

THE UNIVERSITY OF CHICAGO

OBSERVATION OF QUANTUM CRITICALITY WITH ULTRACOLD ATOMS IN  
OPTICAL LATTICES

A DISSERTATION SUBMITTED TO  
THE FACULTY OF THE DIVISION OF THE PHYSICAL SCIENCES  
IN CANDIDACY FOR THE DEGREE OF  
DOCTOR OF PHILOSOPHY

DEPARTMENT OF PHYSICS

BY  
XIBO ZHANG

CHICAGO, ILLINOIS

MARCH 2012

Copyright © 2012 by Xibo Zhang

All rights reserved

*To my motherland, my family, and my friends.*

## ABSTRACT

This thesis reports the observation of quantum criticality with ultracold  $^{133}\text{Cs}$  atoms in optical lattices. The novel experimental techniques that enable this observation include the preparation of two-dimensional (2D) atomic quantum gases in 2D optical lattices, precise tuning of the sample parameters near a quantum critical point, and extraction of local thermodynamics from *in situ* density measurements.

We perform *in situ* microscopy on a 2D quantum gas in optical lattices, and observe the incompressible Mott insulating domains when the repulsive interaction between atoms dominates over their mobility. We study slow mass transport and statistical evolution of atoms in the lattice, as well as scale invariance and universality in weakly-interacting 2D quantum gases without lattice. These results offer the essential knowledge to prepare and investigate atomic samples in the quantum critical regime.

We study quantum critical scaling of the equation of state near the vacuum-to-superfluid quantum phase transition. We quantitatively check the predictions of criticality theory by locating the critical point, testing the critical scaling laws, and constrain the critical exponents. We then explore thermodynamics in the critical regime and study further dependence on the interaction strength. The experimental methods developed here provide promising prospects to study general quantum phase transitions in cold atoms, and to explore the far less understood quantum critical dynamics.

## ACKNOWLEDGMENTS IN CHINESE

大恩无声潜，细流凝于心。

我要感谢我的祖国，生我养我的中华。我能够平平安安地出生并长到二十一岁直至出国留学，是无数先烈用鲜血和生命争取来的机会，龙战于野，其血玄黄，我以他们后人之身份为傲，以一个中国人之身份为豪。

我要感谢我的导师金政教授。从二零零六年三月二十六日直到今日，我从金师的言传身教中获益无数。我在进实验室之前没有深厚的实验背景，进实验室之后，也不是一个飞快的学习者，曾经犯了不少操作错误。然而金师一直支持我，并始终坚持最高的标准。第一次做电路，第一次做光路，第一次设计实验并最终实现目标，第一次写论文并发表，……，我只到后来才慢慢体会到在这些过程中，金师所投入的无数心血，看得到的和看不到的。他可以为弄清一个题目而严苛得似乎不近人情，但他要求的目标从来没有超出我潜力的极限，我可以慢慢体会到那背后的关心和细致。这是一个看着我从孱兵进化成合格的战士的人，他教给我两句话，虽然他自己从来没有说过：

- 忍耐与自信，就算受到再大的苦难或攻击，也非要坚持实验研究不可。
- 直面与勇气，直接面对最残酷的现实，因为这比逃避要有效十倍

我要感谢我的博士后，Nathan Gemelke 教授。Nate 是一个很安静，很坚韧的科学家，他的脑子里总是跳动着各种各样的想法；一旦认定了必要的发展方向，他就会执着地争取和整合各种资源，直至物理目标实现。他同时长于沟通，借用金师的话，Nate 可以和任何人谈任何物理而使彼此受益；而我特别喜欢他时不时的跑进实验室，没有特别的计划，就是为了分享一些有趣的物理或技术进展而发生的无数微型交谈，不少有用的概念就是在这样的谈话中生长而出。从二零零七年五月到二零一零年八月十日，Nate 教了我很多，电子学，光学，物理学，低调和热忱。

我要感谢我的战友，洪承龙博士。从二零零五年九月入学到二零一一年十月二十八日，我很幸运与承龙同窗六年，一起建造仪器和进行实验。我们的才智是不同的，反而是互补的，承龙给我最深的印象有两点，第一，他如果有一个想法，在初步计算设计之后，就会马上行动，而不被诸种借口所阻绊，换言之，他的物理攻击能力特别强，在最相关的时间里，做出即使尚不完美，也五脏俱全的有效工作，然后逐渐改进。第二，他的各方面都很均衡，发展

得很和谐，所以在此基础上深入发展的才能就更加闪光。这六年，我因与承龙共事而成为一个更好的人；这六年，我可以用四个字来总结：血浓于水。

我要感谢我的姐姐，Kathy-Anne Brickman Soderberg 博士 (K-A)。如果有人对我提起“不设防的朋友”，我第一时间想到的就是 K-A。从一句小小的“*How are you?*”，到每次我完成一个演讲，都保证会有有的反馈意见，我和 K-A 在学术演讲和不少其他方面有着共同的价值观，可以不时地自然会心一笑；K-A 点亮了我性格中一度雪藏的阳光一面，而这对整个实验室都很有意义。

我要感谢我的博士后，童世光博士，自二零一零年九月起的一年半里，我们互相支持，推进实验前进。除了 working on cesium 实验外，世光是 LiCs 实验的中流砥柱。我在一起工作中不仅学到物理和技术，而且接触到你的幽默和踏实。很幸运与你同行，汉学满四不可敌，不是吗？

感谢哈立忠师弟，因为有你在 cesium 实验，我可以放心毕业。

感谢 Colin Parker 博士，与你讨论时，你反应的快速和问题的敏锐给我留下了深刻印象；很高兴 LiCs 实验有你加入。

我同时感谢 Tin-Lun Ho 教授，谢谢你对我们实验持续的兴趣和热烈的讨论，更感谢你的真诚鼓励与鼎力支持。

感谢我的爸爸和妈妈，你们的爱是我前进的动力。

.....

这不是一篇完整的致谢(see English version for that)。我真正想做的，是借此机会，把心中的某些思考尽可能准确地表达出来。有一句英文谚语说，*When you articulate, you demonstrate.* 陈述清楚是做到的第一步，也是必要的一步。谢逊明，君子以自量直立。感动着，然后放下。感恩，是为了更好地工作：

**问践广，君子以实验永新。**

张熙博 2012/01/30

## ACKNOWLEDGMENTS

Thank you so much!!

I would like to thank my adviser Prof. Cheng Chin for making my whole journey in ultracold atoms research possible. On March 26, 2006, Cheng welcomed me as a new group member to build up the cesium experiment together. I had little experimental experience then, and didn't realize until much later how much time and thought Cheng had put into training me towards a qualified experimentalist. I learned to form good working habits, to acquire the basics in electronics, optics, and cold atoms, to design and realize new experimental schemes, to explore new physics, and most importantly, to work together under a common commitment. In all these aspects, I am privileged to have the guidance from a master. Moreover, I'm always amazed by Cheng's ability to attract into the group the best people whom I enjoyed working with and learned a lot from. In the past six years, I benefited from a combination of Cheng's two qualities: inspired standards and abundant trust. Cheng, I cannot thank you enough. The margin here is too narrow for writing.

I thank Prof. Nathan Gemelke, who spent three years and three months working as my postdoc. I always enjoyed the numerous "small talks" when Nate entered the lab and started telling us about a new device, a novel technique, or a bunch of interesting physics results. These talks usually did not have a definite agenda; they just happened, and our ideas on experimenting appeared and mushroomed and crystallized. As Cheng once commented, Nate can talk to anyone on anything, which not only shows his talents and knowledge, but also reflects his character. Quiet and resolute towards his dream, and always having a warm interest in people, Nate sets an example for me.

I thank Dr. Chen-Lung Hung, my best friend and partner in crime, who worked hand-in-hand with me from setting up an apparatus to producing physics results. I treasure the time when we stayed up late on cosmology homeworks together, when we fought with the

new current controller, machined the main coils, and set up the vertical lattice together. I especially appreciate your constant reminder “Go out more, to meet different people”. Our qualities are different, yet they are complementary, which makes our working together a very beautiful journey.

I thank my big sister, Dr. Kathy-Anne Brickman Soderberg, who worked next door on the lithium-cesium experiment. In bringing warmth and sunshine to the lab, she is a natural. Although we worked on two different experiments, we shared common values on numerous topics including physics and presentations. I won't forget that when Kathy-Anne was here, every time after I gave a talk, I could always go to her and expect to receive feedback and notes. In fact there is much more. She helped me to grow in character and become a better person, and I feel deep gratitude for this.

I thank Mr. Jeffrey Gebhardt, who taught me a lot of vacuum techniques and skills, and spent a number of late nights with me in fixing vacuum problems and getting things to work.

I thank my postdoc, Dr. Shih-Kuang Tung, for his dedication to experiments, many suggestions and support, and sense of humor. I also thank Shih-Kuang for careful reading of the thesis draft.

I thank Li-Chung (Harry) Ha for taking the responsibility of the cesium experiment's future and for his hard work in preserving the continuity of the lab knowledge and spirit. I also thank Harry for careful reading of the thesis draft.

I thank Dr. Colin Parker for bringing new perspective to the LiCs lab, for his sharp comments in many discussions, and for careful reading of the thesis draft.

I thank Jacob Johansen for bringing new perspective to the LiCs lab, and for careful reading of the thesis draft.

I thank Prof. Selim Jochim who worked with us for two months in the summer of 2006, Kuo-Tung Lin for his numerous help on building electronics and machining parts,

Robert Berry for his professional machining that made a number of our lab components built to last, Skyler Degenkolb for his work on setting up a high-resolution imaging system, Andreas Klinger for setting up the NPRO laser breadboard and testing the dual-wavelength optical lattice setup. I thank Peter Scherpelz for his quality work in both the LiCs lab and the cesium lab (late 2009 to early 2010), and for insightful comments on the thesis draft.

I thank Prof. Tin-Lun Ho for his constant interest in our experiment, for sharing many novel ideas with me, and for his warm encouragement and solid support.

I thank Prof. N. Prokof'ev and Prof. D.-W. Wang for insightful discussions and numerical data, Dr. Q. Zhou, Dr. K. Hazzard, and Prof. N. Trivedi for discussions. I thank S. Fang and C.-M. Chung for numerical data and discussions.

I thank NSF, the Packard foundation, and a grant from the Army Research Office with funding from the DARPA OLE program for supporting the experiment.

I thank the JFI colleagues: Hellmut Krebs for teaching me machining and constantly offering advice, Dr. Qiti Guo for his help on the JFI instruments, John Phillips for his patient and diligent work that keeps the GCIS building (and hence our lab) running stably and smoothly, and Maria Jimenez for helping us organize many events.

I thank my thesis committee for their interest in my research, insightful comments, and constant support.

I thank Nobuko McNeill for her help in all these years. She really treats every student as a family member and offers care, support, and warmth.

I thank Ms. Brenda Ueland and Mr. Jim Collins for their long-term advising, and thank Mr. Jiaju Huang and Ms. Sharon den Adel for inspiration and professional training.

Last but not least, I thank my father and mother for their love and support, and thank deeply my motherland: China.

I am so proud of you.

# CONTENTS

ABSTRACT . . . . .	iv
ACKNOWLEDGMENTS IN CHINESE . . . . .	v
ACKNOWLEDGMENTS . . . . .	vii
LIST OF FIGURES . . . . .	xiv
LIST OF TABLES . . . . .	xvi
1 INTRODUCTION . . . . .	1
1.1 Quantum phase transitions in physics . . . . .	1
1.2 Universal physics near quantum critical points . . . . .	2
1.3 Ultracold atoms in the quantum critical regime . . . . .	5
1.4 Outline of the thesis . . . . .	6
2 EXPERIMENTAL SETUP . . . . .	7
2.1 Apparatus for producing cesium Bose-Einstein condensates . . . . .	7
2.1.1 Overview of the experiment sequence . . . . .	7
2.1.2 Vacuum system . . . . .	9
2.1.3 Diode lasers . . . . .	16
2.1.4 Magnetic coils . . . . .	20
2.1.5 Optical dipole trapping . . . . .	23
2.1.6 Computer control . . . . .	24
2.1.7 Lessons I learned in building the cesium BEC apparatus . . . . .	26
2.2 <i>In situ</i> imaging of 2D atomic gases in 2D optical lattices . . . . .	27
2.2.1 Setting up a pancake-like dipole trap . . . . .	27
2.2.2 Setting up 2D optical lattices . . . . .	28
2.2.3 Building a fast, bipolar current source for the main coils. . . . .	30
2.2.4 Building bipolar current sources for the compensating coils . . . . .	32
2.2.5 Building a stray magnetic field canceller to eliminate the almost spatially uniform magnetic field fluctuations . . . . .	34
2.2.6 Finding the missing pieces . . . . .	34
2.3 Absorption imaging of atomic gases . . . . .	37
2.3.1 Absorption imaging of dilute 3D atomic gases . . . . .	37
2.3.2 Absorption imaging of optically dense 2D atomic gases . . . . .	38
2.3.3 Calibration of absorption imaging for 2D atomic gases . . . . .	38
2.3.4 Experimental setup of the horizontal and vertical imaging paths . . . . .	40
2.4 Further upgrades in the apparatus . . . . .	41
2.4.1 Improving the pointing stability of the dipole trapping beams . . . . .	41

2.4.2	Improving the intensity stability of the dipole trapping and optical lattice beams . . . . .	43
2.4.3	Upgrading the imaging for a higher resolution . . . . .	44
3	MAKING, PROBING, AND UNDERSTANDING TWO-DIMENSIONAL ATOMIC QUANTUM GASES . . . . .	45
3.1	Accelerating evaporative cooling of atoms into Bose-Einstein condensation in optical traps . . . . .	45
3.1.1	Introduction . . . . .	46
3.1.2	Experimental setup and procedures . . . . .	48
3.1.3	Advantage of the trap tilting scheme . . . . .	51
3.1.4	Performance of evaporation using the trap tilting scheme . . . . .	53
3.1.5	Dimensionality of evaporation using the trap tilting scheme . . . . .	54
3.1.6	Applying the trap-tilting scheme in later experiments . . . . .	57
3.2	<i>In situ</i> observation of incompressible Mott-insulating domains in ultracold Bose gases with optical lattices . . . . .	57
3.2.1	Introduction . . . . .	58
3.2.2	Experimental setup and procedures . . . . .	59
3.2.3	Observation of incompressible Mott-insulating domains . . . . .	60
3.2.4	Qualitative comparison with the fluctuation-dissipation theorem . . . . .	65
3.2.5	Detailed procedures and analyses . . . . .	67
3.2.6	Conclusion . . . . .	70
3.3	Slow mass transport and statistical evolution of an atomic gas across the superfluid-Mott insulator transition . . . . .	71
3.3.1	Introduction . . . . .	71
3.3.2	Experimental setup and procedures . . . . .	72
3.3.3	Slow mass transport . . . . .	75
3.3.4	Evolution of occupancy statistics . . . . .	77
3.3.5	Conclusion . . . . .	81
3.4	Observation of scale invariance and universality in two-dimensional Bose gases . . . . .	82
3.4.1	Introduction . . . . .	82
3.4.2	Experimental setup and procedures . . . . .	84
3.4.3	Scale invariance in 2D Bose gases . . . . .	85
3.4.4	Universality in 2D Bose gases . . . . .	88
3.4.5	Evidence of growing density-density correlations in the critical fluctuation region . . . . .	90
3.4.6	Detailed procedures and analyses . . . . .	92
3.4.7	Conclusion . . . . .	95
3.5	Extracting density-density correlations from <i>in situ</i> images of atomic quantum gases . . . . .	95
3.5.1	Introduction . . . . .	96

3.5.2	The density-density correlation function and the static structure factor	98
3.5.3	Measuring the imaging response function $\mathcal{M}^2(\mathbf{k})$	102
3.5.4	Measuring density-density correlations and static structure factors of interacting 2D Bose gases	107
3.5.5	Full analysis of the point spread function and the modulation transfer function	111
3.5.6	Conclusion	114
4	<b>OBSERVATION OF QUANTUM CRITICALITY WITH ULTRACOLD ATOMS IN OPTICAL LATTICES</b>	115
4.1	Proposal: probe quantum criticality with 2D Bose gases in optical lattices	115
4.1.1	Probing quantum criticality with ultracold atoms	115
4.1.2	The Superfluid-to-Mott insulator transition	116
4.1.3	Critical exponents and universality classes	118
4.1.4	The vacuum-to-superfluid quantum phase transition and the predicted critical scaling laws	120
4.2	Experimental setup, procedures, and analyses	122
4.2.1	Preparation of cesium 2D Bose gases in optical lattices	122
4.2.2	Achieving low atomic temperatures	123
4.2.3	Determination of the normal-to-superfluid transition point $\mu_c$	124
4.2.4	Determination of the peak chemical potential and the temperature	125
4.2.5	Effective interaction strength of a 2D gas	127
4.3	Experimental observation of quantum criticality	127
4.3.1	Locating the quantum critical point $\mu_0$	128
4.3.2	Testing the critical scaling law	130
4.3.3	Constraining the critical exponents $z$ and $\nu$	130
4.3.4	Finite-temperature effect on quantum critical scaling	131
4.3.5	Thermodynamics in the quantum critical regime	131
4.3.6	The dependence of thermodynamic observables on inter-atomic interaction strength	135
4.4	Conclusion	136
5	<b>OUTLOOK</b>	137
5.1	Quantum critical dynamics	137
5.1.1	Quantum critical transport	137
5.1.2	Progress on transport measurements	141
5.1.3	Qualitative estimate of the mass conductivity	143
5.1.4	The Kibble-Zurek mechanism (KZM)	148
5.2	Spatially resolved density-density correlation measurements	150
5.2.1	From atomic density of a general-shape cloud to density correlation function defined on a regular square grid	150

5.2.2	Properly weighted discrete Fourier transform for calculating the static structure factor . . . . .	152
A	LIST OF PUBLICATIONS . . . . .	156
	BIBLIOGRAPHY . . . . .	157

## LIST OF FIGURES

1.1	Illustration of the phase diagram of the superfluid-to-Mott insulator quantum phase transition. . . . .	3
2.1	Overview of the apparatus. . . . .	8
2.2	The cesium oven. . . . .	10
2.3	Schematic of the cold nipple. . . . .	11
2.4	Record of the final low-temperature baking. . . . .	14
2.5	Enhanced optical access in the main chamber design. . . . .	16
2.6	Home-built diode lasers. . . . .	17
2.7	Illustration of the cesium D2 transition hyperfine structure and the diode laser frequencies. . . . .	18
2.8	Viewports with different glass-to-metal transition (“the seal”) status. . . . .	26
2.9	The dipole trapping and optical lattice beams setup. . . . .	29
2.10	Picture of the actual optics for the Y-lattice. . . . .	31
2.11	Illustration of the fast bipolar current source. . . . .	32
2.12	Illustration of a bipolar current source for compensating coils. . . . .	33
2.13	Illustration of the optical trap setup. . . . .	36
2.14	Illustration of BEC atoms diffracted by a 2D optical lattice. . . . .	40
2.15	Schematic of the vertical imaging setup. . . . .	41
3.1	Trap-tilt based evaporation and experimental apparatus. . . . .	47
3.2	Performance of trap-tilting based forced evaporation. . . . .	50
3.3	Depth and oscillation frequency of a tilted trap. . . . .	52
3.4	Evaporation speed: experiment and models. . . . .	54
3.5	Snapshot of in situ atomic distribution during slow and fast evaporation processes. . . . .	55
3.6	Temperature and particle number dependence. . . . .	56
3.7	False color absorption images and line cuts along major axis of density profiles for ultracold cesium atoms in a 2D optical lattice. . . . .	61
3.8	Histograms of density profiles in the MI regime. . . . .	62
3.9	Extraction of compressibility from density profiles. . . . .	64
3.10	The fluctuation of local density extracted from a set of twelve absorption images in a weak and a deep lattice regimes. . . . .	66
3.11	Averaged absorption images and density cross sections of cesium atoms in a monolayer of 2D optical lattice. . . . .	73
3.12	Evolution of the density profile after a short lattice ramp. . . . .	76
3.13	Evolution of the on-site statistics in a Mott insulator. . . . .	79
3.14	Illustration of scale invariance and universality in 2D quantum gases. . . . .	83
3.15	Scale invariance of density and its fluctuation. . . . .	86
3.16	Universal behavior near the BKT critical point. . . . .	89
3.17	Fluctuation versus compressibility. . . . .	91

3.18	A comparison between physical length scales and measurement length scales.	100
3.19	Determination of the imaging response function $\mathcal{M}^2(\mathbf{k})$ from <i>in situ</i> images of 2D thermal gases.	103
3.20	Illustration of the patch selected for the static structure factor analysis.	108
3.21	Density fluctuations and the static structure factors of 2D Bose gases.	110
3.22	Analysis of the imaging aberrations and the point spread function.	112
4.1	Illustrations of phase diagrams of the Bose-Hubbard model.	117
4.2	The vacuum-to-superfluid quantum phase transition in 2D optical lattices.	120
4.3	The critical chemical potential for normal-to-superfluid transition at $T_{\text{ref}} = 4.0t/k_B$ .	124
4.4	Compare the scaled equation of state near the normal-to-superfluid transition points.	126
4.5	Evidence of a quantum critical regime.	129
4.6	Finite-temperature effect on quantum critical scaling.	131
4.7	Scaling of pressure $P$ at low temperatures.	132
4.8	Entropy per particle in the critical regime.	134
5.1	Sketch of density and entropy profiles of a trapped, finite-temperature gas.	140
5.2	Evolution of the density profile and the atom number current density after a short 50 ms lattice ramp from zero depth to a final depth of $10 E_R$ ( $U/t = 11$ ).	142
5.3	Illustration of $n(r, \tau) = n(r', \tau_m)$ .	145
5.4	Estimate the chemical potential gradient.	146
5.5	The two-point coordinate difference vector of an elliptical ring region.	151
5.6	Illustration of static structure factor $S(k)$ extracted from different-shaped atomic clouds.	155

## LIST OF TABLES

2.1	Experimental sequences in producing a Bose-Einstein condensate . . . . .	9
2.2	Diode laser frequencies in different cooling and imaging stages. . . . .	19
2.3	The horizontal and vertical imaging setups . . . . .	42

# CHAPTER 1

## INTRODUCTION

### 1.1 Quantum phase transitions in physics

Phase transitions happen everywhere in physics: from the crystalization of water into ice, the vanishing of viscosity in cooled liquid helium, the change into a paramagnet when a ferromagnetic material is heated, to the symmetry-breaking phase transitions in the hot early universe. Many phase transitions are driven by the change in random thermal motion of the atoms or molecules when the temperature is varied. While these different phase transitions have very diverse microscopic features, they often share fundamental characteristics. For example, the specific heat near the water-to-vapor transition under a critical pressure follows the same scaling law (in its dependence on temperature) as that of iron near its demagnetization transition when the temperature is raised [1]. Understanding the universal physics underlying various phase transitions has been a major achievement of 20th century physics [2, 3].

Research over the past two decades has revealed a new type of phase transition that is driven not by thermal motion but by quantum fluctuations based on the Heisenberg uncertainty principle. As the temperature of a many-body system approaches absolute zero, thermal fluctuations of observables cease and quantum fluctuations dominate. Competition between different energies, such as kinetic energy, interactions or thermodynamic potentials, can induce a quantum phase transition between distinct ground states. Quantum phase transitions have been actively pursued in the study of a broad range of materials such as heavy-fermion metals [4, 5], the high-transition temperature (high- $T_c$ ) superconductors [6], quantum dots in the Kondo regime [7], high-density QCD matter [8], and black holes [9]. Near a continuous quantum phase transition, a many-body system is quantum critical, ex-

hibiting scale invariant and universal collective behavior. In the next section, we discuss the important concepts and progress in the study of quantum criticality.

## 1.2 Universal physics near quantum critical points

Even though a quantum phase transition happens at zero temperature, the transition can influence the finite-temperature properties of a many-body system. For example, Fig. 1.1 illustrates the phase diagram of the superfluid-to-Mott insulator transition which happens at temperature  $T = 0$  when the control parameter is tuned to  $g = g_c$  [10]. At low temperatures, the elementary excitations are phonons on the superfluid side ( $g > g_c$ ) and are particle-hole excitations on the Mott insulator side ( $g < g_c$ ). At the critical value  $g = g_c$ , however, there is no well-defined quasi-particle description for the excitations, and no characteristic energy scale except for the temperature  $T$  [11].

Near the quantum critical point, the many-body system is expected to show universal scaling behaviors. As indicated by the vertical arrow in Fig. 1.1, at sufficiently low temperatures, there is only one independent energy scale (chosen as the temperature  $T$ ), and all other thermodynamic observables scale with  $T$ , with characteristic scaling exponents determined by basic properties of the system, such as symmetry and dimensionality [11]. Observing the predicted scaling laws would provide evidence for a quantum critical regime, and the measured generic scaling function can offer valuable information which is often hard to calculate.

A quantum critical many-body system can exhibit characteristic scaling behavior not only in equilibrium thermodynamic observables, but also in various dynamical processes including the quantum critical transport. Theoretical descriptions of quantum critical dynamics are challenging. For example, the transport process at the critical point is described neither by a non-linear equation of waves nor by a Boltzmann equation of quasi-

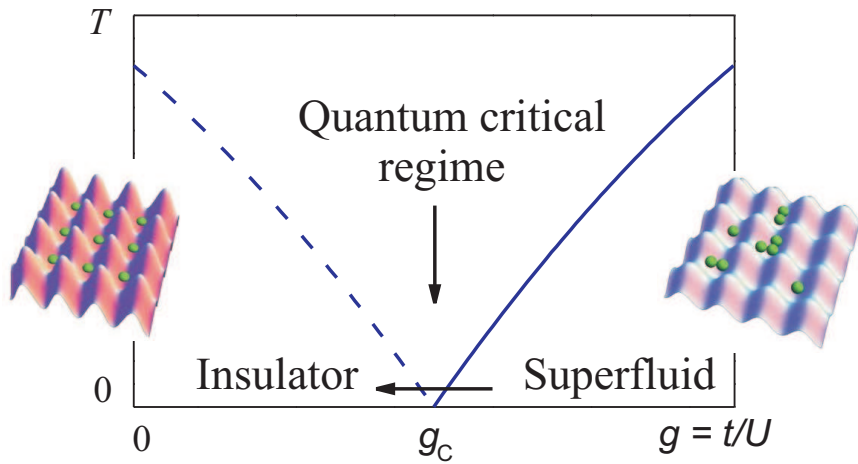


Figure 1.1: Illustration of the phase diagram of the superfluid-to-Mott insulator quantum phase transition. The phase diagram is shown as a function of the temperature  $T$  and coupling constant  $g = t/U$ , where  $t$  is the tunneling energy and  $U$  is the on-site interaction. At zero temperature, the phase transition happens at the critical point ( $T = 0, g = g_c$ ); at finite temperatures, the system shows universal behaviors in the V-shaped quantum critical regime. The two graphs of atomic distributions in optical lattices illustrate the Mott insulator state (left) and the superfluid state (right). Two methods to probe quantum criticality include studying the universal scaling behaviors by changing the temperature of the system, indicated by the vertical arrow, and studying quantum critical dynamics by ramping  $g$  across the quantum phase transition, indicated by the horizontal arrow.

particles [11]. Nevertheless, it is expected that the transport coefficients in the critical regime do not depend on the microscopic details and can be expressed by combinations of fundamental constants in nature. In Ref. [12], the DC electrical conductivity (in two spatial dimensions),  $\sigma_Q$ , is predicted to depend only on the carrier charge  $e^*$  and the Planck constant  $h$ , with a universal constant ( $\Phi_\sigma$ ) of order unity:

$$\sigma_Q = \frac{e^{*2}}{h} \Phi_\sigma. \quad (1.1)$$

Furthermore, a universal scaling function for the conductivity at general frequencies,  $\sigma(\frac{\hbar\omega}{k_B T})$ , can be studied via the gauge-gravity duality [13, 14].

Behavior of quantum critical matter is challenging to calculate or simulate, but can be probed by experiments. In the quantum critical regime, the equilibrium equation of state and thermodynamic observables are predicted to scale with temperature with characteristic exponents based on basic system properties. The corresponding generic scaling functions are hard to calculate but accessible via quantum Monte Carlo simulations. Beyond the equilibrium properties of a critical many-body system, the dynamics is much harder to calculate and also very difficult to simulate (because Monte Carlo simulations mainly provide ground-state properties).

By comparison, experiments can probe both the equilibrium properties and the dynamical processes with similar accuracy and tunability. This thesis focuses primarily on the critical scaling behavior of the equilibrium equation of state and thermodynamic observables, and later discusses our plan to probe critical dynamics. In the next section, we describe our experimental approach: using ultracold atoms in optical lattices to explore quantum criticality.

### 1.3 Ultracold atoms in the quantum critical regime

The realization of Bose-Einstein condensation (BEC) of neutral atoms [15, 16, 17] starts a new era of ultracold atomic physics, enabling the making, probing, and understanding of many exciting novel quantum phases. With powerful tools such as optical lattices [18] and Feshbach resonances [19], ultracold atoms can be controlled and tuned with unprecedented accuracy in all their external and internal degrees of freedom, offering great opportunities to study many-body physics questions that are originally raised in diverse disciplines such as condense-matter physics, nuclear physics, and cosmology.

Our experimental approach is based on bosonic cesium-133 atoms. We produce cesium BECs, load them into a thin layer of two-dimensional optical lattices, and perform *in situ* absorption imaging. Inside the lattice, three processes are relevant: (1) atoms can move around from one lattice site to another, described by the tunneling  $t$ ; (2) atoms on the same site can interact with each other, described by the on-site repulsive interaction parameter  $U$ ; (3) atoms are held in an envelope trapping potential, and each point in the trap can be assigned a local chemical potential  $\mu$ . The competition between these energies ( $t$ ,  $U$ , and  $\mu$ ) can induce the superfluid-to-Mott insulator quantum phase transition near which we study the critical scaling behavior of atoms.

#### ***In situ* microscopy of 2D atomic quantum gases**

A key experimental development is the *in situ* microscopy of 2D atomic quantum gases. Previously, most measurements were based on imaging the atomic clouds after time-of-flight (TOF) expansions. While TOF measurements are excellent in detecting coherence properties, the expansions mix up the information from all the local quantum phases that exist in the trap and prevent spatially resolved knowledge of individual phases. By comparison, probing the atomic density profiles *in situ* provides an alternative for studying local

properties of the cloud.

The atomic samples need to be prepared carefully, too. A 2D image of a 3D sample typically provides integrated column density and averaged information over tens of layers of atoms. Extracting useful information from measurements of 3D samples often involves advanced data analysis such as the inverse Abel transformation [20, 21, 22]. Another experimental alternative is to image only a thin layer of atoms out of a 3D sample via microwave tomography [23]. In our work, we compress a 3D BEC into a single layer of 2D quantum gas; as a result, the column density recorded by the camera is equal to the 2D atomic density, which greatly simplifies the imaging procedures and analyses.

## **1.4 Outline of the thesis**

Chapter two describes the crucial steps in building the experimental apparatus. Chapter three includes a number of our works that either provide essential tools for making and probing the desired quantum states, or reveal important knowledge on 2D atomic quantum gases. Chapter four describes our recent work on observation of quantum criticality with cold atoms in optical lattices, including locating the quantum critical point, testing the critical scaling law, constraining the critical exponents, and subsequently, exploring the thermodynamics in the critical regime. Chapter five lists the possible future directions of the experiment, including plans and preliminary results on quantum critical dynamics, as well as a generalized scheme for extracting local density-density correlation based on an arbitrary-shape region in the atomic sample.

## CHAPTER 2

### EXPERIMENTAL SETUP

This chapter records the design, buildup, and upgrade of our cesium experiment apparatus. I first describe the early experimental setup that enabled us to achieve Bose-Einstein condensate (BEC) of cesium-133 atoms in November, 2007 and enter the quantum world. Next, I describe our apparatus upgrades which led to successful *in situ* imaging of 2D atomic quantum gases. I then give a brief summary on absorption imaging of atomic gases, and describe further improvements in the apparatus.

#### 2.1 Apparatus for producing cesium Bose-Einstein condensates

We chose bosonic cesium-133 ( $^{133}\text{Cs}$ ), the only stable isotope of cesium, for our experiment. The atomic interaction between cesium atoms can be tuned via magnetic Feshbach resonances [19], providing a convenient tool for probing many-body physics. The first step of all our experiments is to produce a cesium BEC. Here I give an overview of the experiment sequence, and then describe the necessary experimental setup and method for each step.

##### 2.1.1 Overview of the experiment sequence

The experiment starts by heating up a cesium source ampule to about  $60^\circ\text{C}$  to get sufficient vapor pressure (in region “A” of Fig. 2.1). Cesium atoms go through a “cold nipple”, an intermediate chamber (region “B”), and the Zeeman slower, and arrive at the main chamber (region “C”).

In the Zeeman slower, atoms with initial speeds below a certain value (about 200 m/s) are slowed down by continuously scattering photons from a counter-propagating laser

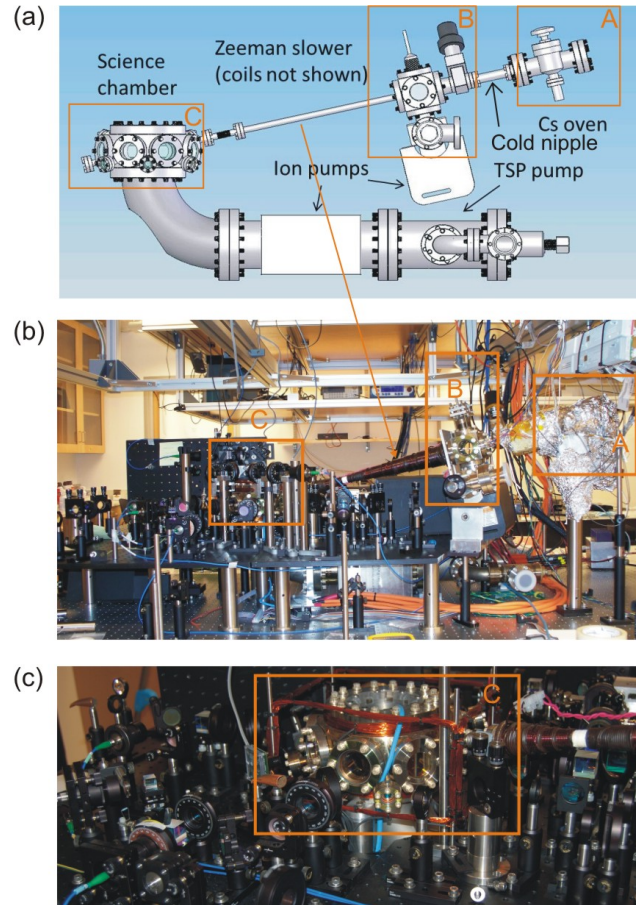


Figure 2.1: Overview of the apparatus: (a) the vacuum design diagram: including the cesium source and oven (“A”), the intermediate region (“B”), and the UHV region (“C”) (b) a picture of the actual setup, taken in 2007/09. (c) a second picture near the main chamber. The photos were taken by the author of this thesis.

beam; their longitudinal speeds are reduced to 50 m/s as they go through the Zeeman slower. Those atoms then enter the main chamber and are captured by the magneto-optical trap (MOT). In the MOT stage, atoms are cooled and trapped by three pairs of counter-propagating lasers together with a quadrupole magnetic field gradient. At the end of the MOT stage, atoms are first compressed by an increased magnetic gradient [24], and then cooled further by optical molasses (with increased frequency detuning and zero magnetic field and gradient). With 2 seconds of MOT loading followed by 32 ms of compressed

MOT and 3 ms of optical molasses cooling, we can have about  $5 \times 10^7$  atoms with a peak spatial density of  $10^{11} \text{ cm}^{-3}$  and a temperature of  $10 \text{ } \mu\text{K}$ . These atoms are subsequently cooled by a sub-Doppler cooling scheme, the Raman-sideband cooling (RSC), and reach a much colder temperature. We perform multiple Raman-sideband cooling to assist the loading of atoms into a conservative potential (the optical dipole trap), wait 0.5 second for self-evaporation, and can have about  $10^7$  atoms with  $1 \text{ } \mu\text{K}$  temperature in the dipole trap. To further increase the atomic phase space density towards quantum degeneracy, we perform forced evaporative cooling by reducing the depth of the dipole trap. We can reduce the atomic temperatures to below 100 nK, enhance the spatial density, and achieve Bose-Einstein condensate (BEC). These sequences are summarized in Table 2.1, where  $n_{\text{max}}$  is the peak density and  $\phi_{\text{max}}$  is the peak phase space density.

Table 2.1: Experimental sequences in producing a Bose-Einstein condensate

Experimental stage	Temperature / atomic speed after stage	$n_{\text{max}}$ ( $\text{cm}^{-3}$ )	$\phi_{\text{max}}$	Atom number
cesium source	330 K	$9 \times 10^{11}$	$5 \times 10^{-16}$	NA
Zeeman slower	50 m/s	NA	NA	NA
MOT and molasses	$10 \text{ } \mu\text{K}$	$10^{11}$	$1 \times 10^{-5}$	$5 \times 10^7$
RSC-assited dipole trap loading	$1 \text{ } \mu\text{K}$	$10^{12}$	$3 \times 10^{-3}$	$10^7$
Forced evaporation to BEC	$\leq 100 \text{ nK}$	$10^{13}$	$> 1$	$10^4 \text{ to } 10^5$

### 2.1.2 Vacuum system

In designing our vacuum system, we have two primary goals: to achieve ultrahigh vacuum (UHV) in the main chamber, and to have good optical accesses. As shown in Fig. 2.1, our vacuum system has three regions: (A) the low vacuum region containing the cesium source and oven, (B) the intermediate region, and (C) the UHV region including the main cham-

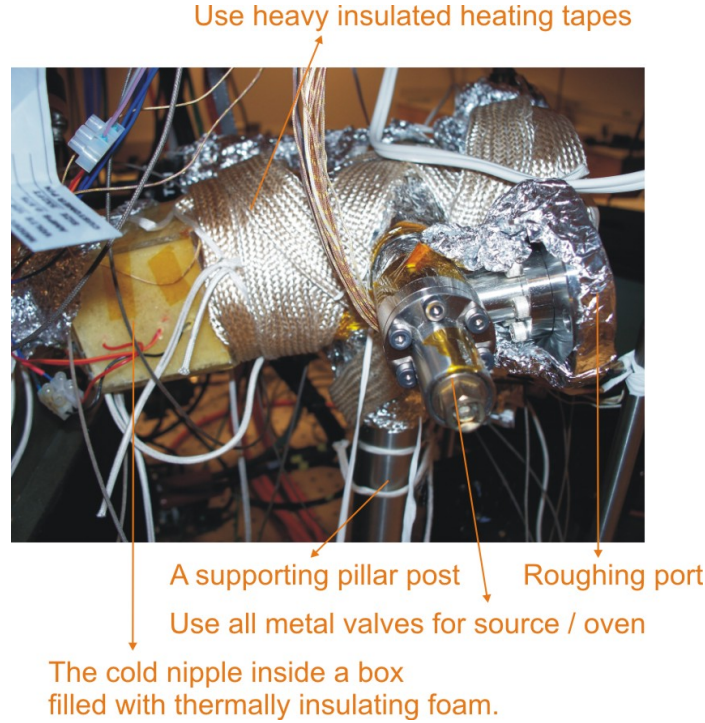


Figure 2.2: The cesium oven. The source is on the opposite side and not seen in the picture. To ensure good electrical insulation, we use heavy insulated heating tapes (made by Omega Engineering). The photo was taken by the author of this thesis.

ber. The typical pressures in these regions are (A)  $10^{-5}$  to  $10^{-4}$  torr (primarily contributed by the cesium vapor pressure at oven temperature  $60 \sim 70$  °C), (B) below  $10^{-9}$  torr, and (C) below  $10^{-11}$  torr.

### A. The cesium source and oven

Atoms come from a source tube containing five grams of cesium (SIGMA-ALDRICH, 239240-5G). The source and oven need to be designed with care. Firstly, because cesium is chemically active and can attack normal glass-to-metal transitions (made of lead alloy), we chose a custom-made source tube (MDC 463000-1000) consisting of a Pyrex tube and a stainless steel (SST) adapter which are directly connected together without introducing a third type of material for the Pyrex-to-SST transition. Secondly, because cesium attacks

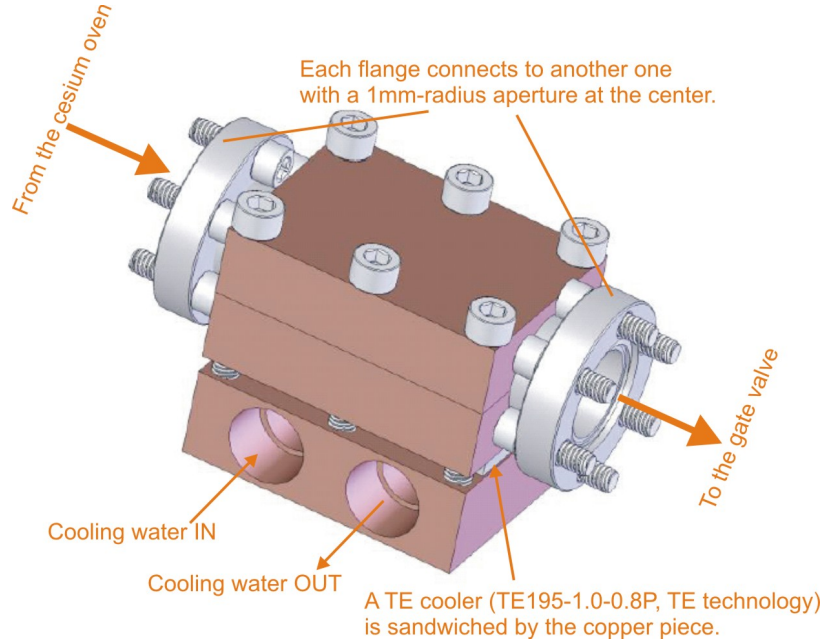


Figure 2.3: Schematic of the cold nipple. The nipple is cooled by a thermoelectric cooler (backed up by water cooling) to about 0 °C, and connects to a flange with a small central aperture (2 mm in diameter) on each end.

the Viton or Kalrez seals (O-rings) of some vacuum valves, we used exclusively all-metal valves (VAT 54024-GE02) in the oven region. Thirdly, to ensure safety in heating up the oven, we used exclusively heating tapes with heavy electrical insulation instead of those with normal insulation. In addition, a timer (Intermatic TN311C) was used to automatically turn on the power supply (Variac) for the source or oven heating every morning and turn it off every night, saving us 1.5 hours warm-up time every day.

To provide sufficient atomic flux, the source tube is heated to 60 °C, providing a vapor pressure of about  $3 \times 10^{-5}$  torr. To prevent cesiums from depositing on the inner oven surface, the oven is heated to slightly higher temperatures (about 70 °C) and the viewport on the oven has the highest temperature. At the same time, to maintain a much lower pressure in downstream regions (slightly above 80 °C), a “cold nipple” is placed between the oven and the intermediate chamber, see Fig. 2.1 and 2.2. As shown in Fig. 2.3, the nipple is

cooled by a thermoelectric cooler (backed up by water cooling) to about 0 °C, and connects to a flange with a small central aperture (2 mm in diameter) on each end. The apertures only allows atoms whose velocities point to the chamber to pass. Other atoms will hit the wall and stick, reducing the background vapor pressure to  $9 \times 10^{-8}$  torr.

### **B. The intermediate chamber**

The cold nipple is connected to a gate valve and then to the intermediate chamber (region B in Fig. 2.1). This chamber is constantly pumped by an ion pump (Gamma Vacuum 40S-CV-2D-SC-N-N, 40 liters/second) and has a pressure below  $10^{-9}$  torr. A wobble-stick is fed through the chamber and can be used to block the atom flux when needed.

#### *Zeeman slower*

A Zeeman slower tube (7 mm in inner diameter, 40 cm in length) is connected between the intermediate chamber and the main chamber (under UHV), and has a vacuum conductance of 0.06 liter/second. For a pressure of  $1 \times 10^{-9}$  torr in the intermediate chamber, the gas flow (throughput) into the main chamber is  $6 \times 10^{-11}$  torr·liter/second, and the caused pressure increase is  $6 \times 10^{-13}$  torr (very small and negligible) for a main chamber ion pump with 100 liters/second pumping rate.

### **C. UHV in the main chamber**

The main chamber (Kimball physics, MCF600-SO200800) is the most important vacuum component where the experiments are performed. It is pumped by an ion pump (Gamma Vacuum, 100L-DI-6D-SC-US110-N) with a large pumping rate (100 liters/second). In addition, a Titanium sublimation pump (Gamma Vacuum, 360043) is connected to provide extra pumping power. To reach the typical pressure (below  $1 \times 10^{-11}$  torr), care needs to be taken in multiple bakings of the system.

### **Pumping down and baking the system**

Before assembling the vacuum system, the vacuum components need to be carefully cleaned. Most stainless steel components (without delicate structures) are cleaned with an ultrasonic cleaner (filled with water and Alconox detergent), then rinsed with ethanol or acetone, and finally blew dry by the nitrogen gas or dry air supplied by the lab building. Other parts like all-metal vacuum valves and ion pump tubes are simply rinsed by ethanol or acetone and blew dry. Viewports are the most delicate parts in the vacuum system and are cleaned by lens tissues and isopropyl alcohol in the usual way of cleaning optics.

Here for cleaning the viewports, we need to be very careful never to immerse the assembly in an aqueous environment because there is a risk of setting up galvanic corrosion with the diffusion bond (suggested by the viewport manufacturer UKAEA Special Techniques), and never to blow a viewport with a lot of cleaning liquid on it because there is a risk of violating the maximum heating/cooling rate of the viewport and causing severe leaks in the glass-to-metal transition. Once the vacuum system is assembled, we leak-check each component using a leak detector (Adixen ASM142) based on helium.

To further clean the vacuum system, multiple baking steps were carried out to accelerate the outgassing from the inner surfaces and remove the gases by pumping. Firstly, once the main chamber and all other UHV components were pre-assembled (without putting on any viewports and with the magnet removed for the ion pump), they were baked under high temperatures (about 370 °C maximum) for 8 days (2006/07/23 to 2006/07/31) and pumped by a turbo pump (Drytel 1025) throughout the process, in order to remove light atoms such as hydrogen from the inner surfaces. Secondly, the intermediate region (from the gate valve to the Zeeman slower) was separately baked under relatively low temperatures (190 °C maximum) for 11 days to remove water. Thirdly, after the whole system was assembled, we baked it under low temperature (195 °C maximum) for 13 days (2007/03/03

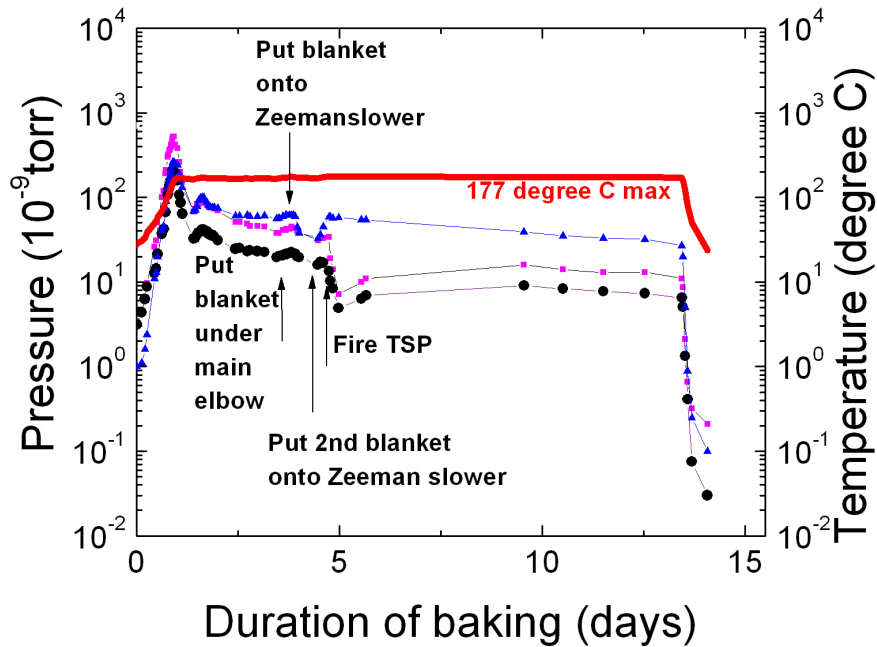


Figure 2.4: Record of the final low-temperature baking. The average of four sampled temperatures (two on the main chamber and two near the Zeeman slower) was shown as the thick red line, with a peak value of 177°C. The absolute maximum temperature was 195°C reached at one point on the main chamber. The pressure read by the UHV24p gauge (black solid) decreased by a factor of 100 when the system was fully cooled down, showing the baking worked well. The other two pressures are the readings of main chamber ion pump (squares) and the intermediate ion pumps (triangles); both readings are limited by the pump resolution of  $1 \times 10^{-10}$  torr.

to 2007/03/16) to remove water.

Figure 2.4 shows the evolution of pressure readings during the baking. In the final baking, the pressure readings in the UHV and intermediate regions started with  $3 \times 10^{-9}$  and  $1 \times 10^{-9}$  torr at room temperature, reached peak values of  $5 \times 10^{-7}$  and  $3 \times 10^{-7}$  torr when the system was heated up, decreased by a factor of 10 after 1.5 days, and decreased by another factor of 4 after another 11 days before we cooled down the system. When the system is fully cooled down, we observe a pressure of  $4 \times 10^{-11}$  torr using a vacuum gauge (Varian UHV24p). Moreover, this reading was later found to be an overestimation because

the gauge controller was too warm. After we removed the controller cover to provide more air cooling, we observed a gauge reading of less than  $3 \times 10^{-12}$  torr. Considering the fairly good vacuum conductance between the gauge and the main chamber, we concluded that the pressure in the chamber was below  $1 \times 10^{-11}$  torr. Thus the baking performance was very good.

One year after the apparatus started operating, the intermediate region had a low pressure reading of less than  $3 \times 10^{-10}$  torr. However, this reading grew slowly over time, and was 100 times larger at the time of this writing (December 2011) than its early value (in 2007 and 2008). However, we didn't observe any evidence of degraded vacuum limiting the experiment (each cycle took 6 to 10 seconds) in the main chamber. We did observe the apparent pressure reading in the intermediate chamber decreased after we replaced the high voltage cable between the ion pump and its controller, or simply after we turned off and restarted the high voltage. Thus the apparent pressure reading increase can be related to a leakage current between the ion pump electrodes.

After baking the intermediate and UHV regions, we also baked the source tube and oven region before and after adding cesium. In these bakings, the oven was heated up to 150 °C and was pumped at its roughing port by a turbo pump (Alcatel Drytel 1025); the cold finger region was heated (instead of being cooled) by reversing the current in the TE cooler. The gate valve was closed in these bakings to protect the high-vacuum regions.

### **Enhanced optical access in the main chamber design**

We design the main chamber to have a pair of recessed viewports (the top and bottom viewports). The inner surfaces of both viewports are very close (13.6 mm) to the chamber center (position of atoms), providing enhanced numerical aperture which is essential for high-resolution imaging, see Fig. 2.5. (Also see Fig. 2.15 in section 2.3.4 for a schematic of the vertical imaging setup making use of the enhanced numerical aperture.) Besides,

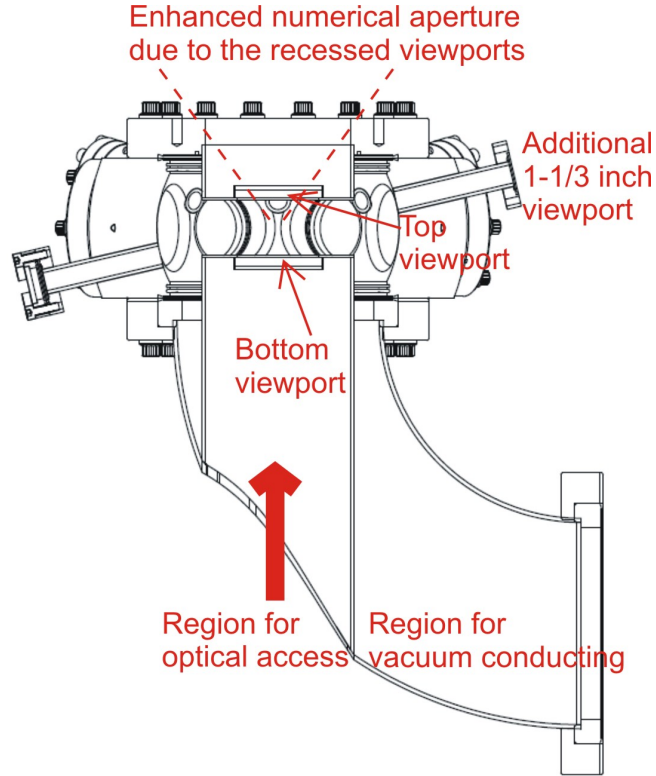


Figure 2.5: Enhanced optical access in the main chamber design.

eight additional 1 – 1/3 inch viewports are welded to the eight custom designed ports on the chamber to further increase the optical access.

### 2.1.3 Diode lasers

Several laser cooling and trapping stages happen before the forced evaporation: Zeeman slowing, magneto-optical trapping (MOT), molasses cooling, and the subsequent Raman-sideband cooling (RSC). Five diode lasers are built for these stages: “reference”, “MOT”, “Repumper”, “RSC master” and “RSC slave”. The first four are grating-feedback to deliver laser beams with stable frequencies (Fig. 2.6a) and moderate power. The fifth laser (RSC

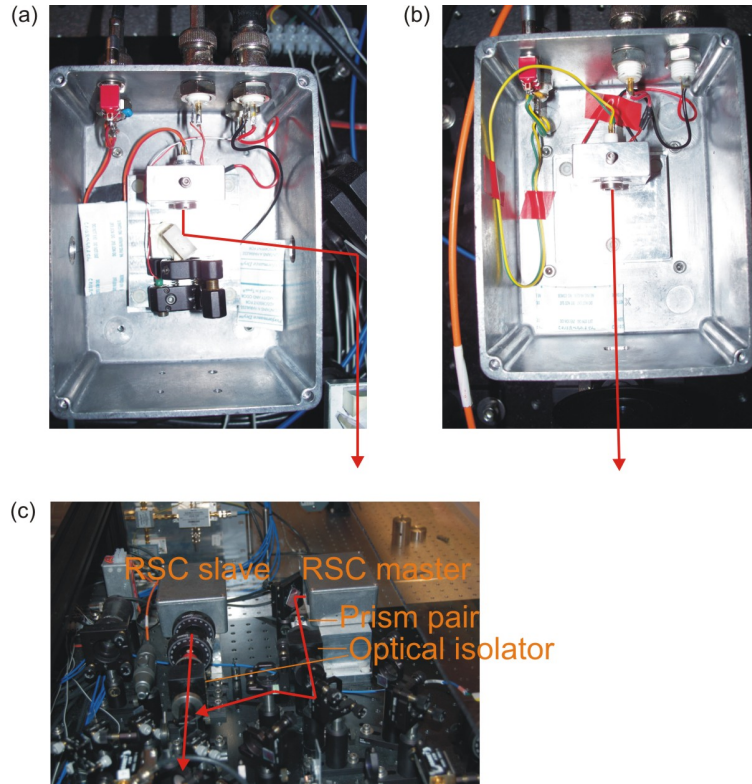


Figure 2.6: Home-built diode lasers. (a) A diode laser with grating feedback. The beam comes out of the laser diode, gets diffracted by the grating, comes out of the box, and is reflected into the desired direction by a mirror. (b) A diode laser without grating feedback (free-running). The output beam from the laser diode directly come comes out of the box. (c) Optics near the master and slave lasers for Raman-sideband cooling. The photos were taken by the author of this thesis.

slave, see Fig. 2.6b) doesn't have a grating and is designed to be injection-locked by the RSC master to give sufficient output power.

As shown in Fig. 2.7, the reference laser frequency is locked to +320 MHz with respect to the  $F = 4 \rightarrow F' = 5$  transition based on polarization spectroscopy. The MOT and Repumper laser frequencies are locked close to the  $F = 4 \rightarrow F' = 5$  and  $F = 3 \rightarrow F' = 4$  transitions, respectively, based on the beat-note between each laser and the reference laser. These two lasers, MOT and Repumper, are needed in the Zeeman slowing, MOT, and molasses cooling stages. After the molasses stage, we need one more pair of lasers to do the

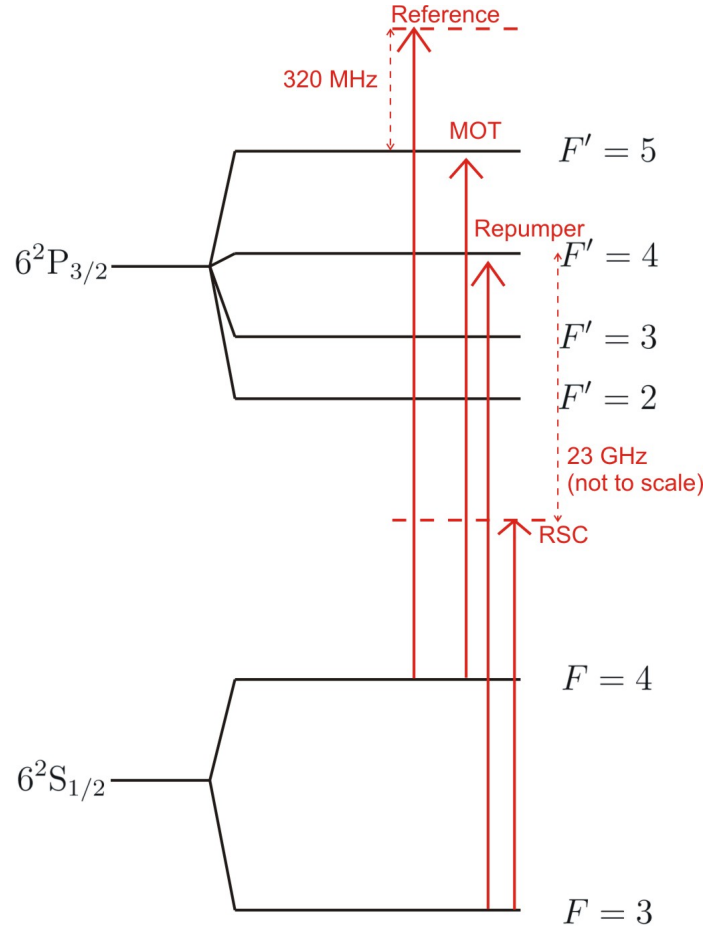


Figure 2.7: Illustration of the cesium D2 transition hyperfine structure and the diode laser frequencies.

Raman-sideband cooling: the RSC master laser is free-running at -20 GHz with respect to the  $F = 3$  to  $F' = 4$  transition (see Fig. 2.7). In Table 2.2 (see Ref. [25] for details), we summarize the laser frequencies in different experimental stages.

The RSC slave laser is injection-locked by the master. As shown in Fig. 2.6c, after each laser comes out of the laser box (with a 3 to 1 aspect ratio and a vertical polarization), it goes through a pair of prisms to make the profile round, and then goes through an optical isolator. The isolator for RSC slave has a side escape window on the output side; two weak

beams comes out of this window. The injection lock is done by first aligning the RSC master beam (with a few mW power) to counter-propagate with the beam coming out of the escape window with a larger bending angle, and then fine tuning the alignment until the slave laser mode totally follow that of the master. We find the slave laser can be injection locked within a current range of  $\pm 3$  mA at a center current of about 140 mA.

After the optical isolator, the slave laser goes through an AOM, a mechanical shutter, and is guided to a second optical table by optical fiber. The injection-locked slave laser has a very good beam profile, and can have better than 80% coupling efficiency into the fiber, with a total power of 70 mW. Note that the injection affects the slave laser beam profile, and we need to re-optimize the fiber coupling efficiency every time the master laser frequency is changed.

Table 2.2: Diode laser frequencies in different cooling and imaging stages.

Diode laser	Experiment stage	Reference transition	Detuning
“MOT”	Zeeman slowing (ZS)	$F = 4 \rightarrow F' = 5$	-93 MHz
“Repumper”	ZS	$F = 3 \rightarrow F' = 4$	-91 MHz
“MOT”	MOT	$F = 4 \rightarrow F' = 5$	-14 MHz
“Repumper”	MOT	$F = 3 \rightarrow F' = 4$	-11 MHz
“MOT”	Compressed MOT	$F = 4 \rightarrow F' = 5$	-26 MHz
“MOT”	Molasses	$F = 4 \rightarrow F' = 5$	-106 MHz
Optical pumping beam	RSC	$F = 3 \rightarrow F' = 2$	+6 MHz
Depumping beam	RSC	$F = 4 \rightarrow F' = 4$	+6 MHz
“MOT”	Horizontal imaging	$F = 4 \rightarrow F' = 5$	0
“Repumper”	Horizontal imaging	$F = 3 \rightarrow F' = 4$	0
“MOT”	Vertical imaging	$F = 4 \rightarrow F' = 5$	+26 MHz
“Repumper”	Vertical imaging	$F = 3 \rightarrow F' = 4$	+37 MHz
RSC master/slave	RSC	$F = 3 \rightarrow F' = 4$	-23 GHz

### The tapered amplifier

To obtain more power, we inject a commercial tapered amplifier (Sacher TEC400) with a seed beam combining parts of the MOT (20 milliWatt) and Repumper lasers (1 milliWatt).

To get a longer lifetime for the amplifier, we operate it at a current (1.5 A) smaller than

the maximum value (slightly larger than 2 A). Because the output profile of the amplifier actually has a double-peak structure which is elongated along the two peaks, we use a prism pair to make the overall profile more round, and optimize the total coupling efficiency of both peaks into a fiber. The best efficiency is about 40%. Here we tune the pointing of the seed beam that injects the amplifier, such that the two peaks contain comparable power; this strategy, instead of distributing most power into one peak, might help extend the lifetime of the amplifier (which has lasted for 5.5 years without showing signs of degrading) [26].

Note that our imaging beams comes directly from the MOT laser, not the amplifier, because the amplifier output might have a broad background at all frequencies, which is bad for imaging.

#### 2.1.4 *Magnetic coils*

Three sets of coils are built for stable and precise control of magnetic fields and gradients: (A) the Zeeman slower coils, (B) the main coils, and (C) the X/Y/Z compensating coils. In this section, we summarize the setup of each set and describe the corresponding experimental stages.

##### **Zeeman slower coils**

In the Zeeman slower, atoms are slowed down by resonantly scattering photons from a counter-propagating laser beam during their traveling inside the slower tube. We design the Zeeman slower coil such that the laser frequency seen by atoms is always on resonance with respect to the  $|4, 4 \rangle \rightarrow |5', 5' \rangle$  transition based on a combination of Zeeman shift, Doppler shift, and the laser detuning. Here we summarize the main results in the following paragraph. The design and test of the Zeeman slower coils are described in details in Ref. [27].

As described in a previous section, the Zeeman slower vacuum tube (7mm in inner

diameter, 40 cm in length) connects the intermediate chamber and the main chamber (see Fig. 2.1a, between regions B and C). Five sections of coils, made of square magnet wires (2 mm in diameter), are wound onto the vacuum tube. A bias coil (a solenoid) is first wound onto the tube, and four sections of coils are then wound on top of the bias coil (section 1, 2, 3, 4 starting from the farthest to the chamber center), with a tapered profile that has a minimum between section 2 and 3. Applied currents are 0, 1.2, -1.0, -0.91, and 3.4 A for sections 1 to 4 and the bias coil, respectively. These coils are air-cooled. We find the MOT has a 30% better loading rate when the axial field gradient in the Zeeman slower is arranged to be opposite to the quadrupole gradient at the chamber center (contributed by the main coil). In this configuration, we achieve a velocity range of 50 to 205 m/s for slowing and an atomic flux of  $8 \times 10^8 \text{ s}^{-1}$  in the MOT capture range.

### **Main coils**

The main coils are a pair of coils close to the chamber. The coils are made of 35 (bottom coil) to 36 (upper coil) turns square magnet wires (1.93 mm in diameter, AWG 13, from MWS wire industries) and are filled with high-strength epoxy (Stycast 2850 FT Black + Catalyst 23 LV). Each coil have inner and outer radii of 23.7 mm and 35.8 mm and 12.1 mm vertical thickness, and the pair is separated by 33.2 mm (measured from inner surfaces). Each coil is fixed to a polycarbonate mount by the same epoxy; the coil is close to but has no direct contact with the main chamber. The main coils can produce a magnetic field of  $B = \bar{I}/\text{amp} \times 6.7 \text{ gauss}$  in the Helmholtz configuration, and can produce a magnetic field gradient of  $B' = 1.6 \text{ gauss/cm} \times \Delta I/\text{amp}$ , where  $\bar{I}$  and  $\Delta I$  are the mean and difference of the two coil currents.

Before we achieved a cesium BEC, the main coil currents were controlled by unipolar current sources. The resulting magnetic field gradient could change its polarity, but the field could not. This limitation didn't prevent us from achieving BECs, but did cause

inconvenience for subsequent experiments. We later replaced this first controller by a new, bi-polar, and faster controller (described in a later section).

Because we typically work with 10 A or smaller currents, the main coils are designed to be air-cooled. However, in order to prevent overheating the coils, one needs to avoid running the coils continuously with 10 A currents (roughly corresponding to a magnetic gradient fully levitating the  $|F = 3, m_F = 3\rangle$  atoms in the anti-Helmholtz configuration, or a magnetic field of 67 gauss in the Helmholtz configuration). To provide both a levitating gradient and an upward magnetic field, the coils are in a superposition of Helmholtz and anti-Helmholtz configurations, and the upper coil has a larger current. Indeed, in a recent upgrade of the imaging system, we noticed that the polycarbonate mount for the upper coil were slightly distorted after five years of running experiments. This distortion might be either due to the normal heating from the upper coil over a long time, or due to some accidental overheating of the coil. In retrospect, G10 epoxy glass might be a better material for making the coil mount.

### **Compensating coils**

The compensating coils are three pair of Helmholtz coils near the chamber. The X and Y coils are rectangular coils (50 turns, 9.5 inches  $\times$  4.4 inches for X, and 70 turns, 6.2 inches  $\times$  4.4 inches for Y), and Z coils are round coils (50 turns, 3.1 inches radius, and 3.4 inch apart from center to center) wound on the main chamber top and bottom flanges. The coils are made of round magnet wire (AWG 22.5, from MWS wire industries), and can produce uniform magnetic fields at the chamber center:  $B_X = 2.1 \text{ gauss} \times \bar{I}_X$ ,  $B_Y = 1.9 \text{ gauss} \times \bar{I}_Y$ , and  $B_Z = 5.9 \text{ gauss} \times \bar{I}_Z$ . Because the typical currents in the coils are small, the coils are air-cooled.

### **Other coils**

After achieving cesium BECs, we made another large coil for cancelling the fluctuation of stray magnetic field that is almost spatially uniform, see section 2.2.5.

### 2.1.5 Optical dipole trapping

In order to reach quantum degeneracy, atoms need to be evaporatively cooled in a conservative trap after the optical cooling. Because cesium atoms at the lowest-energy ground state  $|F = 3, m_F = 3\rangle$  are not magnetically trappable, we need to trap them in optical dipole traps based on high-power lasers with large frequency detunings. For a 1064 nm laser (far from the cesium  $D_2$  line, 852 nm, and  $D_1$  line, 894 nm), the trapping potential  $U$  depends on the laser intensity  $I$  and detuning  $\delta$ :

$$U = \sum_{i=D_1, D_2} p_i \frac{h\gamma_i}{8} \frac{I/I_{\text{sat},i}}{\delta_i/\gamma_i} \quad (2.1)$$

where  $p_{D_1} = 1/3$ ,  $p_{D_2} = 2/3$ ,  $\delta_i$  and  $\gamma_i$  are the frequency detunings and transition linewidths,  $I_{\text{sat},i} = \frac{2\pi^2}{3} hc\gamma_i/\lambda_i^3$  are the saturation intensities,  $\lambda_i$  is the wavelength,  $h$  is the Planck constant, and  $c$  is the speed of light. Numerically we have  $|U| = k_B \times 2.34 \text{ pK} \times \frac{I}{1\text{mW/cm}^2}$ , where  $k_B$  is the Boltzmann constant. In the early design before we achieved BEC, we simply have two 1064 nm beams (in X and Y directions) crossing at the atoms and forming a crossed dipole trap. Each beam has a  $1/e^2$  radius of about 300  $\mu\text{m}$ .

In this period, the dipole trapping laser came from a 20-Watt IPG fiber laser (YLR-20-1064-LP-SF, single frequency, single mode), and we controlled the light intensity by acousto-optic modulators (AOMs). Here I have several remarks:

- It is important to have a single-frequency high-power laser for setting up the dipole trap. If a multi-frequency laser is used to set up a crossed dipole trap, the polarizations of the two beams need to be perpendicular to each other in order to minimize

atomic loss and depolarization.

- The IPG fiber laser we bought in early 2007 had an average break-down rate of once per year, which severely slowed down our experiment. Thus we later switched to another laser with similar maximum power (Innolight Mephisto MOPA 18E, S/N 1866). The new laser has worked reliably for more than two years since November, 2011.
- The AOMs we used in this period (Isomet 1201E-2, for 1064 nm) were rather slow but did not limit the evaporative cooling to BEC, so we only replaced them with faster ones much later. Similarly, we didn't lock the light intensities and relied on the AOMs' own stability of diffraction efficiencies.

### 2.1.6 *Computer control*

In the cesium experiment, we have two computers (PC): “Dimer” and “Quatromer”. Dimer has four PCI-boards from National Instrument to generate analog and digital (“TTL”) output voltages: (1) a 32-channel, 20 MHz digital I/O board (PCI-6534) with 5V TTL signals; (2) two 8-channel (1 MS/s per channel), 12-bit analog I/O boards (PCI-6713), whose voltage resolution is  $(10\text{ V} - (-10)\text{ V})/2^{12} = 4.8828\text{ mV}$ . (Both boards are triggered by channel 1 of the digital board); (3) one 32-channel (45 kS/s per channel), 13-bit analog output board (PCI-6723), whose resolution is 2.4414 mV. (This board is triggered by channel 2 of the digital board).

We use Dimer to control the experimental sequence and use Quatromer to connect to the CCD camera and collect images. Dimer runs a experimental control program (home-written in Labview) which use digital channels to trigger the instruments (CCD cameras, arbitrary function generators, shutters, and so on) and use analog channels to provide quantitative control voltages between -10 V and 10 V. The program first collects all the update

edges and calculates a matrix (with respect to time and channel number) for the updates of all channels, and then executes the update matrix. Due to the slow speed of calculations in Labview, it takes about 4 seconds to calculate the update matrix, which is comparable to our typical experimental time. Because our experimental cycle is fairly short, we are not limited by this 4 s calculation time; at the same time, it is possible to rewrite the major matrix calculations in much more efficient programming languages such as C, IDL, or Matlab.

Due to the limited PCI data transfer rate, our update size cannot exceed the on-board FIFO memories, or the experiment might encounter interruptions. This constraint doesn't limit our experiment sequence where there are relatively few ramping processes. At the same time, newer boards based on PCI express, PXI bus have faster data transfer rate and can alleviate this limitation. Field-programmable gate array (FPGA) provides another promising choice in the computer control of experimental sequences.

We use Quatromer to connect to the CCD camera using a home-written Labview program. At the end of each experimental cycle, Dimer sends a signal to Quatromer; once receiving the signal, Quatromer will collect the image from CCD camera, save the data if asked to, and perform realtime image analyses, and in the end send back a signal to Dimer for it to start a new cycle. The complex realtime image analyses are performed not using Labview but using the more efficient IDL via an IDL-to-Labview tunnel. It is also possible, in fact worthwhile to write the entire camera control program in non-Labview languages such as Matlab, because Labview is not designed for command-line programming (which is very important for writing complex analysis programs).

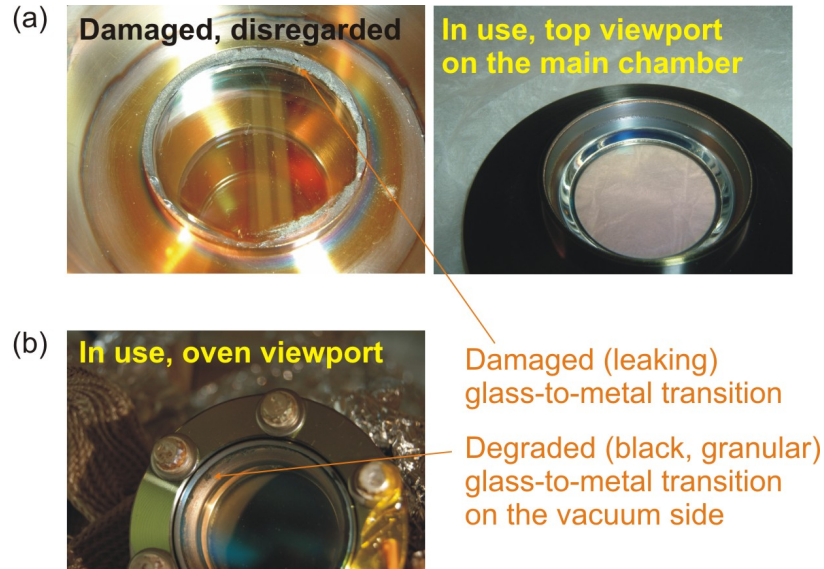


Figure 2.8: Viewports with different glass-to-metal transition (“the seal”) status. (a) Left: a severely leaking top viewport; right: a new viewport (by Special Techniques) after coating. The seal of the new viewport is silver and shiny, while the seal of the leaking viewport is black, has multiple defects, and is not shiny at all. (b) The viewport in the oven region. The seal on the atmosphere side is in good shape, but the seal on the vacuum side is granular and has many defects, which might be caused by the attack of cesium (with  $10^{-4} \sim 10^{-5}$  high vapor pressure) in the oven. The photos were taken by the author of this thesis.

### 2.1.7 *Lessons I learned in building the cesium BEC apparatus*

While many tasks needed to be accomplished in building a BEC apparatus, some tasks did require much more care than others, and our progress was limited by the few mistakes we made. In retrospect, the most important task in the pre-condensate stage is to achieve UHV in the main chamber and maintain it. In 2006/08, we made severe mistakes in cleaning the viewports, violating the maximum cooling rate by more than 100 times<sup>1</sup>. This single event caused a huge vacuum failure in 2006/10 and stopped our experiment for four months. From this, we learned the lesson that the viewports are the most fragile parts of the vacuum

1. When we cleaned the viewports, we put a lot of acetone onto the viewport (including the glass-to-metal transition, and then used an air-gun to blow the acetone away. The original purpose was to remove all the acetone without leaving any residue, but this blowing cooled down the glass-to-metal transition way faster than the allowed rate, which is likely the primary reason that many viewports leaked later.)

system, and it is very essential to collect standard cleaning and baking procedures from multiple direct manufacturers of the viewports. We also learned that even if we get the standard procedures, it is necessary to first try them on a sample piece before applying them to all viewports. After the vacuum failure, we followed both lessons and succeeded in achieving ultra-high vacuum in the main chamber in 2007/03, and achieved BEC half a year later. Fig. 2.8a shows a comparison between a severely leaking viewport and a newly coated viewport; the major difference is in the glass-to-metal transition regions.

In addition, we have one viewport in the oven region. This viewport was originally put in to ease the alignment of the Zeeman slower beam. However, later we found the alignment was fairly straightforward, but the viewport started to show degraded glass-to-metal transition in the vacuum side (see Fig. 2.8b). This is likely due to the repeated attack from the cesium in the oven. In retrospect, we should have put in a blank flange at this position instead of a viewport.

## **2.2 *In situ* imaging of 2D atomic gases in 2D optical lattices**

After achieving a cesium BEC and investigating a fast evaporation based on tilting the dipole trap [28], our physics goal turns to studying cold atoms in 2D optical lattices based on *in situ* imaging. Towards this goal, we changed the apparatus in various aspects: (1) set up a pancake-like dipole trap, (2) set up 2D optical lattices, (3) build a fast, bipolar current controller for tuning the magnetic field, (4) build a stray-field canceler to stabilize the magnetic field to milligauss precision, and a number of other improvements.

### *2.2.1 Setting up a pancake-like dipole trap*

We produce a pancake-like dipole trap (“the light sheet”) with tighter confinement in the vertical directions by shooting an additional elliptical laser beam through the crossed dipole

trap. The light sheet was at first produced by a high-power CO<sub>2</sub> laser beam (10.6  $\mu\text{m}$ ) and corresponded to a compressed BEC with 5 to 1 aspect ratio (horizontal to vertical). Later the CO<sub>2</sub> beam was replaced by a 1064 nm beam from the same source as that of the X and Y dipole beams, because the intensity of a CO<sub>2</sub> laser is much harder to lock than that of a 1064 nm laser.

In the present setup, the light sheet beam comes out of an optical fiber with a 4.0 mm focal length collimator, passes through a cylindrical lens (25 mm) that focuses the beam vertically, and then goes through a telescope (100 mm to 125 mm) before it reaches the atoms. This results in a horizontal  $1/e^2$  radius of 270  $\mu\text{m}$  and a vertical radius of 45  $\mu\text{m}$ . Using less than 1 Watt of power out of the fiber, the light sheet can provide a vertical trapping frequency of about 100 Hz when the gravity is cancelled by a magnetic levitating force. This frequency becomes about 60 Hz (still more than 50% of the maximum trapping frequency) at the end of evaporative cooling where the magnetic gradient is turned off and the trap depth greatly decreases due to gravity.

### 2.2.2 *Setting up 2D optical lattices*

We produce a 2D optical lattice by retro-reflecting the two horizontal dipole beams in the X and Y directions. As shown in Fig. 2.9, each incident dipole beam goes through the atoms, passes through a pair of AOMs, get reflected by a final mirror, and comes back through the AOM pair again before it re-enters the chamber. Here the two AOMs are driven by radio frequency waves from the same source, leading to zero total frequency shift and twice the total diffraction angle. This enables us to produce a lattice potential with continuously controllable strength. We can get about 50% max total diffraction efficiency when the light double-passes two AOMs (sufficient to produce most lattice depths needed experimentally), and can dynamically control the retro-reflected light intensity over

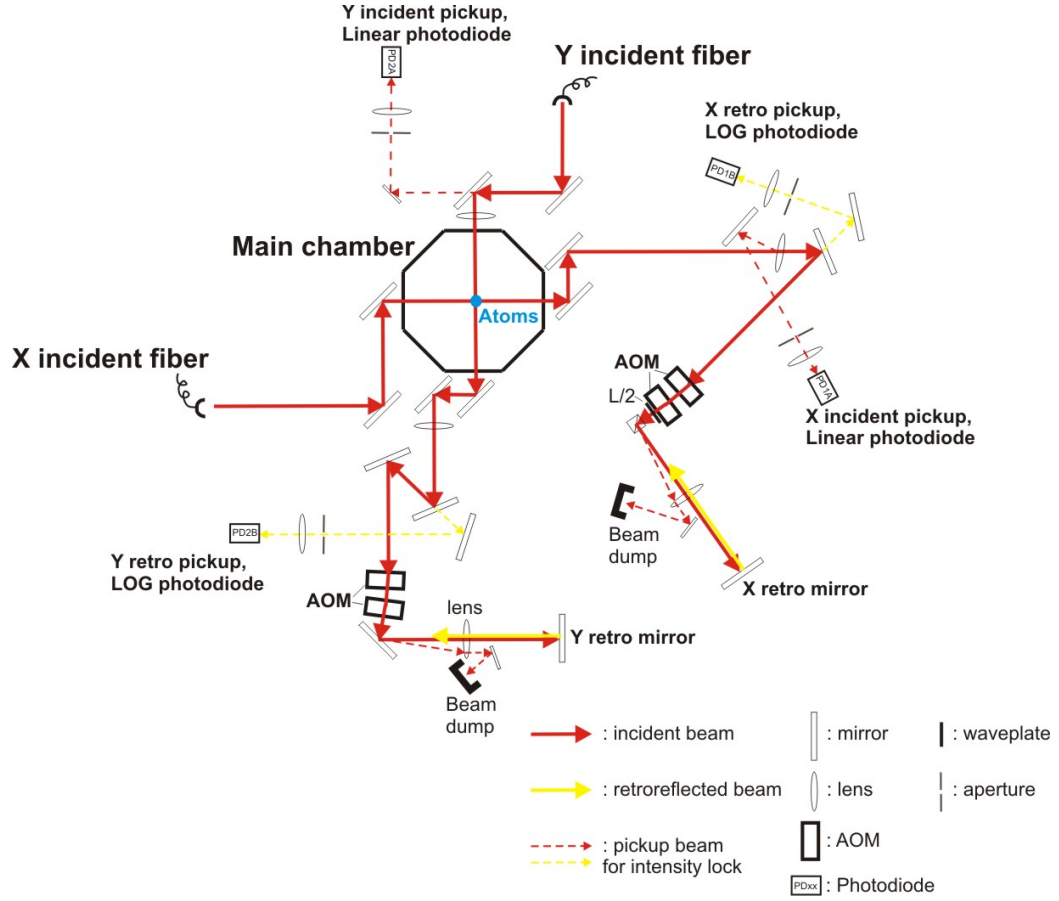


Figure 2.9: The dipole trapping and optical lattice beams setup. Here we provide the schematics for two dipole trapping beams in the X and Y directions. Each dipole trapping beam is retroreflected to form an optical lattice.

more than five orders of magnitude. As the diffraction efficiency is optimized, the retro-reflected beam automatically overlaps with the incident beam, avoiding the usual challenge of overlapping the dipole beam with a completely separate lattice beam. Slowly turning up the retro-reflected power thus converts a dipole trap into an optical lattice with only slightly increased envelope trapping frequency.

In designing the optical lattice setup, we have considered and disregarded two possible configurations:

- Use a single AOM for each retro-reflection path. Here in order to let the beam ex-

perience opposite frequency shifts when it passes the AOM for the first and second time, the AOM must be imaged by a lens onto the final retro-reflecting mirror (via  $2f$ -to- $2f$  imaging, where the AOM and retro-mirror are both twice the focal length from the lens). In this configuration, however, it is difficult to separate the diffracted, retro-reflected beam from the incident zeroth-order beam. Thus the design fails.

- Use two AOMs for each retro-reflection path, and place the two AOMs to be perpendicular to each other, such that the diffractions happen in horizontal and vertical directions, respectively. This design is excellent in separating all the diffraction orders, but causes unnecessary inconvenience in dumping the unwanted diffraction orders. Therefore, we choose the present design described above: in a single pass of the two AOMs, the incident beam is bent twice horizontally in the same angular direction, and is frequency-shifted upward once and downward once such that the total frequency change is zero.

To provide further stability in alignments of the retro beams, lenses are included to image the atoms onto the retro-mirror, such that even if the incident beam has some fluctuations in its pointing direction, the retro-reflected beam will still pass through the atoms. A picture of the actual Y-lattice beam setup is provided in Fig. 2.10.

### 2.2.3 *Building a fast, bipolar current source for the main coils.*

We built bipolar current sources for both upper and lower main coils. As shown in Fig. 2.11, the current in each coil,  $I_{\text{coil}}$ , can be bipolar because it is provided not by one unipolar source, but by the difference between two independent unipolar sources  $I_1$  and  $I_2$ :  $I_{\text{coil}} = I_1 - I_2$ . Here both  $I_1$  and  $I_2$  has a finite bias current (about 10 amp) to ensure the tuning range of  $I_{\text{coil}}$ .

Each unipolar current source consists of a small-signal FET  $Q_A$  and a high-power FET

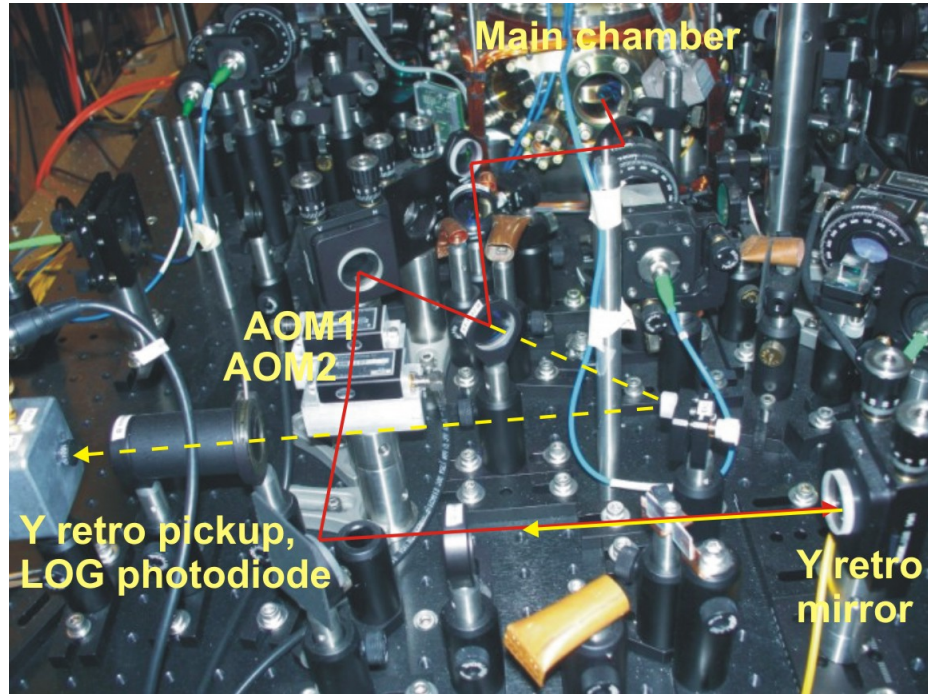


Figure 2.10: We show the actual optics for the Y-lattice beam path after the main chamber, with the beam path and key components highlighted. The photo was taken by the author of this thesis.

$Q_B$ . The two FETs have similar shapes of I-V characteristic (with different proportionality constants), and share the same control voltage. Thus the total current output  $I_i = I_{i,A} + I_{i,B}$  can be controlled by the relatively low current  $I_{i,A}$  with good linearity.

While the current in the coil can switch off fast (switch-off slew rate limited by the breakdown voltage of the high-power FET), it switches on with a much slower rate (limited by the available supply voltage). To boost the switch-on slew rate, one introduces two changes. Firstly, always ask  $I_1$  and  $I_2$  to have the same bias current  $I_b$ , such that their changes are symmetric (if one increases, the other must decrease):  $I_1 = I_b + I_{\text{coil}}/2$  and  $I_2 = I_b - I_{\text{coil}}/2$ . Thus either  $I_1$  or  $I_2$  will be decreasing and have a fast switching rate. Secondly, add two transformers (whose cores are shown in orange in Fig. 2.11) into the circuit, such that the faster switching side (say, it is the  $I_2$  side) will generate a large

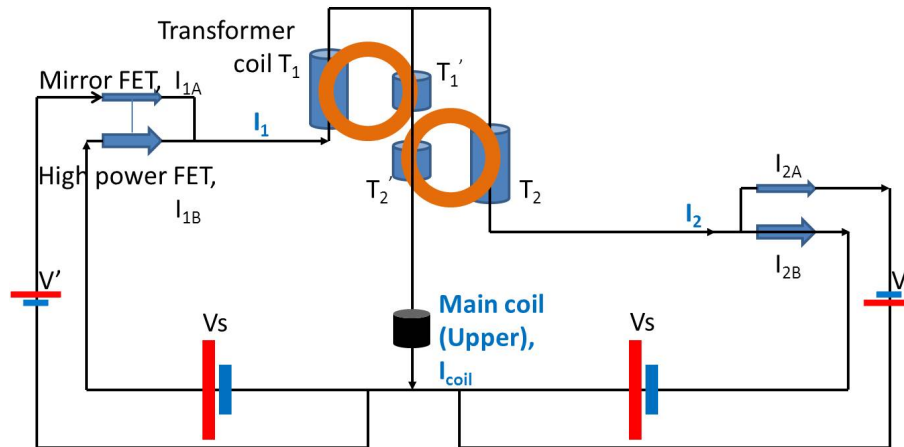


Figure 2.11: Illustration of the fast bipolar current source. The two “Vs”s represent two high-current (8 V, 50 A) power supplies, the two V’s are the  $\pm 24$  V linear power supplies, the black cylinder is one of the main coils, the blue cylinders ( $T_1$ ,  $T_1'$ ,  $T_2$ , and  $T_2'$ ) with different lengths are transformer coils, and the orange doughnut-shaped objects are the toroidal cores (made of ferrite) for the transformers.

transient voltage in coil  $T_2$ , which in turn will transmit the large voltage to  $T_2'$  such that the current in  $T_2'$  can change fast. At the same time, note that  $T_1'$  is in series with  $T_2'$  and will now have a similar fast current switch, which again transmits the large transient voltage to  $T_1$  and enables  $I_1$  to switch fast. In the end, the main coil current  $I_{\text{coil}} = I_1 - I_2$  can switch fast. The above qualitative picture is confirmed by actual measurement. With the transformer method, a typical improvement of 25 in the switch-on slew rate can be achieved [29].

#### 2.2.4 Building bipolar current sources for the compensating coils

Until the middle of 2008, we used an old current source for compensating coils. This source had limited current range, a complicated crossover behavior when the current passes zero, and a rather slow speed. We built new bipolar current sources based on high-power operational amplifiers (op amp, APEX PA12). As shown in Fig. 2.12, the coil current  $I_{\text{coil}}$

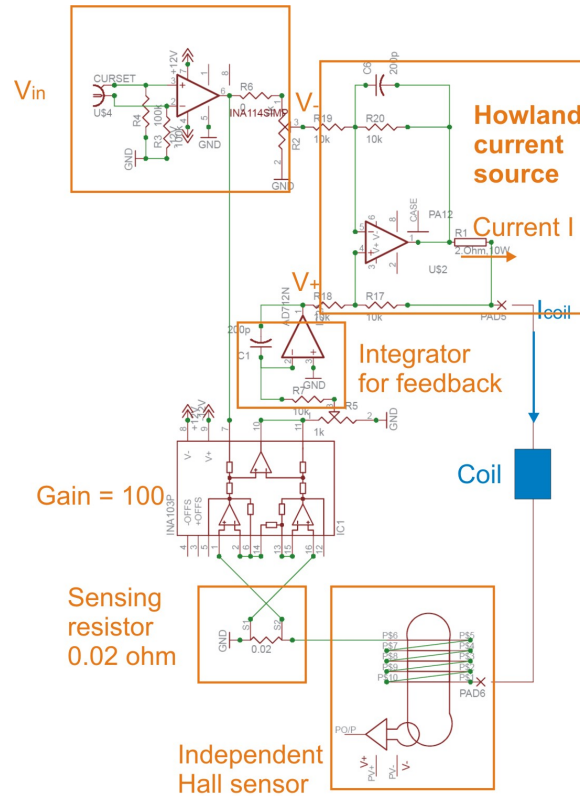


Figure 2.12: Illustration of a bipolar current source for compensating coils.  $I_{coil} \approx I = (V_+ - V_-)/R_1$ . The circuit uses feed-forward (via  $V_-$ ) to the Howland current source to finish most of the desired current change with a fairly high bandwidth based on the high-power op amp, and uses feedback from a sensing resistor to maintain accuracy.

is provided via the current  $I$  through a 2 ohm resistor in a Howland-type current source:  $I_{coil} \approx I = (V_+ - V_-)/R_1$ . The circuit uses feed-forward (via  $V_-$ ) to the Howland current source to finish most of the desired current change with a fairly high bandwidth based on the high-power op amp, and uses feedback from a sensing resistor to maintain accuracy. The advantage is an inherent bi-polar current source without crossover problems.

### 2.2.5 *Building a stray magnetic field canceller to eliminate the almost spatially uniform magnetic field fluctuations*

To study some of the narrow Feshbach resonances of cesium, we need to stabilize the magnetic field to milligauss (mG) precision. Because our lab is close to the two building elevators, we check and find a 14 mG fluctuation as the two elevators go up and down based on measurements using a Fluxgate magnetometer (Applied physics systems, model 534, with 4.00V/gauss). To cancel this fluctuation via feedback, we need to make sure the error signal (based on the fluxgate reading) is insensitive to our own tuning of the magnetic field and gradient via the main and compensating coils. Firstly, we carefully chose the position and orientation of the fluxgate, such that it sits where the main coil field line is horizontal and its reading for vertical field ( $B_z$ ) is insensitive to the magnetic field due to the main coil (variation within 1 mG when the main coil field changes by more than 60 gauss). Secondly, we check the dependence of the fluxgate  $B_z$  reading on all other PC control voltages, find two of them (the main coil magnetic gradient and the compensation field in Y direction), and add them (with proper linear weight) to the fluxgate  $B_z$  reading to obtain the real error signal. We also attenuate the intrinsic high-frequency oscillation (at about 7 kHz) using a low-pass filter before summing up the voltages. Thirdly, we build a large square coil above the chamber (10 turns, 41 cm above the atoms, 145 cm $\times$ 118 cm, providing 0.056 gauss/amp). Lastly, we feedback to the coil current according to the error signal, and eliminate the almost uniform stray field fluctuation to better than 1 mG.

### 2.2.6 *Finding the missing pieces*

In 2008/09 to 2009/01, we already loaded a BEC into 2D optical lattices, but didn't see a clear signature of Mott insulating domains, likely because the vertical confinement is still too weak. Qualitatively, with a vertical trap frequency of 60 Hz, one site in a 2D op-

tical lattice acts like a 1D tube; atoms on the same site can largely avoid each other by being at different positions along the tube, thus reducing the effective on-site repulsive interaction and preventing the superfluid-to-Mott insulator transition. We decided to further compress the BEC by loading it into a single site of a vertical lattice. Besides, in order to minimize the atomic loss, we chose to perform imaging at high magnetic field (about 18 gauss). These two experimental procedures provided the last two pieces that fit the big picture, and enabled us to perform a number of experiments based on *in situ* absorption imaging [30, 31, 32].

### **Further compress the atoms vertically**

We further compress the atoms by introducing a one-dimensional lattice in the vertical direction and compressing the pancake-like BEC (formed in the light sheet) into one single site of the vertical lattice. As shown in Fig. 2.13, the vertical lattice is formed by intersecting two beams ( $\pm 8$  degrees with respect to the horizontal plane) at the atoms, and has a spacing of  $3.8 \mu\text{m}$ .

The vertical lattice beams come from a separate laser (Innolight Mephisto NPRO, model number M2000NE, S/N 1796) with 2 Watt output at 1064 nm. We couple the beam into an optical fiber and can have 1.1 Watt out of the fiber. The beam goes through a collimator (an aspheric lens with 4mm focal length), and is then split into two beams (upper and lower) by a  $\text{YVO}_4$  Wollaston polarizer (Day Optics PWS8010, with 10mm aperture). The two beams go through a telescope (100 mm to 125 mm, the same one for the vertical light sheet) and cross at the atoms. The polarization of the lower beam is rotated to be vertical, the same as that of the upper beam, such that the two beams interfere at the atoms. This produces a vertical confinement frequency of 850 Hz, which already corresponds to a trap aspect ratio of 85 to 1 and enables the 2D experiments. Later, to compress the cloud even more, we shape the vertical lattice beam to have a smaller vertical size at the atoms

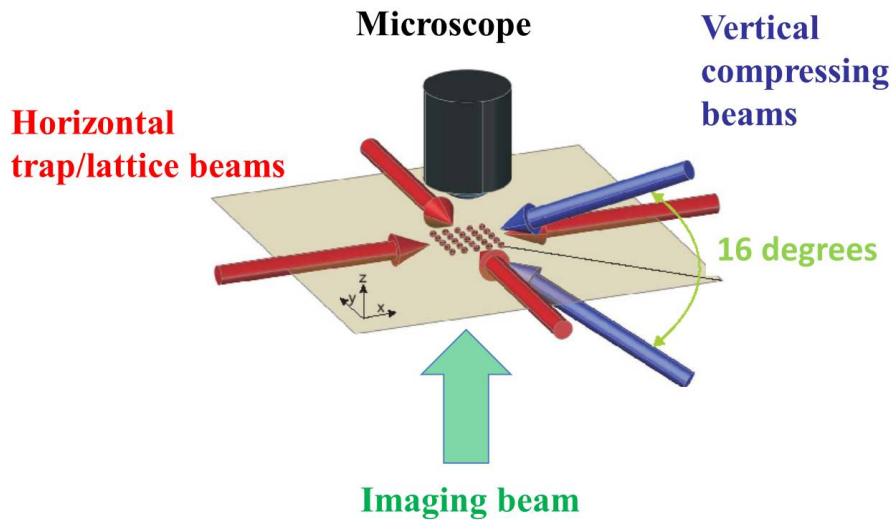


Figure 2.13: Illustration of the optical trap setup.

by including two cylindrical lenses (a 100 mm lens before the Wollaston polarizer and an 80 mm lens closely after the Wollaston polarizer).

### Image at high magnetic field

When we switched the magnetic field value to near zero, where the scattering length  $a$  is large and negative ( $a < -2000a_0$ ), the atomic loss rate is substantial for the typical atomic density inside optical lattices. To minimize this effect, we chose to perform *in situ* imaging near a magnetic field of 17.6 gauss where the scattering length is small and positive, and the loss is small and negligible.

## 2.3 Absorption imaging of atomic gases

### 2.3.1 Absorption imaging of dilute 3D atomic gases

In the simplest picture, absorption imaging is performed by shining a weak on-resonance imaging laser beam (with wavelength  $\lambda$ , along the  $z$  direction) through the atomic cloud, and measuring the beam intensity attenuation due to atom-photon scattering. The integrated atomic column density  $n_{cl} = \int n_{3D} dz$  can be related to the intensity attenuation:

$$n_{cl}(x, y) = \frac{1}{\sigma_0} \ln \frac{I_0(x, y)}{I(x, y)}, \quad (2.2)$$

where  $x$  and  $y$  are the coordinates in the plane perpendicular to the imaging beam,  $I_0$  and  $I$  are the imaging beam intensities without and with the atoms, and  $\sigma_0 = 3\lambda^2/2\pi$  is the resonance cross-section for the atom-photon interaction.

If the imaging beam intensity is not so weak, the cross-section will become  $\sigma = \sigma_0/(1 + I/I_{\text{sat}})$ , where  $I_{\text{sat}} = \pi h c \Gamma / 3 \lambda^3$  is the saturation intensity,  $h$  is the Planck constant,  $c$  is the speed of light,  $\Gamma$  is the natural linewidth of the imaging transition. Because the imaging intensity gradually decreases as the light goes through the cloud, the cross-section  $\sigma$  will change accordingly and the simplest formula is now accurate only for an infinitely thin slice of cloud. We can solve an ordinary differential equation, and derive the following modified formula:

$$n_{cl}(x, y) \sigma_0^* = \frac{I_0(x, y) - I(x, y)}{I_{\text{sat}}^*} + \ln \frac{I_0(x, y)}{I(x, y)}, \quad (2.3)$$

where  $\sigma_0^*$  and  $I_{\text{sat}}^*$  are effective parameters that can be different from  $\sigma_0$  and  $I_{\text{sat}}$  due to an imperfect imaging beam polarization (deviation from  $\sigma_+$ ), a finite period before the atoms enter the cycling transition  $|4, 4\rangle \rightarrow |5', 5'\rangle$  (especially when the imaging pulse is short),

and a possible line width broadening. Thus  $\sigma_0^*$  and  $I_{\text{sat}}^*$  need to be independently calibrated.

In the horizontal imaging path, we generally turn off the trap and let the atoms expand for a finite period into a dilute cloud before taking the image. The imaging beam intensity is weak and we apply Eq. 2.2 only with  $\sigma_0$  replaced by an independently calibrated  $\sigma_0^*$  due to possible imperfect imaging beam polarization and other practical factors.

### 2.3.2 *Absorption imaging of optically dense 2D atomic gases*

For a 2D sample with very small thickness (comparable to or smaller than the imaging beam wavelength) in the imaging beam direction ( $z$ ), the calculations for a 3D sample won't apply because all the atoms can experience the same imaging beam intensity. The situation is further complicated because atoms can have some collective scattering behavior when they are close to each other; the collective behavior is different from the single atom process we previously discussed. Fortunately, the picture is greatly simplified if the imaging intensity is much larger than the saturation intensity and each atoms scatters photons with maximum possible rate. In this limit of  $I \gg I_{\text{sat}}$ , the possible collective effect can be suppressed [33, 34]. Provided the imaging pulse length is much longer than the excited state lifetime, one can adopt a statistical model for atom-photon scattering [34, 27], and arrive at the same formula, Eq. 2.3, where  $\sigma_0^*$  and  $I_{\text{sat}}^*$  need to be independently calibrated.

### 2.3.3 *Calibration of absorption imaging for 2D atomic gases*

#### **Calibrate the saturation intensity**

According to Eq. 2.3, if we perform imaging with different beam intensities on clouds prepared under identical conditions, the sum of  $\ln(I_0/I)$  and  $(I_0 - I)/I_{\text{sat}}^*$  should be the same ( $n\sigma_0^*$ , here we write the 2D atomic density  $n$  instead of the integrated column density  $n_{cl}$ ). Thus we can leave  $I_{\text{sat}}^*$  as a free parameter and try overlapping the  $n\sigma_0^*$  profiles taken

with different imaging intensities. We find that we can indeed overlap the different profiles, and thus obtain  $I_{\text{sat}}^*$  as the fit parameter which gives the optimized overlapping.

### **Calibrate the resonant cross-section $\sigma_0^*$**

In the low-density tail of the atomic cloud, the local fluctuation of atom number  $N_i$  in a small patch (with Area  $A_i$ ) should obey the Poisson distribution,  $\delta N_i^2 = N_i$ , which in principle can be used for density calibration. In the real experiment, however, the natural patch size  $\sqrt{A_i}$  (taken as the pixel size of CCD camera) is often much smaller than the imaging resolution  $R$ . Consequently, the apparent number fluctuation within a single pixel is reduced. To overcome this limitation, we evaluate the average value and shot-to-shot variance of the local  $n\sigma_0^*$  in binned pixels with different sizes (from  $1 \times 1$  to  $10 \times 10$ ), and find the corresponding slopes in the  $\delta(n\sigma_0^*)^2$  versus  $n\sigma_0^*$  plot in the low density tails. The slope saturates as the bin becomes larger and larger, and the saturated value can be used to derive the cross-section  $\sigma_0^*$ .

### **Calibrate the imaging magnification**

For our horizontal imaging with a large field of view, we can watch the free fall of atoms and derive the magnification  $M_{\text{hor}}$  based on the measured acceleration (in pixel/second<sup>2</sup>) and the known value for the local gravitational acceleration  $g$ . One can then produce an identical reference object, compare its images using the horizontal imaging and the vertical imaging, and use  $M_{\text{hor}}$  to derive the vertical imaging magnification  $M_{\text{vert}}$  based on the known pixel sizes in both CCD cameras.

Another more direct way to calibrate the vertical imaging magnification is to use the “standard length” provided by the recoil peak spacing in the time-of-flight images taken after (1) applying a short 2D lattice potential pulse to a degenerate cloud and (2) immediately shutting down all the trapping potentials to let the cloud expand for a finite period. Note

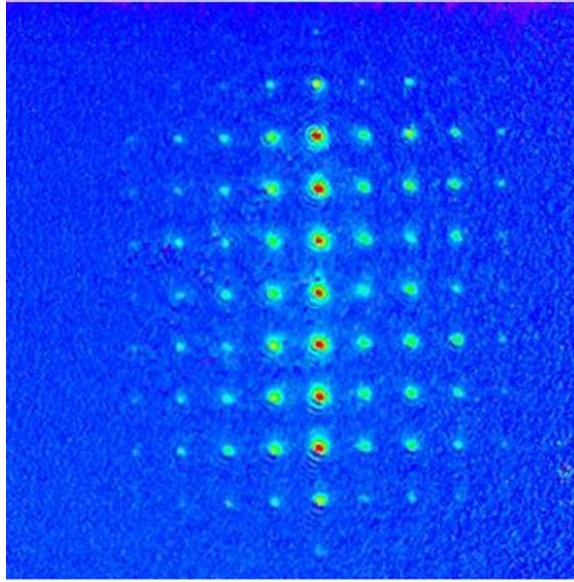


Figure 2.14: Illustration of BEC atoms diffracted by a 2D optical lattice. We apply a short pulse of 2D optical lattice potential to a BEC, turn off the trap to let the atoms expand for a finite time-of-flight time, and then take the image. The recoil peak spacing can be used to calibrate the imaging magnification.

that the atoms should be levitated while they expand. The finite magnetic field and gradient can introduce a small anti-trapping force which needs to be considered in the calculation. A sample image is shown in Fig. 2.14.

### 2.3.4 *Experimental setup of the horizontal and vertical imaging paths*

Our primary detection method is absorption imaging, either with the trap turned off a certain period before the imaging (“time-of-flight”) or with all the traps kept on during the imaging (“*in situ*”). We have two imaging paths: in the horizontal imaging path (in the Y direction), we have a near-unity magnification and a large field of view, and can conveniently watch and debug the experiment; in the vertical imaging path (in the Z direction), we have a large magnification and perform high-resolution *in situ* imaging using a microscope objective, as illustrated in Fig. 2.15. The important instruments and optics are

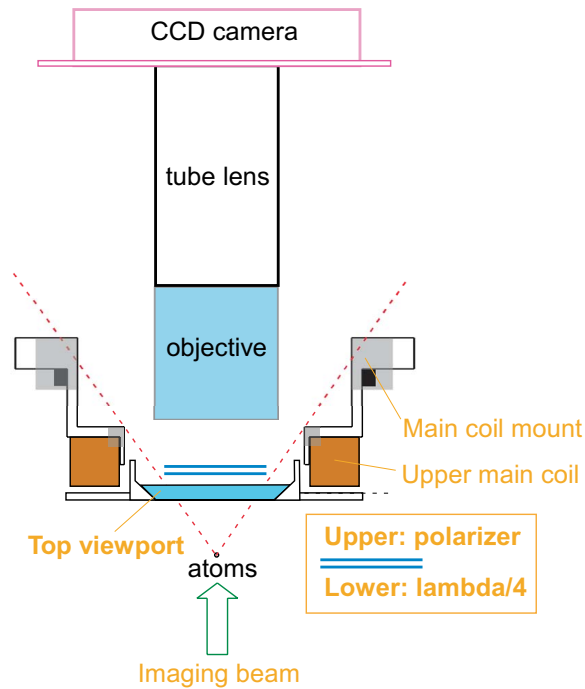


Figure 2.15: Schematic of the vertical imaging setup. The imaging beam (green arrow) comes from below, goes through the atoms (at the crossing point of the two dashed lines) and a number of optics (the top viewport, a  $\lambda/4$  waveplate, and a polarizer plate), then goes through the microscope objective and the tube lens, and finally reaches the CCD camera. The two dashed lines illustrate the numerical aperture allowed by the designs of chamber and coil mounts.)

summarized in Table 2.3.

## 2.4 Further upgrades in the apparatus

### 2.4.1 Improving the pointing stability of the dipole trapping beams

Although the temperature and humidity in the lab is fairly stable, they did sometimes fluctuate dramatically (for example, under extreme weather). When we first set up the dipole trapping beams, everything from the high power laser to the final optics sat on the same

Table 2.3: The horizontal and vertical imaging setups

Item	Horizontal imaging	Vertical imaging
CCD camera	Andor DU-434-BV	Andor DU434-BR-DD
Magnification	1.22	19.5
Lens near atoms	GPX50-125-DB5 (125 mm)	microscope objective (OKHNL10, 34 mm WD)
Lens near camera	GPX50-150-BB2 (150 mm)	InfiniTube tube lens ( $\times 10$ ) and magnifier ( $\times 2$ )

table, and the alignment only involved free-space propagations. Some optics (such as the AOMs) were sensitive to the room temperature / humidity, and could cause a substantial displacement of the cross dipole trap position. The beam profile also changed from time to time, leading to changes of the dipole trap size and shape. To minimize these undesired changes, we decided to separate the high power laser source and the main experimental breadboard, and to use optical fibers to connect the two.

Optical fibers have several advantages. Firstly, the spatial mode out of a polarization maintaining fiber is very clean and stable. Secondly, the beam pointing is also stable against the temperature / humidity fluctuations. Thirdly, we can put all the controlling optics (like AOMs) before the fiber and convert all their fluctuations into a single quantity, the fiber output power fluctuation, and stabilize it by intensity lock.

As promising as the fiber scheme is, it also has practical concerns. First of all, we observe fringes in the atomic pattern inside the dipole trap formed by beams out of fiber. In order to minimize or eliminate these fringes, we need to minimize the number of 1 inch lenses in the path before the main chamber. For X and Y dipole beams, this number is zero and one (a indispensable imaging lens in the Y path), respectively. In this way, we achieve a dipole trapping potential with negligible fringes.

We also find that to couple more than a few Watts into the fiber, the fiber needs to be short. For example, the coupling efficiency of a 25 meter fiber starts to drop at 1.5 Watt

input power. For our dipole trapping beams, we use short fibers (2 to 3 meters long) which can take 5 Watt input with up to 83% coupling efficiency.

#### *2.4.2 Improving the intensity stability of the dipole trapping and optical lattice beams*

After achieving a cesium BEC, we would like to produce it with stable atom number. Since our evaporation uses the trap-tilting scheme [28], the stability of final trap depth (crucial for the final atom number) is determined by the intensity stability of the dipole trapping beams. Similarly, optical lattice experiments also require a precise and stable control of the lattice depth (via the retro-reflected intensity). Thus we decided to lock the intensities for all the dipole trapping and optical lattice beams at 1064 nm for two purposes: (1) to achieve a reproducible control, (2) to suppress the noise.

Because we control the beam intensity by controlling the AOM diffraction efficiency, the suppression of low-frequency intensity noise (which atoms are most sensitive to) will be ultimately limited by the bandwidth of the AOMs (“the actuator”). Thus we upgrade the AOMs for higher bandwidth, replacing all the slow Isomet AOMs (at 1064 nm) with the much faster Crystal Technology AOMs (97-02848-01) which can switch on and off the diffracted beam power within 4  $\mu$ s.

The dipole trapping beams are locked based on pick-up signals from fast linear photodiodes (with about 2 MHz bandwidth). The intensity noise with the lock is the same for different intensities, and corresponds to less than 0.1% of the full intensity.

The lattice beams are locked based on pick-up signals from logarithmic photodiodes which provide a large dynamic range (larger than  $10^5$ ). The bandwidth of a logarithmic photodiode is mainly determined by the performance of the logarithmic converter in the

amplifying circuit (for which we choose Digikey AD8304). The dynamic range not only depends on the performance of the logarithmic converter, but also depends on two properties of the photodiode: (1) the responsivity at a particular wavelength and (2) the dark current that limits the lowest detectable light level. We use an InGaAs photodiode (G8376) in the X-lattice path and a silicon photodiode (S5971) in the Y-lattice path. The bandwidth of the photodiode decreases as the input light intensity decreases. For moderate light levels, the retro-beam intensity has a common percentage stability.

While we lock the intensity to suppress the low-frequency noise, we compromise the switching speed of the beam. When the intensity is in-lock, the typical rise / fall time is on the order of  $25 \mu\text{s}$ .

### *2.4.3 Upgrading the imaging for a higher resolution*

High imaging resolution is important for probing a number of topics in many-body physics, such as the local fluctuations and correlations. In order to improve our imaging resolution, recently (2011/12) we changed the vertical imaging setup by replacing the commercial microscope objective and tube lens with a custom-made microscope assembly. The design of the new objective has two improvements: firstly, it takes into account aberrations caused by the finite thicknesses of optics between atoms and objective; secondly, the numerical aperture (N.A.) increases from 0.28 to 0.5, reducing the diffraction limited radius from  $1.8 \mu\text{m}$  to  $1.0 \mu\text{m}$ . Tests using a resolution target (with the 1951 USAF test pattern) estimate a resolution of  $1.3 \mu\text{m}$ . Tests based on the atoms is in progress and should have results soon.

# CHAPTER 3

## MAKING, PROBING, AND UNDERSTANDING TWO-DIMENSIONAL ATOMIC QUANTUM GASES

In this chapter, we present a series of experiments on making, probing, and understanding two-dimensional (2D) atomic quantum gases. These experiments provide the essential tools and knowledge for preparing and studying atomic samples in the quantum critical regime.

### 3.1 Accelerating evaporative cooling of atoms into Bose-Einstein condensation in optical traps

In this section, we discuss a simple scheme to achieve fast, accelerating (runaway) evaporative cooling of optically trapped atoms by tilting the optical potential with a magnetic field gradient. Runaway evaporation is possible in this method due to the weak dependence of vibration frequencies on trap depth, which preserves atomic density during the evaporation process. Using this scheme, we show that Bose-Einstein condensation with  $\sim 10^5$  cesium atoms can be realized in  $2 \sim 4$  s of forced evaporation. The performance is in sharp contrast to  $> 20$  s of evaporation time if we adopt conventional cooling method by reducing the dipole beam intensity. The evaporation speed and energetics of this new scheme are consistent with the three-dimensional evaporation picture, despite the fact that atoms can only leave the trap in the direction of tilt.

This section is based on our published work (by C.-L. Hung, X. Zhang, N. Gemelke, and C. Chin) in *Phys. Rev. A*, **78**, 011604(R) (2008). Copyright (2008) by the American Physical Society.

### 3.1.1 Introduction

The possibility to manipulate Bose-Einstein condensates (BECs) and degenerate Fermi gases of cold atoms in optical traps opens up a wide variety of exciting research; prominent examples include spinor condensates [35], Feshbach resonance in cold collisions [36], and BECs of molecules [37, 38]. In many early experiments, condensates were first created in a magnetic trap and subsequently transferred to an optical dipole trap. These experiments could be greatly simplified after direct evaporation to BEC in optical traps was demonstrated [39]. In this section, we describe a further improvement on dipole-trap based evaporation, which allows for runaway cooling without significant increase in trap complexity.

Evaporative cooling proceeds by lowering the depth of a confining potential, which allows atoms with high kinetic energy to escape and the remaining particles to acquire a lower temperature and higher phase space density through rethermalization. Starting from a sample of precooled atoms in a dipole trap, one can perform forced evaporative cooling on optically trapped atoms by constantly reducing the trap depth until quantum degeneracy is reached. This method has been successful in creating rubidium BEC in a dipole trap [39], and has become a critical component in recent experiments on quantum gases of Cs [40], Li [41], K [42] and Yb [43]. In all these experiments, forced evaporative cooling in the dipole trap is realized by reducing the intensity of the trapping beam, and consequently also the restoring forces. In later discussion, we will refer to this approach as the trap-weakening scheme.

Evaporative cooling in optical traps remains one of the most time-consuming and technically challenging steps in condensate production. Fundamentally, this is due to the fact that cooling by weakening the trapping potential inevitably reduces the collision rate. Here runaway (accelerating) evaporation is essentially impossible even with perfect evaporation

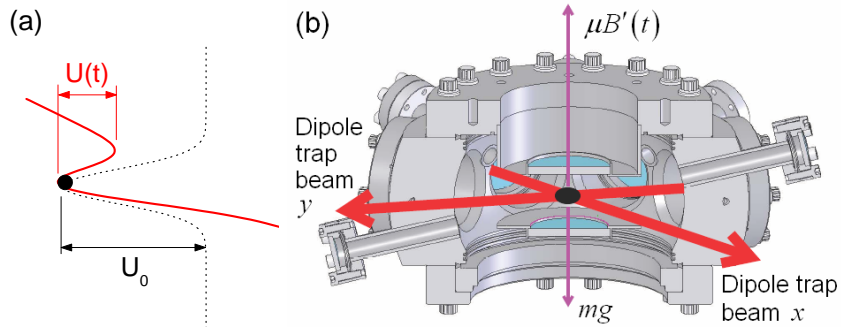


Figure 3.1: Trap-tilt based evaporation and experimental apparatus. (a) Trap depth  $U$  decreases when an external potential gradient is applied to the optically trapped atoms. (b) Apparatus for evaporation of cesium atoms (black dot) in a crossed-beam dipole trap. A strong, slowly-varying magnetic field gradient  $B'(t)$  over-levitates the atoms with magnetic moment  $\mu$  against gravitational pull  $mg$  and evaporates them upward.

efficiency and purely elastic collisions<sup>1</sup>. Within experimentally accessible times, the trap-weakening method puts a severe limit on the maximum gain in phase space density one can reach. Several auxiliary schemes have been successfully implemented in order to increase the evaporation speed, including the dimple trap [40] and a zoom lens system [45]. These methods often increase the complexity of the apparatus or require delicate optical alignment or manipulation.

In this section, we report a simple evaporative cooling scheme which can be immediately implemented in many existing experiments. Instead of reducing the intensity of the trapping beam, we reduce the trap depth by applying an external force on the optically trapped atoms, see Fig. 3.1a. This trap-tilting method entails only a weak reduction in confinement strength over a large range of potential depth and can significantly speed up the cooling process. Using this method, we demonstrate runaway evaporative cooling in a large volume dipole trap and reach Bose-Einstein condensation of cesium significantly faster than previous results [46]. Finally, we comment on the conditions for runaway evap-

1. The only possible runaway evaporation in a weakening trap is on resonant Fermi gas, see Ref. [44]

oration in a tilted trap and investigate the dimensionality of atomic energy selection in the evaporation.

### 3.1.2 *Experimental setup and procedures*

For this study, cesium atoms are first slowed by a Zeeman slower, collected in a magneto-optical trap (MOT) for 2 s, molasses pre-cooled, and finally cooled and spin polarized by degenerate Raman-sideband cooling (dRSC) [47] to the lowest hyperfine ground state  $|3, 3\rangle$ . A crossed dipole trap and magnetic field gradient are employed to levitate and collect the cooled atoms. The dipole trap is formed by intersecting two laser beams on the horizontal ( $x-y$ ) plane; both beams are extracted from a single-mode, single frequency Yb fiber laser operating at the wavelength of 1064 nm, frequency offset by 80 MHz, focused to a  $1/e^2$  beam diameter of 540  $\mu\text{m}$  (620  $\mu\text{m}$ ) and power of 1.9 W (1.6 W) in the  $y-(x-)$  direction. In the absence of trap tilt, the trapping frequencies near the bottom of the potential well are  $(\omega_x^0, \omega_y^0, \omega_z^0) = 2\pi \times (17, 34, 38)$  Hz. During the dipole trap loading process, we switch on a uniform magnetic field of 58 G in the (vertical)  $z$ -direction to improve the atom number following the loading process and apply a levitating magnetic field gradient of  $B'_c = mg/\mu = 31.3$  G/cm, where  $mg$  is the gravitational force,  $\mu = 0.75 \mu_B$  is the magnetic moment of the atoms in  $|3, 3\rangle$ , and  $\mu_B$  is the Bohr magneton. After 1 s of thermalization and self-evaporation in the dipole trap, we ramp the magnetic field to 20.8 G, where three-body loss is minimized [48], and the field gradient to 37.8 G/cm in 1.85 s and begin our study on forced evaporation. At this point, which we define as time  $t = 0$ , there are  $N_0 = 1.9 \times 10^6$  atoms in the trap with a temperature of  $T_0 = 470$  nK, peak atomic density of  $n = 3.8 \times 10^{12}$   $\text{cm}^{-3}$ , and peak collision rate of  $\Gamma_0 = 133$  /s. The background collision rate is below 1/60 s.

We perform forced evaporative cooling by linearly increasing the magnetic field gradi-

ent  $B'$  from 37.8 to 41.4 G/cm in 2.2 s and then to 43.5 G/cm in another 3 s, which reduces the calculated trap depth from 3.0  $\mu\text{K}$  to 1.0  $\mu\text{K}$  and then to 170 nK. The magnetic field and dipole trap intensity are kept constant throughout the process. To evaluate the cooling performance, we interrupt the evaporation at various times to measure the particle number  $N$ , temperature  $T$  and trap frequencies  $\omega_{x,y,z}$ . Particle number and temperature are extracted from absorption images taken at low magnetic fields, following a 70 ms time-of-flight expansion at  $B = 17$  G to minimize the collisions and  $B' = B_c$  to levitate the atoms. Trap frequencies are measured from small amplitude oscillations of the atomic momentum by abruptly displacing the trap center. Peak phase space density is calculated from  $\phi = n\lambda_{dB}^3$ , where  $n = N\omega_x\omega_y\omega_z(m\lambda_{dB}/h)^3$ ,  $\lambda_{dB} = h(2\pi mk_B T)^{-1/2}$  is the thermal de Broglie wavelength,  $k_B$  is the Boltzmann constant and  $h$  is the Planck constant. Collision rates are calculated as  $\Gamma = n\langle\sigma v\rangle$ , where the elastic collision cross section is  $\sigma = 8\pi a^2$ , scattering length at 20.8 G is  $a = 200 a_0$  [49], and  $\langle v\rangle = (16k_B T/\pi m)^{1/2}$ .

After 4 s forced evaporative cooling, we observe Bose-Einstein condensation from the appearance of bimodality and anisotropic expansion in time-of-flight images. At this point, the temperature is 64 nK and total particle number is  $5 \times 10^5$ . An almost pure condensate with  $10^5$  atoms was obtained after another 2.5 s. In this evaporation process, the mean truncation parameter is calculated to be  $\bar{\eta} = \langle U/k_B T\rangle = 6.5(3)$ , and the evaporation efficiency is  $\bar{\gamma}_{ev} = -\log(\phi/\phi_0)/\log(N/N_0) = 3.4$ . We observe an increasing collision rate and accelerating evaporation, indicating achievement of runaway evaporation; see Fig. 3.2.

An alternative evaporation path is developed to minimize the time to reach BEC. After a shorter magnetic field ramping process of 1 s, we ramp the field gradient from 38.9 G/cm at  $t = 0$  to 41.3 G/cm in 0.5 s and then to 43.5 G/cm in another 1.5 s. Here we reach BEC in as short a period as 1.8 s of forced evaporation. Another 1 s evaporation allows us to obtain  $4 \times 10^4$  atoms in an almost pure condensate, see Fig. 3.2(d). Despite the rapid increase of phase space density, the collision rate actually decreases by 25% at the end of

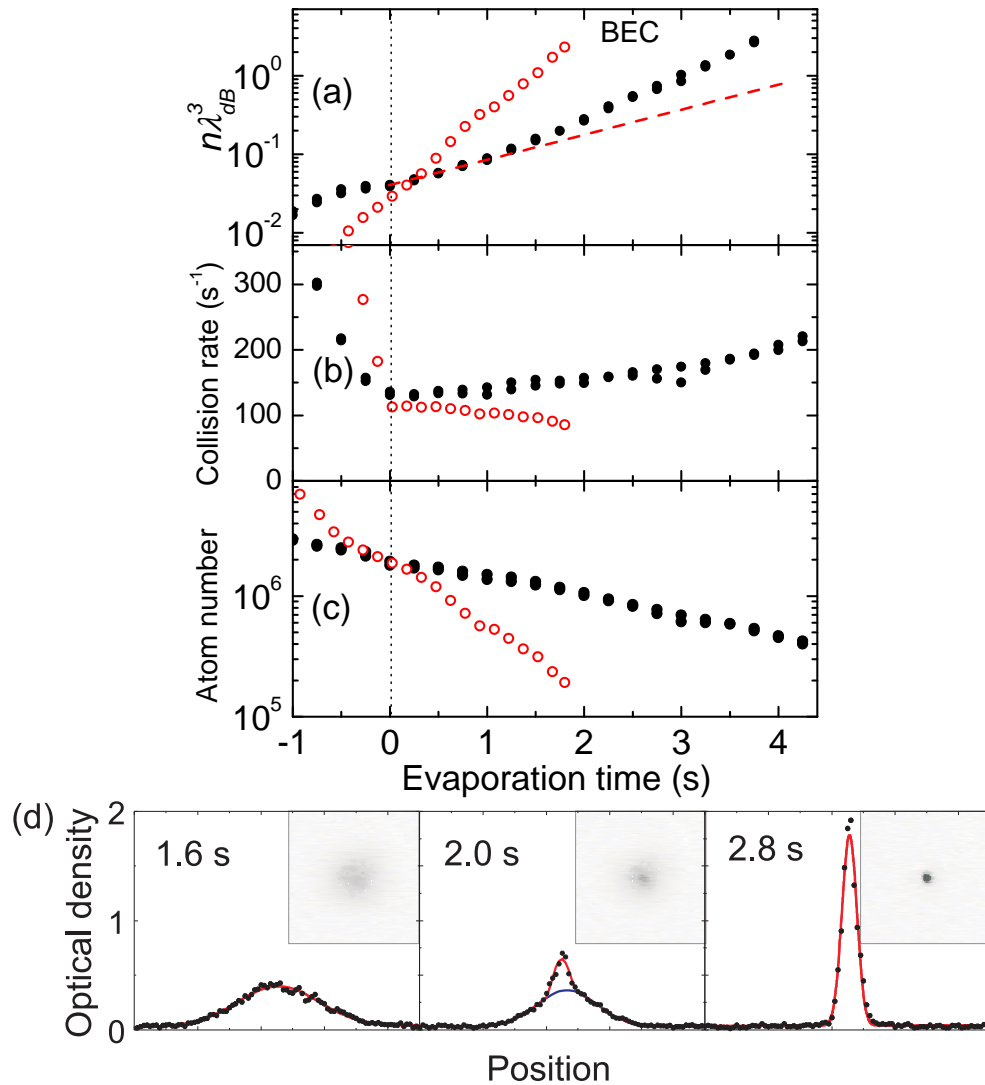


Figure 3.2: Performance of trap-tilting based forced evaporation: (a) phase space density, (b) collision rate, (c) particle number and (d) density profile. Two evaporation paths: 4 s (solid dots) and 1.8 s (open circles) are shown. The dashed line in (a) shows simple exponential increase. In (d), time-of-flight absorption images and single-line optical density profiles are taken from the 1.8 s evaporation path. The expansion time is 70 ms, and the field of view is  $1.2 \text{ mm} \times 1.2 \text{ mm}$ .

evaporation. The truncation parameter and evaporation efficiency are  $\bar{\eta} = 4.6$  and  $\bar{\gamma}_{ev} = 1.9$ , respectively.

Throughout both evaporation processes, the peak density is moderate,  $n < 1.5 \times 10^{13} \text{cm}^{-3}$ . The collision loss rate, dominated by three-body recombination process [48], is below 1/40 s at 20.8 G. Trap loss from collisions is negligible in the following discussion.

### 3.1.3 Advantage of the trap tilting scheme

To understand the advantage of the trap-tilting scheme, we analyze how the trap frequency is modified in a model Gaussian potential during the evaporative cooling process. We combine the magnetic gradient potential and the gravitational potential as  $-\gamma mgz$ , where  $\gamma = B'/B'_c - 1$ . The total potential  $V(x, y, z)$  can be modeled as

$$V = -\frac{U_0}{2} [e^{-2(x^2+z^2)/w^2} + e^{-2(y^2+z^2)/w^2}] - \gamma mgz, \quad (3.1)$$

where the first two terms come from the two horizontal trapping beams, and the last term is the tilt potential. Here, we assume the two beams have the same beam waist  $w$  and peak light shift  $U_0/2$  for convenience.

We introduce the tilt parameter  $\zeta = \sqrt{e}\gamma mgw/2U_0$  to parameterize the trap depth  $U$  and trap frequencies  $\omega_{x,y,z}$ . Using Eq. 3.1, the trap depth and frequencies are evaluated as a function of  $\zeta$ , as shown in Fig. 3.3(a). All quantities are normalized to those of an untilted potential, where the trap depth is  $U_0$ , and the trap frequencies  $\omega_z^0 = \sqrt{2}\omega_x^0 = \sqrt{2}\omega_y^0 = \sqrt{4U_0/mw^2}$ . Note that the trap is unstable when  $\zeta \geq 1$ . In the range of  $10^{-3} < U/U_0 < 1$ , the geometric mean of the trap frequencies  $\bar{\omega} = (\omega_x\omega_y\omega_z)^{1/3}$  varies with the trap depth

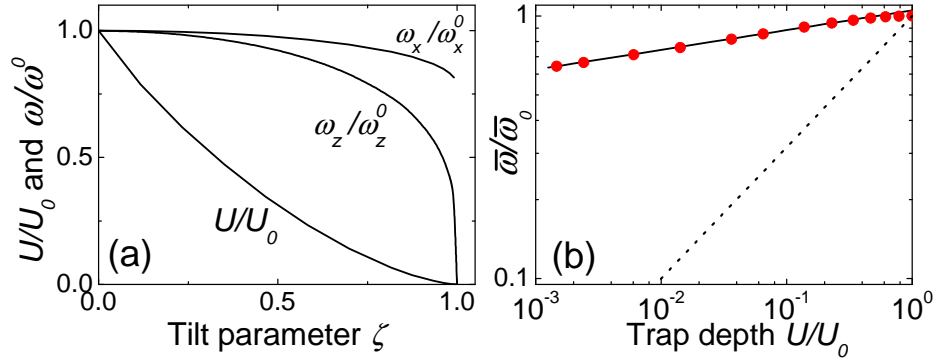


Figure 3.3: Depth and oscillation frequency of a tilted trap. (a) shows the calculated normalized trap depth and frequencies  $\omega_z$  and  $\omega_x = \omega_y$  as a function of the tilt  $\zeta$ , based on Eq. (1). In (b), mean trap frequencies are plotted against the trap depth for a tilted trap (solid dots) and for a weakened trap (dotted line). The solid line shows a power-law fit to the mean frequency, see Eq. (2).

approximately as, see Fig. 3.3(b),

$$\frac{\bar{\omega}}{\bar{\omega}_0} \approx 1.05 \left( \frac{U}{U_0} \right)^{0.075(1)}, \quad (3.2)$$

where  $\bar{\omega}_0$  is the mean frequency of an untilted trap.

The key to fast, runaway evaporation in the tilted trap lies in the gentle, almost negligible weakening of the trap confinement when the trap depth decreases. As the trap depth reduces by a factor of 100, the trap frequency only decreases by 45% in the  $z$ -direction and 14% in the other two directions, in contrast to the trap-weakening method, which reduces trap frequencies by a factor of 10 under the same condition. In general, a weakening trap with  $\bar{\omega} \propto U^\nu$  and  $\nu = 0.5$  shows a much stronger dependence on the trap depth than the tilting trap with  $\nu = 0.075$ .

The collision rate in a harmonic trap depends on the particle number, trap frequencies and temperature. Assuming the truncation parameter  $\eta = U/k_B T$  is kept constant during

the cooling process, we have

$$\begin{aligned}\Gamma &\propto N\bar{\omega}^3 T^{-1} \\ &\propto U^{1/\alpha} U^{3\nu} U^{-1} \equiv U^\beta,\end{aligned}\tag{3.3}$$

where  $\beta = 1/\alpha + 3\nu - 1$ , and  $\alpha > 0$  parameterizes the cooling efficiency by removing atoms [50]. Following the calculation in Ref. [51], with the trap frequency versus trap depth dependence,  $\bar{\omega} \propto U^\nu$ , we derive

$$\alpha = \frac{N}{T} \frac{dT}{dN} = \frac{\eta + \kappa - 3}{3 - 3\nu},\tag{3.4}$$

and  $\kappa > 0$  depends on the dimension of evaporatoin as discussed below.

The condition for runaway evaporation is then given by  $\beta < 0$ . For the trap weakening scheme with  $\nu = 1/2$ ,  $\beta$  is positive for all  $\eta$ . Runaway evaporation is thus impossible. For the tilting scheme with  $\nu = 0.075$ , the exponent  $\beta$  is negative when  $\alpha > 1.08$  ( $\eta > 5.4$ , shown in later discussion), suggesting runaway evaporation with increasing collision rate is possible.

### 3.1.4 Performance of evaporation using the trap tilting scheme

Time evolution of the phase space density  $\phi(t)$  can now be derived based on standard evaporation theory (Ref. [50]). Assuming energetic atoms can leave the sample in all directions, we have

$$\phi(t) = \phi(0)(1 + \lambda\alpha\beta\Gamma_0 t)^{2/\beta-1},\tag{3.5}$$

and for  $\eta > 6$ ,  $\kappa_{3D} \approx (\eta - 5)/(\eta - 4)$  [51, 52]. Here  $\Gamma_0$  is the initial collision rate and  $\lambda_{3D} \approx (\eta - 4)e^{-\eta}/\text{sqrt}2$  [51, 52] is the fraction of collisions producing an evaporated

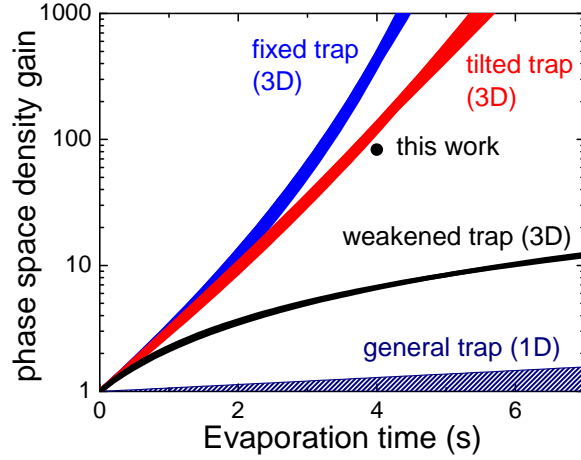


Figure 3.4: Evaporation speed: experiment (4 s path, solid dot) and models. We assume an initial collision rate of  $\Gamma_0=133$  /s,  $\eta = \bar{\eta} = 6.2 \sim 6.8$  and no collision loss. Shaded area covers the 1D evaporation region with  $0 \leq \nu \leq 1$  and all possible  $\eta$ .

atom. Here we see that a negative  $\beta < 0$  leads to a faster-than-exponential growth of the phase space density, which eventually diverges at time  $t = (-\lambda\alpha\beta\Gamma_0)^{-1}$ . We compare the models and our experiment result in Fig. 3.4. To reach the same final phase space density, the trap-tilting scheme would require a much shorter evaporation time than the weakening scheme. For comparison, a potential with fixed trap frequency ( $\nu = 0$ ), e.g., radio-frequency based evaporation in magnetic traps, permits an even stronger runaway effect, see Fig. 3.4.

### 3.1.5 Dimensionality of evaporation using the trap tilting scheme

Remarkably, the performance of our evaporation is consistent with the 3D evaporation model. The consistency of our evaporation speed with the 3D model is somewhat surprising. In a strongly tilted trap where hot atoms can only escape the trap in the tilted direction (see Fig. 3.5), it is generally expected that the evaporation will exhibit performance consistent with one dimensional evaporation. In momentum space, atoms allowed to evaporate

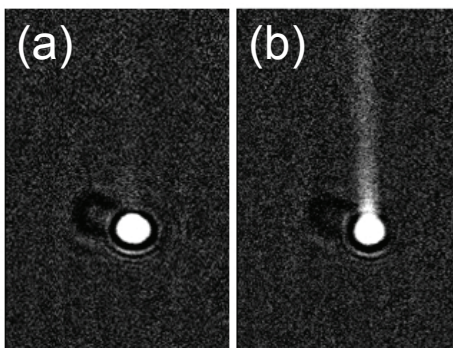


Figure 3.5: Snapshot of in situ atomic distribution during (a) slow and (b) fast evaporation processes. Hot atoms leave the trap in the upward direction due to a strong vertical magnetic force.

along the direction of tilt, with  $p_z^2 \sim 2mU$ , spans a small transverse area  $2\pi mk_B T$ , due to thermal motion in the transverse direction. Compared this area to that of a full evaporating sphere  $8\pi mU$ , one estimates a reduction in the evaporation rate by a factor of  $4\eta$  [53, 50] and thus  $\lambda_{1D} \approx \lambda_{3D}/4\eta$ . Performance of 1D evaporation for all possible  $\eta$  is shown in the shaded area in Fig. 3.4. Our experiment result exhibits evaporation speeds much faster than the any 1D prediction.

We suspect 3D-like evaporation in a tilted trap results from the inseparability of the potential and the existence of a saddle point located at the rim of the potential barrier, which can lead to stochastic single particle motion [53]. When atoms with sufficiently high energy are created by collisions, stochastic motion can allow them to efficiently find escape trajectories. If the energetic atoms have a high probability to escape, regardless of their initial direction of motion, evaporation is effectively three dimensional [53]. In realistic models, stochastization may also be induced by the intensity irregularities of the trapping laser beams.

To further investigate the “dimension of evaporation” in a tilted trap, we come back to

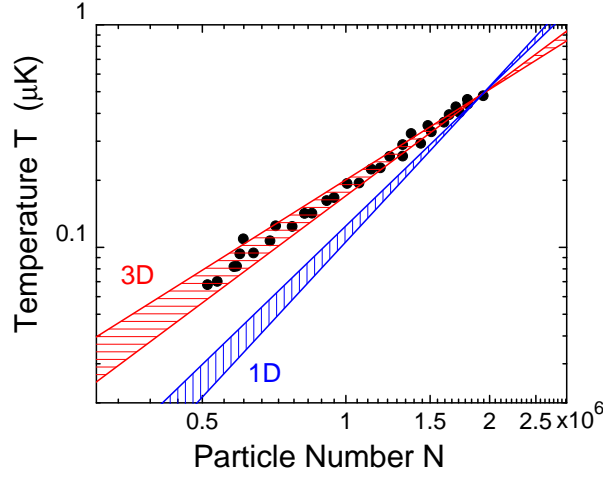


Figure 3.6: Temperature and particle number dependence. Based on the 4 s evaporation data (solid circles), the temperature shows a power-law dependence on particle number  $T \propto N^\alpha$ , with  $\alpha = 1.46(2)$ . For comparison, predictions from 3D and 1D evaporation models are shown using our experiment initial condition and  $\eta = 6.5 \pm 0.3$ .

$\eta + \kappa$ , which parameterizes the energy removed by evaporating a single atom, or

$$\eta + \kappa = -(k_B T)^{-1} dE/dN. \quad (3.6)$$

For 3D evaporation, we expect  $\kappa_{3D} \approx (\eta - 5)/(\eta - 4)$ , which is  $\kappa_{3D} = 0.6(1)$  for our parameter  $\bar{\eta} = 6.5(3)$ ; for 1D evaporation, energy selectivity applies to the axial, but not the transverse motion, which has a mean energy of  $2 k_B T$  per particle (shown to be  $7/4 k_B T$  with careful calculation in Ref. [54]). Hence, we expect a higher energy removed per particle with  $\kappa_{1D} = \kappa_{3D} + 2 = 2.6(1)$  for our parameter [54]. Experimentally, we can test these predictions by evaluating the cooling efficiency  $\alpha$ , which has a simple dependence on  $\kappa$  as shown in Eq. 3.4. We show in Fig. 3.6 that our 4 s evaporation data is excellently fit to the power-law function with  $\bar{\alpha} = 1.46(2)$ . Using Eq. 3.4, we derive  $\kappa = 0.6(3)$ , which is consistent with the 3D value and confirms the 3D nature of the trap-tilt based evaporation.

### 3.1.6 *Applying the trap-tilting scheme in later experiments*

In all later experiments, the evaporation based on trap-tilting scheme produced almost pure BECs with sufficient atom numbers ( $2 \sim 3 \times 10^4$  is enough for 2D gas experiments) and enabled fast experiment cycles. Since the scheme works for both upward trap-tilting and downward trap tilting, we chose to evaporate downward by gradually ramping off the magnetic gradient (which levitates cesium atoms in the  $|3, 3 \rangle$  state) such that at the end of evaporation, we achieve an almost pure condensate in a uniform magnetic field.

## **3.2 *In situ* observation of incompressible Mott-insulating domains in ultracold Bose gases with optical lattices**

The observation of the Superfluid (SF) to Mott-insulator (MI) phase transition of ultracold atoms in optical lattices [55] was an enabling discovery in experimental many-body physics, providing the first tangible example of a quantum phase transition (one that occurs even at zero temperature) in an ultracold atomic gas. For a trapped gas, the spatially varying local chemical potential introduces multiple quantum phases into a single sample, complicating the interpretation of bulk measurements [55, 56, 57, 58, 59]. Here, we report spatially resolved, *in situ* imaging of a two-dimensional ultracold atomic gas as it crosses the SF to MI transition, providing unprecedented and direct access to individual characteristics of the insulating, superfluid and normal phases. We present results for the local compressibility in all phases, showing a strong suppression in the insulator domain, and observe suppressed density fluctuations for the MI in accordance with the fluctuation-dissipation theorem. Furthermore, we obtain a direct measure of the finite temperature of the system. Taken together, these methods make possible a highly complete characterization of multiple phases in a strongly correlated Bose gas, and of the interplay between quantum and thermal fluctuations in the quantum critical regime.

This section is based on our published work (by N. Gemelke, X. Zhang, C.-L. Hung, and C. Chin) in *Nature* **460**, 995 (2009).

### 3.2.1 Introduction

Since its theoretical inception [60, 61, 62], two of the most celebrated properties of the bosonic Mott insulator have been its incompressibility and suppression of local density fluctuations [63], induced by the enhanced importance of inter-particle repulsion for particles subject to a strong lattice potential. The result for a trapped atom gas is the remarkable “wedding-cake” density profile, where successive MI domains are manifest as plateaus of constant density. Related phenomena have been studied through the coherence [55, 56], transport [55, 57], noise correlations [58], and number variance [55, 59], but direct observation of the incompressibility has proven difficult due to the inhomogeneous nature of all experiments to date, and to the technical difficulty of making spatially resolved measurements. Innovative experimental efforts incorporating tomographic imaging and other advanced techniques have yielded evidence [23, 64] that shell structure exists in the Mott insulator regime, though none has directly observed the incompressibility of the insulating density plateaus by imaging a complete and single physical system in situ.

We report studies based on direct in-situ imaging of an atomic MI. By loading a degenerate Bose gas of cesium-133 atoms into a thin layer of a two-dimensional optical lattice potential, and adiabatically increasing the optical lattice depth, we observe the emergence of an extremely flat density near the center of the cloud, which corresponds to a MI phase with accurately one atom-per-site. From density profiles, we extract important thermodynamic and statistical information, confirming the incompressibility and reduction of density fluctuations in the MI as described by the fluctuation-dissipation theorem.

### 3.2.2 *Experimental setup and procedures*

The single layer, two-dimensional (2D) optical lattice is formed by two pairs of counter-propagating laser beams derived from a Yb fiber laser at wavelength  $\lambda = 1064$  nm. The pairs are oriented orthogonally on the horizontal ( $x-y$ ) plane, forming a square lattice with site spacing  $d = \lambda/2 = 0.532 \mu\text{m}$ . A weak harmonic potential of  $V_H = m(\omega_x^2 x^2 + \omega_y^2 y^2)/2$  localizes the sample, where  $m$  is the cesium mass, and the geometric mean of the trap frequencies is  $\omega_r = \sqrt{\omega_x \omega_y} = 2\pi \times 9.5\text{Hz}$  (a weak dependence on lattice depth is described in Section 3.2.5). Vertical confinement is provided by an additional vertical optical lattice with a site spacing  $4 \mu\text{m}$ , formed by two beams intersecting at an angle of  $15^\circ$ , confining atoms in a gaussian wavepacket of width (oscillator length)  $a_z = 0.30 \mu\text{m}$ . The sample is loaded into a single site of the vertical lattice, kept deep to prevent vertical tunneling. Tunneling in the horizontal 2D lattice is controlled by varying the lattice depth  $V$  [55]. Details on preparation of the atomic sample can be found in section 3.2.5 and Ref. [28].

We obtain a top view of the sample using absorption imaging, directly revealing the atomic surface density  $n(x, y)$  on the horizontal plane. The imaging resolution is  $3 \sim 4 \mu\text{m}$ , and magnification such that one imaging pixel corresponds to an area of  $(2\mu\text{m})^2$  on the object plane. Unit filling in a 2D optical lattice has a conveniently measurable optical absorption on resonance.

The superfluid-to-Mott insulator (SF-MI) transition of ultracold atoms in an optical lattice is described by the Bose-Hubbard model, characterized by on-site interaction  $U$  and the tunneling  $t$  [62]. In 2D optical lattices, superfluid is converted into a MI when  $U/t$  exceeds 16 [56, 65] near the density of one atom per site. Here, the SF-MI phase transition can be induced by either increasing the lattice potential depth  $V$  (typically measured in units of recoil energy  $E_R = h \cdot 1.3\text{kHz}$ , where  $h$  is Planck's constant) [55, 56, 64] or the atomic interaction strength (characterized by scattering length  $a$ ) via a magnetically-tuned

Feshbach resonance [19], together providing complete, independent control of  $U$  and  $t$ .

### 3.2.3 *Observation of incompressible Mott-insulating domains*

Atomic density profiles in the lattice are shown in Fig. 3.7. For weak lattice depths (superfluid regime), the density profiles are bell-shape, with negative curvature at the center (Fig. 3.7a), indicating a finite, positive compressibility dictated by the interaction coupling constant (discussed below.) In sufficiently deep lattices, we observe a flattened density at the center of the sample (Fig. 3.7b,c), indicating development of a Mott insulating phase with one particle per lattice site. This density plateau, an important feature of the MI phase, arises from incompressibility.

A primary check on the MI is to compare the measured density in the plateau to that corresponding to one atom-per-site, given by MI physics as a “standard candle” of atomic density. Using the known scattering cross-section, correcting for saturation effects (see Section 3.2.5), we determine the plateau density to be  $n = 3.5(3)/\mu\text{m}^2$ , in agreement with the expected value  $1/d^2 = 3.53/\mu\text{m}^2$ .

To distinguish a MI from superfluid or normal gas, we histogram the occurrence of pixels  $h(n)$  in the images corresponding to a density  $n$  with a bin size of  $\Delta n \ll n$ . The MI plateau, containing a large number of pixels with similar atomic density, appears as a peak at  $n = 1/d^2$  (Fig. 3.8a). In general, the occurrence of a particular density  $n$  can be regarded as the rate at which local chemical potential changes with density, multiplied by the number of pixels  $w(\mu)\Delta\mu$  corresponding to a chemical potential between  $\mu$  and  $\mu + \Delta\mu$ . The occurrence at density  $n$  is then

$$h(n) = \Delta n w(\mu)\Delta\mu/\Delta n \approx \Delta n w(\mu)\kappa^{-1}, \quad (3.7)$$

where  $\kappa = \partial n/\partial\mu$  is the local compressibility [66]. In a harmonic trap,  $w(\mu) = 2\pi/md^2\omega_r^2$

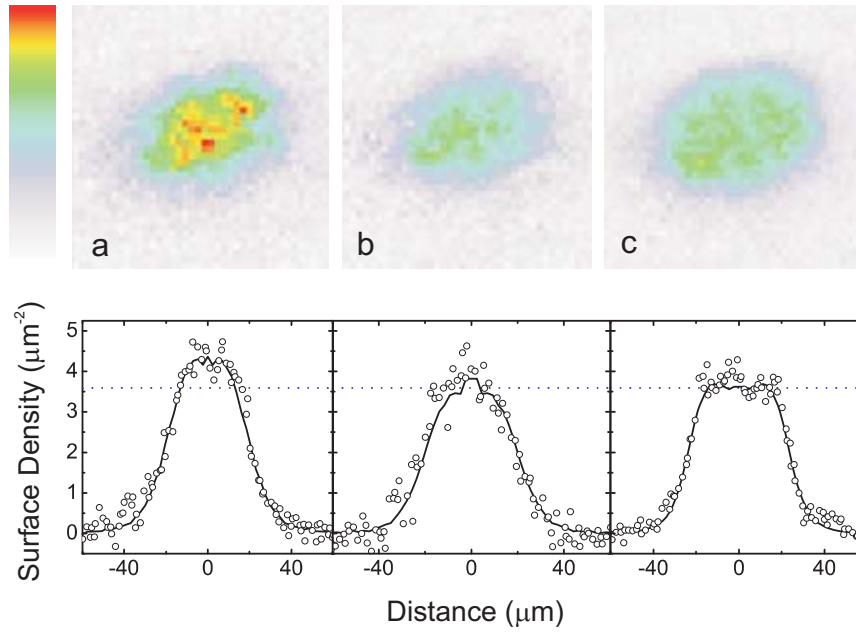


Figure 3.7: False color absorption images and line cuts along major axis of density profiles for  $N = 7500$  ultracold cesium atoms at scattering length  $a = 310 a_B$  in a 2D optical lattice. (a) Superfluid regime (shallow lattice  $V = 2.4E_R$ ), (b) Phase transition regime (medium lattice depth  $V = 9.4E_R$ ), and (c) Mott insulator regime (deep lattice  $V = 22E_R$ ). Images are averaged over three experiment repetitions. Colorbar shows linear variation with density from zero to peak value of  $5.4\mu\text{m}^{-2}$ . Line cuts are taken along the major axis, and compared to radial average of density (solid line) over the entire image as described in text. The blue horizontal line indicates the density of one atom per site.

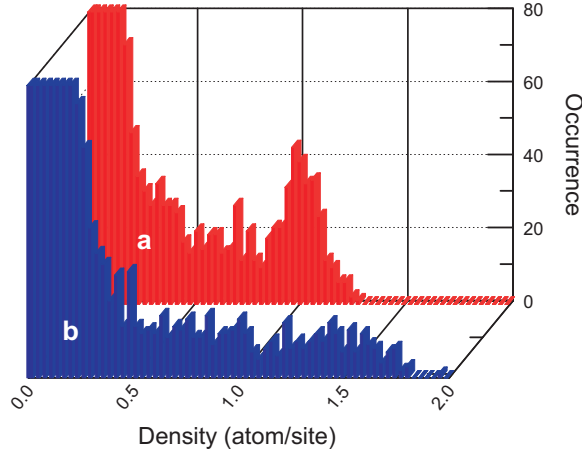


Figure 3.8: Histograms of density profiles in the MI regime (a,  $V = 38E_R$ ,  $a = 460a_B$ ) and the superfluid regime (b,  $V = 0.5E_R$ ,  $a = 460a_B$ .) The histograms are based on an average of three density images. The bin size is  $\Delta n = 0.03$ .

is constant, and the histogram is a particularly useful tool to distinguish different phases. For a pure BEC in the Thomas-Fermi limit, the compressibility is constant to the maximally-allowed density  $n_{pk}$ , and results in a constant  $h(n)$  for  $n \leq n_{pk}$  (see Fig. 3.8b for  $0.5/d^2 < n < 1.5/d^2$ ). For the MI, the density is insensitive to chemical potential in a narrow range near  $n = 1/d^2$ , indicating a vanishing compressibility, and thus a sharp histogram peak at  $n = 1/d^2$ . The peak's presence in Fig. 3.8a is thus directly related to the incompressibility in the Mott phase. Finally, the compressibility of a normal (ideal) gas is proportional to its density, thus  $h(n) \propto 1/n$ , leading to the strong upturn at low densities in Fig. 3.8a,b for both regimes.

Much more information can be obtained from the density profiles, as recently suggested in Ref. [20]. For example, the compressibility in a two-dimensional cylindrically symmetric trap can be written

$$\kappa = \partial n / \partial \mu = -n'(r) / (rm\omega_r^2), \quad (3.8)$$

where we have assumed the local density approximation, and that the chemical potential depends on the trapping potential  $\mu = \mu_0 - V_H(r)$ . For a BEC in the Thomas-Fermi regime,

the compressibility is positive and constant,  $\kappa_{BEC} = 1/g$ , where  $g = \sqrt{8\pi}a\hbar^2/ma_z$  is the (2D) interaction parameter[67]. We can thereby relate the measured compressibility to that of a BEC as

$$\frac{\kappa}{\kappa_{BEC}} = -\left(\frac{2}{\pi}\right)^{7/2} \frac{n'(r)}{rd^{-4}} \frac{a}{a_z} \left(\frac{E_R}{\hbar\omega_r}\right)^2. \quad (3.9)$$

We evaluate  $\kappa$  from azimuthally averaged density profiles (Fig. 3.9a). Eccentricity of the trap is corrected by rescaling the principal axes as determined from the density profile, and verified to be consistent with direct measurement of trap frequencies. Due to the singular nature of  $n'(r)/r$  near the center, we evaluate  $\kappa$  there by fitting  $n(r)$  to a quadratic,  $n(r) = n(0) - \alpha r^2$ . The curvature then gives the compressibility as  $\kappa(0) = 2\alpha/m\omega_r^2$ , for which we obtain  $\kappa/\kappa_{BEC} = 0.34(10)$  in a weak lattice and  $\kappa/\kappa_{BEC} = 0.013(6)$  in a strong lattice (See Fig. 3.9). In the weak lattice (SF regime), the finite and constant compressibility at the center agrees with expectation for the superfluid phase, though lower than expected, which we attribute to finite temperature and calibration of trap parameters. The finite temperature is also clear in the exponential tail of the density profile and the compressibility [68], from which we derive the temperature 10(2) nK in the superfluid regime ( $V = 0.3E_r$ ) and 15(3) nK in the MI regime ( $V = 22E_r$ ).

In a deep lattice (MI regime), we observe a strong reduction of the compressibility in the trap center, below that in the superfluid phase for the weak lattice, strongly supporting the emergence of a MI phase at the center of the sample. Away from center,  $\kappa$  suddenly increases at  $r = 20d$ , then decreases for  $r > 40d$ . The exponential decay is again consistent with a normal gas. Between MI and normal gas ( $20d < r < 40d$ ), a more detailed measurement and model of compressibility would be necessary to identify the local phase.

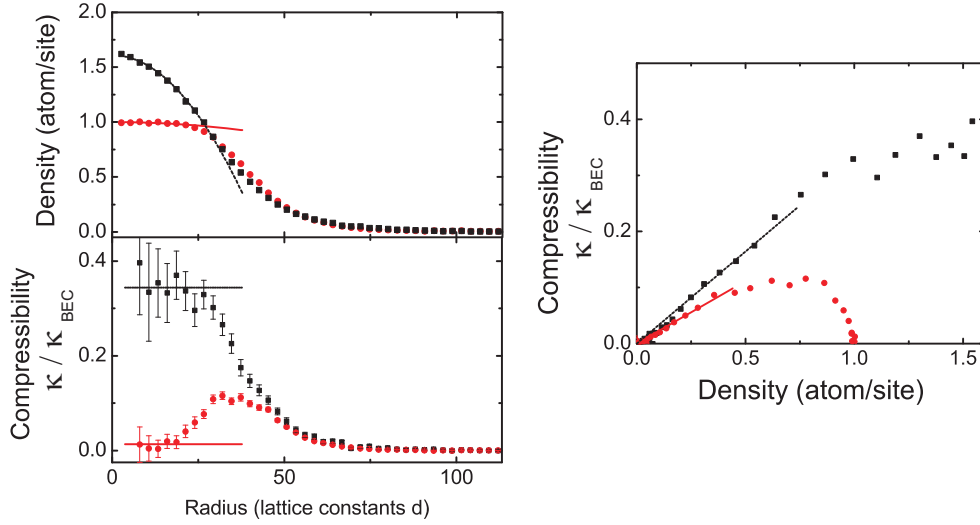


Figure 3.9: Extraction of compressibility from density profiles. (a) Radially averaged profiles (3 images) in the superfluid (black squares:  $V = 0.3E_R$ ,  $N = 7200$ ) and MI (red circles:  $V = 22E_R$ ,  $N = 6700$ ), with  $a = 310a_B$ . A quadratic fit to the sample's center extracts the curvature near  $r = 0$ . (b) Normalized compressibilities derived from (a) using Eq. (1) in the superfluid (black squares) and MI (red circles) regimes. The horizontal lines indicate compressibility near  $r = 0$ , estimated from the quadratic fits in (a). Rising compressibility at  $r = 30d$  marks the MI boundary. (c) The dependence of compressibility on atomic density. Linear dependence at low densities (normal gas) is best fit by solid lines. Error bars indicate standard error in the mean.

### 3.2.4 *Qualitative comparison with the fluctuation-dissipation theorem*

Within the local density approximation, one may consider any small area of the sample as a thermodynamic subsystem in a grand-canonical ensemble, assumed to be in equilibrium with the remainder of the gas. One can then invoke the fluctuation-dissipation theorem (FDT) (see e.g. Refs. [66, 69]) to ascertain that incompressibility necessarily implies a low local particle number fluctuation; this relationship takes the form

$$\delta n^2 \approx \kappa k_B T \quad (3.10)$$

Resolved in-situ imaging provides an enticing opportunity to measure fluctuations of the local density [70, 63], and thus check the validity of the FDT. We measured fluctuations by recording multiple absorption images, calculating the variance of density measured in each pixel (each collects signals from a patch of  $(2\mu m/d)^2 \approx 14$  lattice sites). Fig. 3.10 shows the recorded fluctuations, where pixels are binned according to their mean atomic density. Fluctuations consist of detection (photo-electron shot) noise and thermal and quantum atomic density fluctuations. Detection shot noise can be well-calibrated and modeled by analyzing portions of the images with low density; extension to higher optical depth (density) shows the weak dependence illustrated in Fig. 3.10.

Above the detection noise, density fluctuations (see Fig. 3.10) show a strong qualitative agreement with the compressibility presented in Fig. 3.9 as expected from the FDT. For example, the Mott-phase shows a strong suppression of fluctuations at the density of one atom-per-site. The superfluid regime lacks this feature, instead showing a pronounced flattening as the sample transitions from normal gas to superfluid, as expected from the constant compressibility in the superfluid phase (Figure 3c). Finally, at low density, the normal gas shows a temperature-independent fluctuation of  $\delta n = \gamma\sqrt{n}$ , which can be anticipated from Figure 3c, and agrees with the FDT. The coefficient  $\gamma$  is roughly consistent

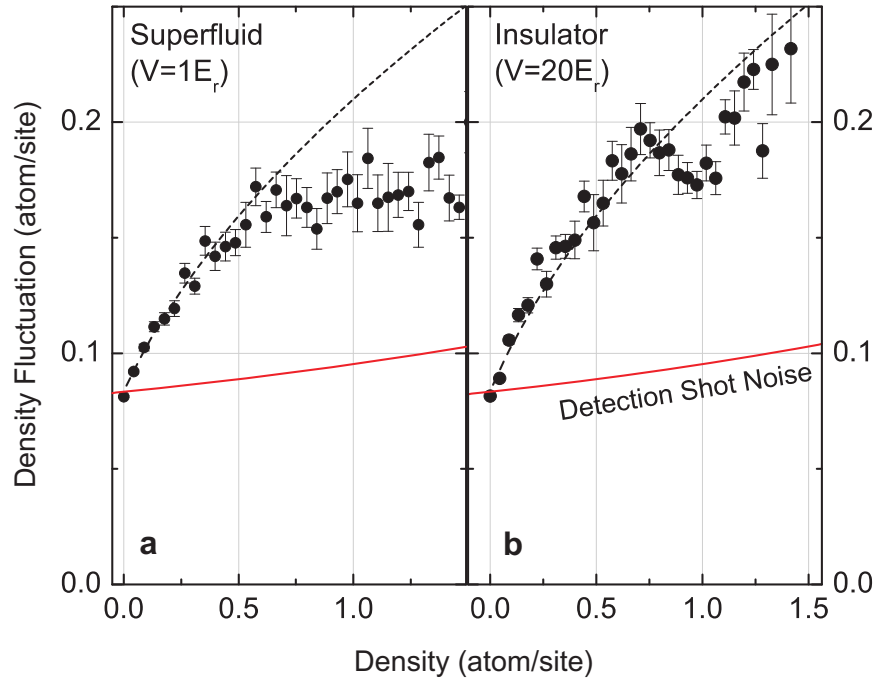


Figure 3.10: The fluctuation of local density extracted from a set of twelve absorption images in the weak (a) and deep (b) lattice regimes. The insulator and superfluid show a pronounced difference at one atom-per-site, where the insulator’s fluctuation is suppressed by incompressibility. In the superfluid, constant compressibility initiates a flattening. At low densities, in both regimes, the fluctuation shows a characteristic  $\sqrt{n}$  dependence, where the gas is presumed to be normal; the dashed line shows best fit  $\sqrt{n}$  dependence. The total number of atoms was  $N = 8300$  (SF) and  $N = 9600$  (MI) with  $a = 310a_B$  for both sets. Error bars indicate standard error in the mean.

with the FDT, and measured imaging resolution (see Section 3.2.5).

### 3.2.5 Detailed procedures and analyses

Cesium Bose condensates are produced by forced evaporative cooling in a crossed beam dipole trap. The condensate is compressed vertically by loading into a single layer of an optical lattice with the scattering length tuned near zero. After this, the lattice is adiabatically instated by controlled retroreflection of dipole trapping beams, and the scattering length brought to its final value. Imaging is performed absorptively along the vertical, calibrated for saturation effects by varying the intensity of the imaging light. Fluctuations of density are calculated for each pixel in a series of images taken at identical experimental parameters, and plotted against the mean density at that pixel. The parameter  $\gamma$  is estimated from a model of the expected averaging of thermal fluctuations over an imaging resolution limited spot.

#### **Preparation of BEC in a thin 2D optical lattice**

The  $^{133}\text{Cs}$  BEC is formed in a crossed-beam dipole trap by an efficient evaporative cooling method [28]. The dipole trap consists of three beams on the horizontal plane: two orthogonal beams at the wavelength of 1064 nm (Yb fiber laser, YLR-20-1064-LP-SF, IPG), focused to  $1/e^2$  radii of  $350\ \mu\text{m}$ , and one  $\text{CO}_2$  laser beam at the wavelength of  $10.6\ \mu\text{m}$  (Gem-Select 100, Coherent), focused to a vertical  $1/e^2$  radius of  $70\ \mu\text{m}$  and horizontal of  $2\ \text{mm}$ . The  $\text{CO}_2$  beam intersects the Yb laser beams at an angle of  $45^\circ$  and provides an enhanced vertical confinement to support the atoms against gravity. With  $N = 10^4$  atoms in a pure condensate, the Thomas-Fermi radii of the condensate are  $(r_x, r_y, r_z) = (23, 14, 3.6)\ \mu\text{m}$ .

After a pure BEC is obtained, the sample is compressed vertically by introducing a

vertical lattice, formed by two laser beams (Mephisto, Innolight) inclined at  $+7.5^\circ$  and  $-7.5^\circ$  relative to the horizontal plane. The vertical lattice has a spacing of  $4 \mu\text{m}$  and, together with the crossed dipole trap, forms an array of 2D oblate “pancake” potentials, with harmonic confinement frequencies of  $850\text{Hz}$  at its maximum depth.

In order to load the condensate into a single pancake trap, we first ramp the magnetic field to  $17.2 \text{ G}$  in  $400 \text{ ms}$ , reducing the s-wave scattering length to  $a < 10 a_B$ , and then turn on the vertical lattice in  $100 \text{ ms}$ . Atomic population in other lattice sites, if any, can be identified by observing an interference pattern in time-of-flight images taken from the side. For this work, we observe a sufficiently weak interference pattern contrast to conclude  $> 98\%$  of the atoms are in a single pancake trap. After the vertical lattice is fully turned on, the  $\text{CO}_2$  laser intensity is ramped to zero in  $100 \text{ ms}$  while the scattering length is ramped to its final value by tuning the external magnetic field.

The 2D lattice potential in the horizontal ( $x$ - and  $y$ -) directions is formed by introducing retro-reflections of the  $1064 \text{ nm}$  dipole trap beams. A continuous evolution from a pure dipole trap (with zero retro-reflection) to a 2D optical lattice (with significant retro-reflection) is achieved by passing each dipole trap beam (after it passes through the atomic cloud once) through two acousto-optic modulators (AOMs) controlled by the same radio-frequency (rf) source, then off a retroreflection mirror. The AOMs induce an overall zero frequency shift, but permit a dynamic control of the retroreflection intensity over six orders of magnitude. To load the lattice to a depth of  $38E_r$ , the retro-reflection intensities are slowly ramped over  $200\text{ms}$  with an exponential waveform of  $36\text{ms}$  time constant. For smaller final lattice depths, the ramp waveform is fixed but duration shortened. Onsite interaction energy  $U$  and tunneling rate  $t$  are evaluated from the measurements of the lattice vibration frequencies and band structure calculation. Envelope trapping frequencies were separately measured by exciting center of mass oscillations, and found to be consistent with orientation and ellipticity of in-situ images of atomic density. A weak variation of the mean

envelope frequency with lattice depth was measured and accounted for by the expression  $\omega_r = \sqrt{\omega_x \omega_y} = 2\pi \times 9.5(1 + V/82E_R)\text{Hz}$ .

### **Calibration of atomic surface density**

By varying the intensity of the imaging beam, we measure the optical depth on resonance in the density plateau using  $OD = \ln(M_0/M)$ , where  $M$  is the number of photons collected by a CCD pixel in the presence of the atoms and  $M_0$  is that without the atoms. The optical depth in the plateau is extracted from a fit to the peak in the histogram. We then fit the variation of peak optical depth assuming  $OD = n\sigma/(1 + M_0/M_{sat})$  to determine the depth in the zero intensity limit  $M_0 \rightarrow 0$ , and thus the surface density of the sample. Here,  $\sigma=0.347 \mu\text{m}^2$  is the known cesium atom-photon cross-section while the fit parameter  $M_{sat}$  represents the photon number on a CCD pixel at the atomic saturation intensity.

### **Fluctuation of atomic density**

The fluctuations in the absorption images are estimated by taking the average of 11 images under the same experimental procedure, and calculating the mean and variance of optical depth measured at each CCD pixel. Fluctuations are presumed to arise from optical shot noise, thermal atomic fluctuation, and long lengthscale variations arising from total atom number fluctuation. The optical shot noise is calibrated by examining regions with negligible atomic density, and extended to higher optical depth using  $\delta OD_{os} \propto \sqrt{1 + e^{OD}}$ . For the thermal cloud, with density  $n < 0.3$  atoms/site, the fluctuation-dissipation theorem predicts  $\delta N_a = \sqrt{N_a}$ , with  $N_a$  the number of atoms measured in a given region. This result should be valid for a region significantly larger than the correlation length, which we expect for the normal gas to be on order of the deBroglie thermal wavelength, expected to be  $< 1.5 \mu\text{m}$  for our sample. Though each imaging pixel corresponds to an area in the object plane consisting of  $\sim 14$  sites, imperfect imaging resolution is expected

to effectively average away a certain fraction of the total fluctuation. This effect can be calculated, assuming statistical independence for each site, by summing the weight  $w_{i,j}$  of a resolution-limited spot falling within a given pixel  $j$  for each lattice site  $i$ , giving a variance reduced by  $\sum_i w_{i,j}^2$ . The result for our parameters is a reduction to  $\delta n = \gamma\sqrt{n}$ , with  $\gamma \sim 0.11(1)$ . This should be compared with the fraction of the total fluctuation shown in Fig. 3.10 corresponding to thermal fluctuations in the superfluid regime. To make this comparison, we reject global fluctuations associated with variation of the total atom number by subtracting the variance we calculate after first applying a resolution-spoiling gaussian blur to the images from the variance without modification. We find, for the remaining high spatial-frequency fluctuations, a best fit to  $\gamma$  of 0.15(2), using a gaussian blur  $1/e^2$  radius of  $r_b = 14\mu\text{m}$  to remove global variations (the result varies within stated error for blur radii  $7\mu\text{m} < r_b < 28\mu\text{m}$ ). The remaining discrepancy is likely due to calibration of imaging resolution, and possibly the effect of a nonnegligible correlation length.

### 3.2.6 Conclusion

Clearly, *in situ* imaging of the Mott insulator is a powerful new tool to investigate new quantum phases of cold atoms in optical lattices. From the density profiles, not only can one observe the density plateau, incompressibility and reduction of fluctuations in the Mott insulating phase, but also demonstrate a qualitative validation of the fluctuation-dissipation theorem. Relatively modest extension of this work holds new promise for studying the role of quantum fluctuations, correlation and thermodynamics near a quantum phase transition. Since this work, *in situ* imaging has become our primary tool to study 2D atomic quantum gases without or with optical lattices [31, 32, 71].

### 3.3 Slow mass transport and statistical evolution of an atomic gas across the superfluid-Mott insulator transition

We study transport dynamics of ultracold cesium atoms in a two-dimensional optical lattice across the superfluid-Mott insulator transition based on *in situ* imaging. Inducing the phase transition with a lattice ramping routine expected to be locally adiabatic, we observe a global mass redistribution which requires a very long time to equilibrate, more than 100 times longer than the microscopic time scales for on-site interaction and tunneling. When the sample enters the Mott insulator regime, mass transport significantly slows down. By employing fast recombination loss pulses to analyze the occupancy distribution, we observe similarly slow-evolving dynamics, and a lower effective temperature at the center of the sample.

This section is based on our published work (by C.-L. Hung, X. Zhang, N. Gemelke, and C. Chin.) in *Phys. Rev. Lett.* **104**, 160403 (2010). Copyright (2010) by the American Physical Society.

#### 3.3.1 Introduction

The thorough understanding of atomic interactions in optical lattices provides a testing ground to investigate hypothetical models widely discussed in condensed matter and many-body physics [18, 72]. Because of the simplicity and tunability of the underlying Hamiltonian, research on optical lattices generates new fronts to perform precise, quantitative comparison between theoretical calculations and measurements. This new class of “precision many-body physics” has generated tremendous interest in recent years to locate the superfluid (SF) to Mott insulator (MI) phase boundaries [55, 56, 73], described by the Bose-Hubbard model [61, 62], and to characterize Mott and band insulators in Fermi gases [74, 75], described by the Fermi-Hubbard model [76]. Many new, exotic quantum phases

in optical lattices have also been proposed [72], even in the absence of counterparts in condensed matter physics.

As promising as the precise characterization of quantum phases is, fundamental assumptions such as the thermal dynamic equilibrium of the sample should be investigated. Since the preparation of quantum gases generally involves ramping up the lattice potential, dynamics are an inseparable part of all optical lattice experiments. Very slow equilibration processes have been reported in one-dimensional optical lattices [77] and have been suggested by the observation of long-lived repulsively bound pairs [78] and doublons [79] in three-dimensional lattices. Prospects of non-equilibrium dynamics in optical lattices have also attracted much interest recently. Mass and entropy transport in the optical lattices can provide a wealth of information to characterize the underlying quantum phases [80, 81]. Dynamic passage across a phase transition can lead to the proliferation of topological defects in the optical lattices [82].

In the following sections, we study global dynamics of ultracold atomic gases in a monolayer of two-dimensional (2D) optical lattice. After ramping up the lattice potential, we observe both mass transport and statistical distribution of atomic occupancy in the lattice. Mass transport is directly seen from *in situ* density profiles, while occupancy statistics is probed by inducing loss in sites of three or more atoms using a fast three-body recombination loss pulse (see Fig. 3.11). Both processes show intriguing behavior at times much longer than microscopic time scales for atomic interaction and tunneling.

### 3.3.2 *Experimental setup and procedures*

We begin the experiment with a  $^{133}\text{Cs}$  quantum gas in a 2D optical trap. Details on the preparation of the quantum gas and optical lattice loading procedure can be found in Ref. [28] and Ref. [30], respectively. In brief, a nearly pure Bose condensate is loaded

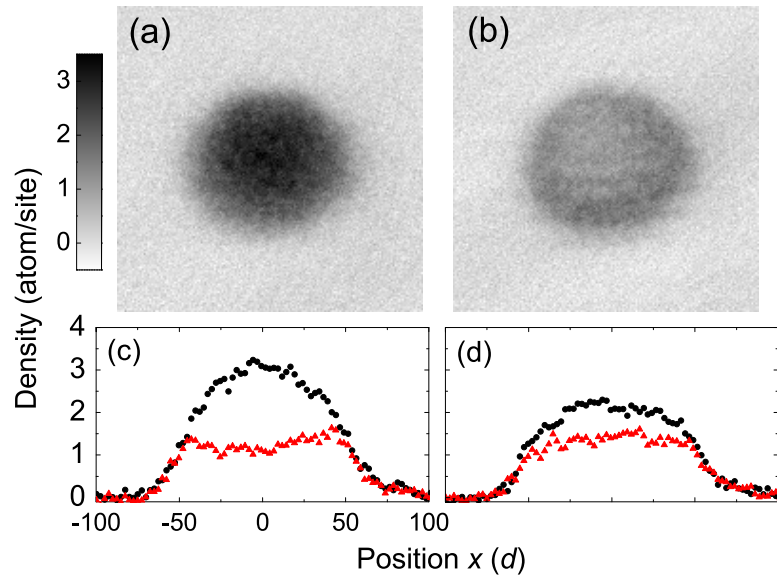


Figure 3.11: Averaged absorption images and density cross sections of  $N = 2 \times 10^4$  cesium atoms in a monolayer of 2D optical lattice. After ramping the lattice in 150 ms to a lattice depth  $V_f = 13 E_R$ , (a) shows the sample immediately after the ramp. In (b), an additional fast recombination pulse removes atoms in sites of occupancy three or more. (c) shows the average density cross sections of (a) (circles) and (b) (triangles). (d) shows the average density cross sections of the samples with additional 800 ms hold time after the ramp, without (circles) and with the recombination loss pulse (triangles). Image size is  $(106 \mu\text{m})^2 = (200 \text{ sites})^2$  and seven images are used in each averaged result.

into a 2D optical dipole trap, formed by two orthogonally crossed beams on the  $x - y$  plane and a one-dimensional vertical optical lattice of  $4 \mu\text{m}$  spacing which confines the whole sample in a single “pancake”-like lattice site [30]. Using microwave tomography, we find  $\sim 95\%$  of the atoms are loaded into a single pancake trap. The remaining  $\sim 5\%$  in the neighboring sites do not contribute to the main results reported in this letter. The trap vibration frequencies are  $(\omega_x, \omega_y, \omega_z) = 2\pi \times (11, 13, 1970)$  Hz, and the cloud temperature is  $T = 11$  nK. The ratios  $\hbar\omega_i/k_B T = (0.05, 0.06, 9)$  indicate the sample is two-dimensional. After 2D trap loading, we adjust the atomic scattering length  $a$  by ramping the magnetic field to a designated value, typically,  $B = 20.7$  G where  $a = 200 a_B$  and  $a_B$  is the Bohr radius. At this field, the three-body recombination loss rate is at the Efimov minimum [48].

We introduce a 2D optical lattice by slowly turning on retro-reflections of the crossed dipole beams which add a square lattice potential with lattice spacing  $d = 532$  nm and a weak contribution to the envelope confinement characterized by a mean radial frequency  $\sqrt{\omega_x\omega_y} = 2\pi(1 + V/82E_R) \times 12$  Hz, where  $E_R = k_B \times 64$  nK is the recoil energy and  $V$  is the lattice depth. Care is taken to equalize lattice depths in the  $x$  and  $y$  directions by balancing the lattice vibration frequencies to within 5%. Based on the vibration frequency measurements, we calculate tunneling  $t$  and on-site interaction  $U$  numerically from the band structure in a homogeneous 2D lattice.

We ramp on the lattice depth following  $V(\tau) = V_f(1 + \gamma)/[1 + \gamma e^{4(\tau - \tau_c)^2/\tau_c^2}]$  [83], preceded by a 30 ms linear ramp from 0 to  $0.4 E_R$  to ensure a smooth turning on of the lattice potential at low depth. The final depth  $V_f$  is reached at time  $\tau = \tau_c$  and  $\gamma$  is chosen such that  $V(0) = 0.4 E_R$ . After the ramp, the sample is held in the lattice for a hold time  $\tau_{hold}$ . The adiabaticity parameter of the ramp is given by

$$\alpha = \hbar|\dot{t}|/t^2; \quad (3.11)$$

slow ramps with  $\alpha < 1$  suggest that local equilibrium of the system is preserved [84, 83].

We obtain the *in situ* density profile of the sample by absorption imaging normal to the  $x - y$  plane. After a hold time  $\tau_{hold}$ , we first switch the magnetic field to  $B = 17.7$  G ( $a = 40a_B$ ) and then turn off the 2D lattice 100  $\mu$ s before the imaging, reducing the on-site peak density by a factor of 30, in order to mitigate any density dependent loss during the imaging process.<sup>2</sup> The atomic density is measured with a spatial resolution of 1.3  $\mu$ m using a long working distance (34 mm) commercial microscope objective. The strength and duration of the imaging pulse are chosen to keep the travel distance of the atoms due to the radiation pressure from the imaging beam small compared to the depth of focus, while maintaining a good signal-to-noise ratio.

### 3.3.3 *Slow mass transport*

Our first step to study the global dynamics is to watch how the density profile equilibrates after a lattice ramp. Here we employ a ramp which is locally adiabatic, but is fast enough to induce detectable mass flow. An example is shown in Fig. 3.12 (a), where after a  $\tau_c = 20$  ms ramp to  $V_f = 10 E_R$  ( $U/t = 11$ ,  $\alpha < 0.6$ ) the sample of  $N = 2 \times 10^4$  atoms at scattering length  $a = 200 a_B$  gently expands and the peak density slowly decreases. This deformation is consistent with the increase of repulsive atomic interaction in stronger lattice confinement.

To quantify the rate of mass redistribution, we define the root-mean-square deviation of a density profile at hold time  $\tau$  from equilibrium as

$$\Delta(\tau) = \left\{ \sum_i [\bar{n}_i(\tau) - \bar{n}_{eq,i}]^2 \right\}^{1/2}, \quad (3.12)$$

---

<sup>2</sup> This procedure suppresses systematic distortions of the density measurement. In previous works [30], our imaging was performed at low magnetic fields, where recombination and radiative losses preferentially reduce the density at the center and can enhance the plateau feature in deep lattices.

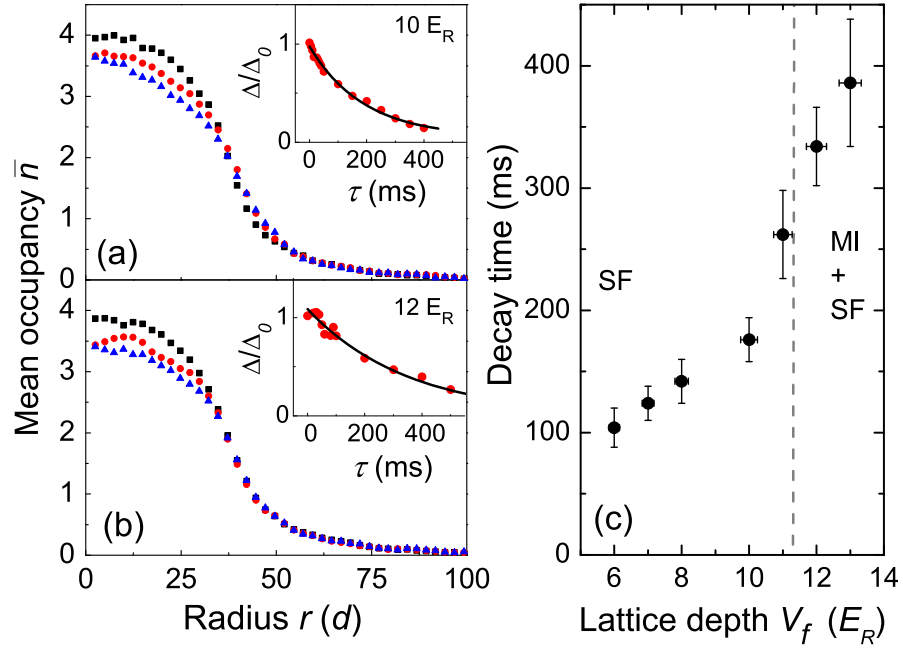


Figure 3.12: Evolution of the density profile after a short lattice ramp. Following a  $\tau_c = 20$  ms ramp to  $V_f = 10 E_R$  ( $U/t = 11$ ,  $\alpha < 0.6$ ), (a) shows the radial density profiles measured after hold times of 0 ms (squares), 200 ms (circles) and 500 ms (triangles). Inset shows the time evolution of  $\Delta$ , normalized to the initial value  $\Delta_0 = \Delta(0)$  (circles) and the single exponential fit. (b) shows the profiles measured at  $V_f = 12 E_R$  ( $U/t = 20$ ,  $\alpha < 1$ ). The fitted decay times at different depths of  $V_f$  are shown in (c), where the dashed line marks the critical lattice depth, see text.

where the sum goes over lattice sites enclosing the sample.  $\bar{n}_i(\tau)$  is the mean occupancy of site  $i$  at hold time  $\tau$ , obtained by averaging over an annular area centered on the cloud, containing site  $i$ , and with width  $1.3 \mu\text{m}$  [30].  $\bar{n}_{eq,i}$  is the mean occupancy of site  $i$  at equilibrium, which we obtain from samples that cease to evolve after long hold time of  $\tau_{hold} = 500 \sim 800$  ms.

At lattice depths  $V_f < 10 E_R$ , the sample shows a weak breathing mode oscillation in the first 50 ms of hold time. After 50 ms,  $\Delta(\tau)$  can be fit by single exponential decays with time constants  $> 100$  ms. When the lattice depth reaches  $11 E_R$  or higher, the mass flow slows down significantly, see Fig. 3.12 (b) and (c), suggesting that the mass transport is suppressed in this regime. The crossover behavior near  $V_f = 11 E_R$ , where  $U/t \approx 15$ , is consistent with a recent observation of the suppression of superfluidity at  $U/t = 16$  in a 2D optical lattice [56], and quantum Monte Carlo calculations, predicting that the SF-MI transition at the tip of the  $n = 1$  Mott lobe occurs at  $U/t \approx 16.74$  in 2D [85]. For  $V_f > 13 E_R$ , even slower dynamics require much longer hold time and the slow loss from three-body recombination limits our ability to determine the mass redistribution time scale.<sup>3</sup>

The slow dynamics throughout the SF-MI regime indicate that the global thermalization is much slower than the microscopic time scales. Indeed, in the range of  $V_f = 6 \sim 13 E_R$ , tunneling to neighboring sites occurs in  $\tau_t = \hbar/zt = 0.6 \sim 3$  ms, where  $z = 4$  is the coordination number of the 2D square lattice.

### 3.3.4 Evolution of occupancy statistics

In the second experiment, we investigate the evolution of occupancy statistics. For this, we develop a scheme to determine the fraction of sites with three or more atoms by inducing

---

3. At  $V_f = 13 E_R$  and scattering length  $a = 200 a_0$ , three body loss rate for 3 atoms per site is  $\sim 0.4 \text{ s}^{-1}$

a fast three-body recombination loss, and comparing the density profiles with and without the loss. For cesium atoms, extremely fast three-body loss can be induced by jumping the magnetic field near an Efimov resonance [48], where the loss happens much faster than atoms tunnel.

We induce the recombination loss at  $V_f = 13 E_R$  by jumping the magnetic field to  $B = 2$  G for a duration of 1 ms before imaging at 17.7 G. The  $1/e$  time of the field switching is below 100  $\mu$ s. During the switching, the magnetic field from the eddy currents is measured by microwave spectroscopy and compensated by a controlled overshoot of currents in the magnetic coils. At 2 G, the three-body loss rate is as high as  $(20 \mu\text{s})^{-1}$  for 3 atoms in one site, much faster than the tunneling rate  $1/\tau_t = (3 \text{ ms})^{-1}$ , and the 1 ms pulse is sufficient to remove all the atoms that could participate in the loss process.

We analyze the dynamics of on-site statistics by first ramping the lattice in  $\tau_c = 300$  ms to  $V_f = 13 E_R$  ( $U/t = 41$ ,  $\alpha < 0.1$ ) at scattering length  $a = 310 a_B$  and then holding the sample for up to 800 ms. Here, the lattice ramp is slow enough to ensure negligible subsequent mass flow. Density profiles at different hold times, with and without the loss pulse, are shown in Fig. 3.13 (a-c). A larger fractional loss occurs at the central part of the sample where the density is higher, as expected; there is no apparent loss in the wing. We observe a smaller fractional loss after a longer hold time, which suggests that fewer sites are found with three or more atoms.

The evolution of the statistics is best shown in Fig. 3.13 (d), where the atom loss,  $\Delta\bar{n}$ , is induced by the recombination pulse after different hold times. A dramatic difference is seen near the center with mean occupancy near  $\bar{n} = 2$ . Here the loss fraction reaches  $\Delta\bar{n}/\bar{n} = 50\%$  immediately after the ramp, and it slowly declines to merely 15% after a hold time of  $\tau_{hold} = 800$  ms.

To quantitatively model the loss, we assume, starting with  $n$  atoms in one site, ( $n$  modulo 3) atoms remain after the pulse. To test this model, we prepare an ideal 2D gas by

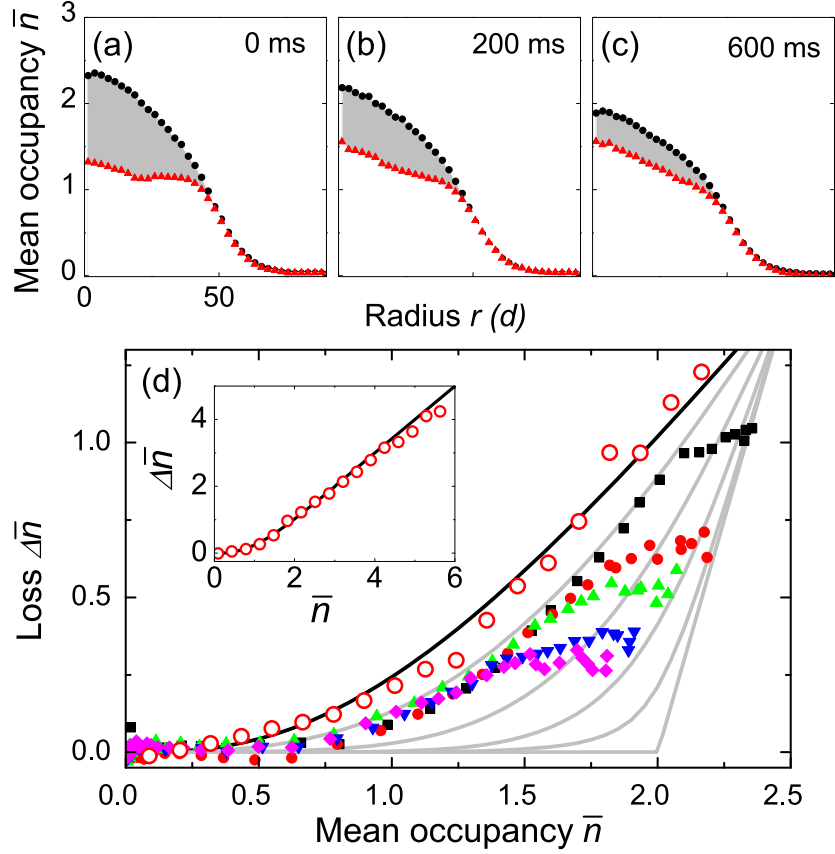


Figure 3.13: Evolution of the on-site statistics in a Mott insulator. ( $N = 1.6 \times 10^4$ ,  $\tau_c = 300$  ms,  $V_f = 13 E_R$ ). Upper figures show the density profiles of the samples held in the final depth  $V_f = 13 E_R$  for  $\tau_{hold} =$  (a) 0 ms, (b) 200 ms, (c) 600 ms and then imaged with (triangles) and without (circles) the recombination pulse. Shaded areas mark the loss fractions. (d) shows the loss  $\Delta\bar{n}$  versus mean occupancy  $\bar{n}$  measured after different hold times (filled symbols): 0 ms (squares), 200 ms (circles), 400 ms (upward triangles), 600 ms (downward triangles) and 800 ms (diamonds). Gray lines are the loss derived from an insulator model, see text, assuming  $k_B T/U=1$  (higher curve), 0.5, 0.3, 0.2 and 0 (lower curve). The black line, derived from the Poisson distribution, is in good agreement with an ideal gas measurement (open circles). The inset shows an extended view.

tuning the magnetic field to  $B = 17.1$  G, where  $a \approx 0 a_B$ . We then quickly ramp on the lattice to  $30 E_R$  in 10 ms to freeze the on-site occupancy and perform the loss measurement. For non-interacting particles, we expect the occupancy obeys a Poisson distribution. The calculated atom loss, see black solid lines in Fig. 3.13 (d) and the inset, is in good agreement with our measurement.

Recombination losses measured with interacting samples and slow lattice ramps, on the other hand, deviate from the Poisson model toward lower values for all mean occupancies (see Fig. 3.13 (d)). This is a general characteristic of the strongly interacting gas.

To gain further insight into the occupancy statistics in an insulator, we compare our measurement with an analytic model based on a grand canonical ensemble [86, 68]. In deep lattices with  $t \ll U, k_B T$ , the probability for occupancy  $n$  can be written as  $P_n = Q^{-1} e^{-\beta(H_n - \mu n)}$ , where  $H_n \approx (U/2)n(n-1)$ ,  $\beta = 1/k_B T$ ,  $\mu$  is the local chemical potential and  $Q = \sum_n e^{-\beta(H_n - \mu n)}$  is the grand partition function. The mean occupancy is then  $\bar{n} = \sum n P_n$  and the loss is modeled as

$$\Delta \bar{n} = \bar{n} - \sum P_n (n \bmod 3). \quad (3.13)$$

Calculations for  $k_B T/U = 1, 0.5, 0.3, 0.2$  and  $0$  are plotted in Fig. 3.13(d). For  $\bar{n} < 2.5$ , all curves show smaller loss than does the Poisson model. An insulator at lower temperature experiences fewer losses because thermal fluctuation is reduced. At zero temperature, loss only occurs at  $\bar{n} > 2$ , where the occupancy  $n \geq 3$  is unavoidable.

Surprisingly, our loss measurements do not follow the model with a uniform temperature for up to 800 ms hold time. Using  $U = k_B \times 26$  nK and describing the deviation from a constant temperature contour by an effective local temperature  $T_{\text{eff}}(r)$ , we find the center of the cloud has a lower  $T_{\text{eff}} \sim 6$  nK, while for the wing  $T_{\text{eff}} \sim 20$  nK even after 800 ms of hold time. This persistent temperature variation across the sample suggests that the heat

flow is insufficient to establish a global thermal equilibrium even after 800 ms hold time. This may be aggravated by a large heat capacity of the atoms in the wing.

Both the slow mass and heat flows observed in this work raise the issue of describing quantum gases in optical lattices using a thermodynamic model. We suspect that the slow dynamics is partially due to our large sample size of  $(100 \text{ sites})^2$  and the dimensionality of our system, and partially associated with the critical behavior of the system. Across the SF-MI transition, the sample enters the quantum critical regime, where long equilibration times are expected [82, 87]. Other interesting mechanisms include the long lifetime of the excited doublon [79], which could slow down statistical redistribution of occupancies while supporting mass transport. Moreover, the slow recombination loss preferentially removes atoms at the center of the sample, creating  $\sim 20\%$  observed reduction in the mean occupancy during 800 ms of hold time, which could lead to a radial temperature gradient assuming sufficient local rethermalization.

### 3.3.5 Conclusion

In summary, we show that the *in situ* density profiles of atoms in a 2D optical lattice provide a viable tool for investigating dynamic processes induced by chemical potential and temperature imbalance. In both cases, we find equilibration times much longer than the microscopic tunneling time scale. Further investigation into these processes and the relevance of our observation to the quantum dynamics in the critical regime will be reported in the future.

### 3.4 Observation of scale invariance and universality in two-dimensional Bose gases

The collective behavior of a many-body system near a continuous phase transition is insensitive to the details of its microscopic physics[3]. Characteristic features near the phase transition are that the thermodynamic observables follow generalized scaling laws[3]. The Berezinskii-Kosterlitz-Thouless (BKT) phase transition[88, 89] in two-dimensional (2D) Bose gases presents a particularly interesting case because the marginal dimensionality and intrinsic scaling symmetry[90] result in a broad fluctuation regime which manifests itself in an extended range of universal scaling behavior. Studies on BKT transition in cold atoms have stimulated great interest in recent years[91, 92, 93, 94, 95, 96], clear demonstration of a critical behavior near the phase transition, however, has remained an elusive goal. Here we report the observation of a scale-invariant, universal behavior of 2D gases through in-situ density and density fluctuation measurements at different temperatures and interaction strengths. The extracted thermodynamic functions confirm a wide universal region near the BKT phase transition, provide a sensitive test to the universality prediction by classical-field theory [97, 98] and quantum Monte Carlo (MC) calculations[99], and point toward growing density-density correlations in the fluctuation region. Our assay raises new perspectives to explore further universal phenomena in the realm of classical and quantum critical physics.

This section is based on our published work (by C.-L. Hung, X. Zhang, N. Gemelke, and C. Chin) in *Nature* **470**, 239 (2011).

#### 3.4.1 Introduction

In 2D Bose gases, critical behavior develops in the BKT transition regime, where an ordered phase with finite-ranged coherence competes with thermal fluctuations and in-

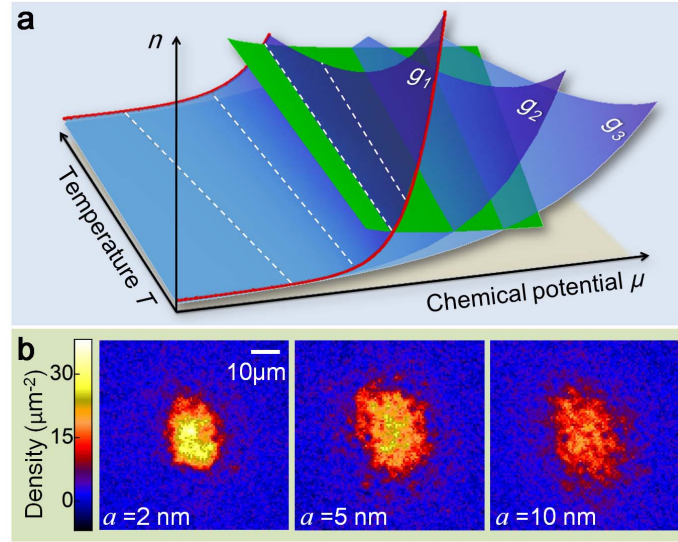


Figure 3.14: Illustration of scale invariance and universality in 2D quantum gases. (a) Scale invariance links any thermodynamic observable at different  $\mu$  and  $T$  via a simple power-law scaling. In a 2D Bose gas with coupling constant  $g \ll 1$ , atomic density  $n$  measured at different temperatures (red lines) can be scaled through constant  $\mu/T$  and  $n/T$  contours (dashed lines). Near the BKT phase transition boundary (green plane), systems with different  $g = g_1, g_2, \dots$  (blue planes) scale universally. (b) *In situ* density measurements of trapped 2D gases provide crucial information to test the hypotheses of scale invariance and universality. Sample images at different scattering lengths  $a$  are obtained from single shot.

duces a continuous phase transition from normal gas to superfluid with quasi-long range order[89]. In this fluctuation region, a universal and scale-invariant description for the system is expected through the power-law scaling of thermodynamic quantities with respect to the coupling strength and a characteristic length scale[98, 100], e.g., thermal de Broglie wavelength (Fig. 3.14a). For weakly interacting gases at finite temperatures, in particular, the scale invariance prevails over the normal, fluctuation, and superfluid regions because of the density-independent coupling constant[67] and the symmetry of underlying Hamiltonian[90].

In this section, we experimentally verify the scale invariance and universality of interacting 2D Bose gases, and identify BKT critical points. We test scale invariance of *in situ*

density and density fluctuations of  $^{133}\text{Cs}$  2D gases at various temperatures. We study the universality near the BKT transition by tuning the atomic scattering length using a magnetic Feshbach resonance[19] and observing a universal scaling behavior of the equation of state and the quasi-condensate density. Finally, by comparing the local density fluctuations and the compressibility derived from the density profiles, we provide strong evidence of a growing density-density correlation in the fluctuation regime.

### 3.4.2 *Experimental setup and procedures*

We begin the experiment by loading a nearly pure  $^{133}\text{Cs}$  Bose condensate of  $N = 2 \times 10^4$  atoms into a single pancake-like optical potential with strong confinement in the vertical ( $z$ -) direction and weak radial confinement in the horizontal ( $r$ -) direction[30, 31]. The trapping potential,  $V(r, z) = m\omega_r^2 r^2/2 + m\omega_z^2 z^2/2$ , has mean harmonic trapping frequencies  $\omega_r = 2\pi \times 10$  Hz and  $\omega_z = 2\pi \times 1900$  Hz. Here,  $r$  denotes the radial distance to the trap center and  $m$  is the cesium atomic mass. In this trap, we reach temperatures as low as  $T = 15$  nK and moderate peak chemical potential  $\mu_0 < k_B T$ . The ratio  $\hbar\omega_z/\mu_0 > \hbar\omega_z/k_B T \sim 6$  indicates that the sample is deeply in the 2D regime with  $< 1\%$  population in the vertical excited states. Here,  $\hbar = h/2\pi$ ,  $h$  is the Planck constant, and  $k_B$  is the Boltzmann constant. The 2D coupling constant is evaluated according to  $g = \sqrt{8\pi}a/l_z$  [67], where  $a$  is the atomic scattering length and  $l_z = 200$  nm is the vertical harmonic oscillator length. We control the scattering length  $a$  in the range of  $2 \sim 10$  nm  $\ll l_z$ , resulting in weak coupling strengths  $g = 0.05 \sim 0.26$ . Here, the density-dependent correction to  $g$ [67, 101] is expected to be small and negligible ( $< 2\%$ ).

We obtain *in situ* density distributions of 2D gases by performing absorption imaging perpendicular to the horizontal plane with a commercial microscope objective and a CCD camera[31] (see Fig. 3.14b for sample images). About 50 images are collected for each

experiment condition, and the average density  $n$  and the density variance  $\delta n^2$  are evaluated pixel-wise (see Section 3.4.6). We obtain the radial density  $n(r)$  and variance  $\delta n^2(r)$  profiles (Fig. 3.15 insets) by accounting for the cloud anisotropy and performing azimuthal averaging[30].

We obtain the equation of state  $n(\mu, T)$  from the averaged density profile by assigning a local chemical potential  $\mu(r) = \mu_0 - V(r, 0)$  to each point according to local density approximation. Both  $T$  and  $\mu_0$  can be determined from the low density wing where the sample is assumed normal and the density profile can be fit to a mean-field formula  $n(\mu, T) = -\lambda_{dB}^{-2} \ln[1 - \exp(\mu/k_B T - gn\lambda_{dB}^2/\pi)]$ [95], where  $\lambda_{dB} = h/\sqrt{2\pi m k_B T}$  is the thermal de Broglie wavelength.

### 3.4.3 Scale invariance in 2D Bose gases

We confirm the scale invariance of a 2D gas by first introducing the dimensionless, scaled form of density  $\tilde{n} = n\lambda_{dB}^2$  (phase space density), fluctuation  $\delta\tilde{n}^2 = \delta n^2 \lambda_{dB}^4$ , and chemical potential  $\tilde{\mu} = \mu/k_B T$ , and showing that the equation of state and the fluctuation satisfy the following forms:

$$\tilde{n} = F(\tilde{\mu}) \quad (3.14)$$

$$\delta\tilde{n}^2 = G(\tilde{\mu}), \quad (3.15)$$

where  $F$  and  $G$  are generic functions. This suggests both energy and length scales are set solely by the thermal energy and the de Broglie wavelength, respectively. An example at  $g = 0.26$  ( $a = 10$  nm) is shown in Fig. 3.15. Here we show that while the original density and fluctuation profiles are temperature dependent (see Fig. 3.15 insets), all profiles collapse to a single curve in the scaled units. At negative chemical potential  $\tilde{\mu} < 0$ , the system is normal and can be described by a mean-field model (dashed lines). In the

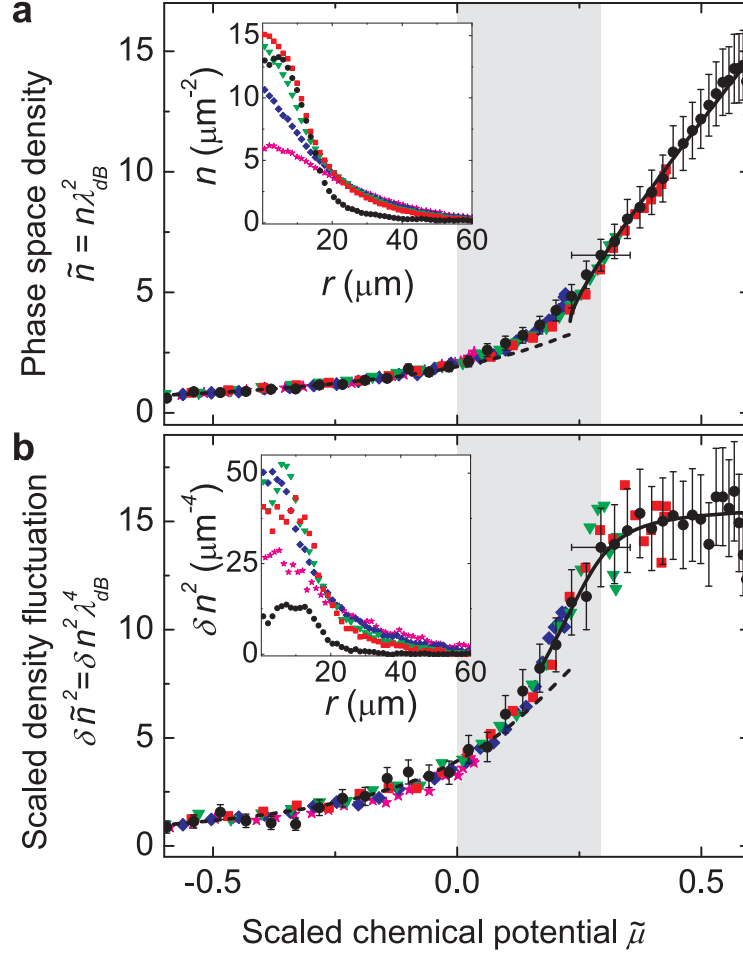


Figure 3.15: Scale invariance of density and its fluctuation. (a) Scaled density (phase space density)  $\tilde{n} = n\lambda_{dB}^2$  as a function of the scaled chemical potential  $\tilde{\mu} = \mu/k_B T$  measured at five different temperatures:  $T = 21$  nK (black circles), 37 nK (red squares), 42 nK (green triangles), 49 nK (blue diamonds), and 60 nK (magenta stars), and coupling strength  $g = 0.26$ . Mean-field expectations for normal gas (dashed line) and superfluid (solid line) are shown for comparison. Inset shows the radial density profiles before scaling. (b) Scaled fluctuation  $\delta\tilde{n}^2 = \delta n^2 \lambda_{dB}^4$  at different temperatures. Dashed line is the mean-field calculation based on the fluctuation-dissipation theorem<sup>20</sup>. Solid line is an empirical fit to the crossover feature from which the critical chemical potential  $\tilde{\mu}_c$  is determined. Inset shows the radial fluctuation profiles before scaling. The shaded area marks the fluctuation region  $0 < \tilde{\mu} < \tilde{\mu}_c$ . Error bars show standard deviation of the measurement.

range of  $0 < \tilde{\mu} < 0.3$ , the system enters the fluctuation regime and deviation from the mean-field calculation becomes evident. Crossing from normal gas to this regime, however, we do not observe sharp transition feature in the equation of state. At even higher  $\tilde{\mu} > 0.3$ , the system becomes a superfluid and the density closely follows a mean-field prediction[98]  $\tilde{n} = 2\pi\tilde{\mu}/g + \ln(2\tilde{n}g/\pi - 2\tilde{\mu})$ . We notice that the mean-field theory in the superfluid limit also cannot accurately describe the system in the fluctuation regime. Transition into the BKT superfluid phase is most easily seen in the scaled fluctuation  $\delta\tilde{n}^2$ , which crosses over to a nearly constant value due to the suppression of fluctuation in the superfluid regime[102]. In the density profile  $\tilde{n}$ , a corresponding transition feature can be found when one computes the derivative  $\partial\tilde{n}/\partial\tilde{\mu}$ , i.e., the scaled compressibility  $\tilde{\kappa}$ , as suggested by the fluctuation-dissipation theorem discussed in later paragraphs and Fig. 3.17. Finally, our measurement suggests that the validity of scale invariance extends to all thermal, fluctuation and superfluid regimes, a special feature for weakly-interacting 2D gases[90] which guided the analysis of a recent experiment[33].

**Determination of the BKT critical points** We associate the crossover feature in the density fluctuations  $\delta\tilde{n}^2$  and the scaled compressibility  $\tilde{\kappa}$  with the BKT transition[102, 103]. To estimate the location of the transition point, we apply an empirical fit to this feature and determine the critical chemical potential  $\tilde{\mu}_c$  and the critical phase space density  $\tilde{n}_c$  (see Section 3.4.6). Results at different  $g$  in the range of 0.05 to 0.26 are shown in Fig. 3.16c-d and compared to the theoretical prediction of  $\tilde{n}_c = \ln(\xi/g)$  and  $\tilde{\mu}_c = (g/\pi) \ln(\xi_\mu/g)$ [104], where  $\xi = 380$  and  $\xi_\mu = 13.2$  are determined from a classical-field MC calculation[97]. Our results show good agreement with the theory, apart from a potential systematic error from the choice of the fit function, which can account for a down shift of 10% in the fit values of  $\tilde{\mu}_c$  and  $\tilde{n}_c$ .

### 3.4.4 Universality in 2D Bose gases

Further comparison between profiles at different interaction strengths allows us to test the universality of 2D Bose gases. Sufficiently close to the BKT critical point with  $|\tilde{\mu} - \tilde{\mu}_c| < g$ , one expects the phase space density shows a universal behavior[98],

$$\tilde{n} - \tilde{n}_c = H\left(\frac{\tilde{\mu} - \tilde{\mu}_c}{g}\right), \quad (3.16)$$

where  $H$  is a generic function. Here, density and chemical potential are offset from the critical values  $\tilde{n}_c$  and  $\tilde{\mu}_c$ , which remove the non-universal dependence on the microscopic details of the interaction[100, 98].

To test the universality hypothesis, we rescale  $\tilde{\mu}$  to  $\tilde{\mu}/g$  and look for critical values  $\tilde{n}_c$  and  $\tilde{\mu}_c$  such that the equations of state at all values of  $g$  display a universal curve in the phase transition regime (see Section 3.4.6). Indeed, we find that all rescaled profiles can collapse to a single curve in the fluctuation region  $-1 < (\tilde{\mu} - \tilde{\mu}_c)/g < 0$  and remain overlapped in an extended range of  $|\tilde{\mu} - \tilde{\mu}_c|/g \leq 2$  (see Fig. 3.16a), which contrasts the very different equations of state  $\tilde{n}(\tilde{\mu})$  at various  $g$  shown in the inset of Fig. 3.16a. Our result closely follows the classical-field prediction[98] and quantum MC calculations[99] assuming strictly 2D mean-field contribution, and the fitting parameters: critical density  $\tilde{n}_c$  and chemical potential  $\tilde{\mu}_c$  show proper dependence on  $g$  and are in fair agreement with the theory prediction[97] (see Fig. 3.16c-d). We emphasize that critical values determined from the density fluctuations (see Fig. 3.16c-d) match well with those determined from the universal behavior, indicating that universality is a powerful tool to determine the critical point from a continuous and smooth density profile. Similar agreement with the theory on the critical densities has also been reported based on different experiment techniques[92, 94, 96].

Further universal features near the phase transition can be revealed in the growth of the

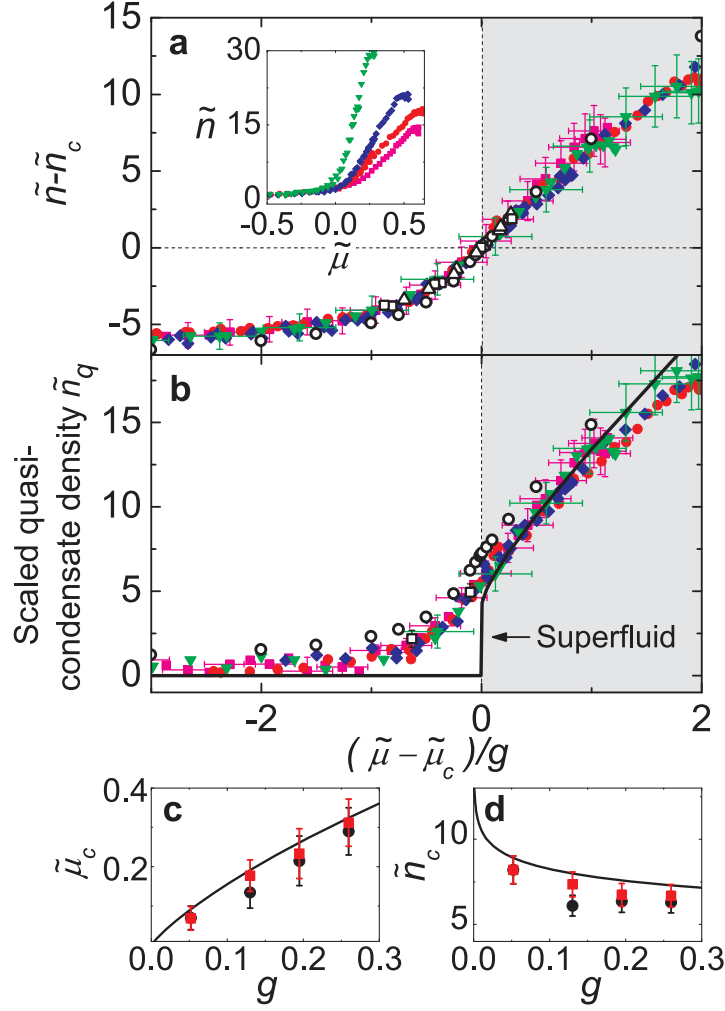


Figure 3.16: Universal behavior near the BKT critical point. (a) Rescaled density profiles  $\tilde{n} - \tilde{n}_c$  measured at various coupling strengths,  $g = 0.05$  (green triangles), 0.13 (blue diamonds), 0.19 (red circles), and 0.26 (magenta squares). Inset shows the original equations of state  $\tilde{n}(\tilde{\mu})$ . (b) scaled quasi-condensate density  $\tilde{n}_q = \sqrt{\tilde{n}^2 - \delta\tilde{n}^2}$  at different interaction strengths. In both plots, MC calculations from Ref. [98] (open circles) and Ref. [99] ((a) open squares for  $g = 0.07$  and open triangles for  $g = 0.14$ ; (b) open squares) are plotted for comparison. The shaded area marks the superfluid regime and the solid line in (b) shows the superfluid phase space density calculation<sup>12</sup>. (c-d) critical values  $\tilde{\mu}_c$  and  $\tilde{n}_c$  determined from the following methods: universal scaling as shown in (a) (see Section 3.4.6, red squares), density fluctuation crossover (see text, black circles), and MC calculation from Ref. [97] (solid line). Experiment values coincide at  $g = 0.05$  identically, as a result of our analysis (see Section 3.4.6). Error bars show the standard deviation of the measurement.

quasi-condensate (QC) density  $n_q = \sqrt{n^2 - \delta n^2}$  across the phase transition[97, 98, 105]. QC is a measure of the non-thermal population in a degenerate Bose gas. A finite QC density does not necessarily imply superfluidity, but can be responsible for a non-Gaussian distribution observed in the momentum space[94]. QC is predicted to be universal near the critical point following[98]

$$\tilde{n}_q = Q\left(\frac{\tilde{\mu} - \tilde{\mu}_c}{g}\right), \quad (3.17)$$

where  $Q$  is a generic function and  $\tilde{n}_q = n_q \lambda_{dB}^2$ .

We employ both of our density and fluctuation measurements to evaluate  $\tilde{n}_q$  at various  $g$ . Adopting  $\tilde{\mu}_c$  determined from the universal behavior of the density profile, we immediately find that all measurements collapse to a single curve in the range of  $|\tilde{\mu} - \tilde{\mu}_c|/g \leq 2$  with apparent growth of QC density entering the fluctuation region (Fig. 3.16b). The generic function  $Q$  we determined is in good agreement with the classical-field[98] and quantum MC[99] calculations with no fitting parameters. Both our density and fluctuation measurements show universal behaviors throughout the fluctuation region where a mean-field description fails and confirm universality in a 2D Bose gas near the BKT phase transition[98, 99].

### 3.4.5 *Evidence of growing density-density correlations in the critical fluctuation region*

The generic functions we described in the previous paragraphs offer new avenues to investigate the critical behavior of the 2D gas. Following the framework of scale invariance, we compare the dimensionless compressibility  $\tilde{\kappa} = \partial\tilde{n}/\partial\tilde{\mu} = F'(\tilde{\mu})$  and the fluctuation  $\delta\tilde{n}^2 = G(\tilde{\mu})$  extracted from the measurements at  $g = 0.05$  and  $0.26$  (see Fig. 3.17). In the normal gas regime at low phase space density ( $G(\tilde{\mu}), F'(\tilde{\mu}) < 3$ ), a simple equality

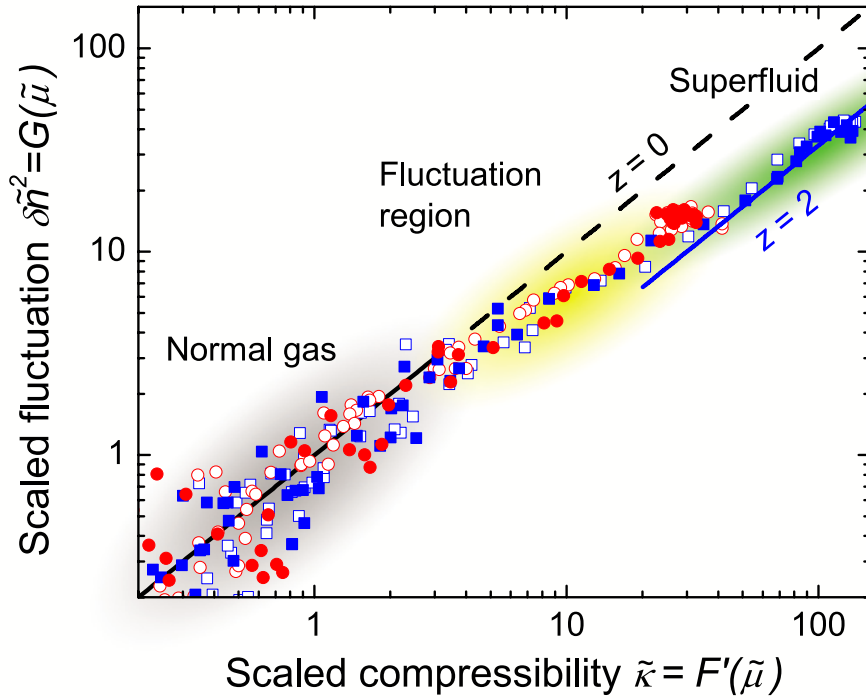


Figure 3.17: Fluctuation versus compressibility. Scaled compressibility  $\tilde{\kappa} = F'(\tilde{\mu})$  and scaled density fluctuation  $\delta\tilde{n}^2 = G(\tilde{\mu})$  are derived from measurements at two interaction strengths,  $g = 0.05$  (squares) and  $g = 0.26$  (circles), each containing two different temperatures between 20 and 40 nK (solid and open symbols, respectively). Diagonal line shows the expectation of  $G = F'$  in the normal gas region. Solid line shows suppressed fluctuation  $G = F'/(1+z)$  with  $z = 2$ .

$G = F'$  is observed. This result is consistent with the fluctuation-dissipation theorem (FDT) for a classical grand canonical ensemble[106], which gives  $k_B T \frac{\partial N}{\partial \mu} = \delta N^2$ , where  $N$  is the particle number in a detection cell. In the fluctuation and the superfluid regimes at higher phase space density, our measurement shows that density fluctuations drop below the compressibility  $G < F'$ .

Natural explanations for the observed deviation include non-vanishing dynamic density susceptibility at low temperature[107] and the emergence of correlations in the fluctuation region[108]. While the former scenario is outside the scope of this article, we show that the

correlation alone can explain our observation. Including correlation, the compressibility conforms to [109, 108]

$$\tilde{\kappa}(\mathbf{r}) = \lambda_{dB}^{-2} \int \langle \delta\tilde{n}(\mathbf{r})\delta\tilde{n}(\mathbf{r} + \mathbf{r}') \rangle d^2r' \quad (3.18)$$

$$= \delta\tilde{n}^2(\mathbf{r})(1 + z), \quad (3.19)$$

where  $\langle \dots \rangle$  denotes ensemble average and  $z = \frac{1+n(\mathbf{r}) \int [g^{(2)}(\mathbf{r}, \mathbf{r} + \mathbf{r}') - 1] d^2r'}{1+n(\mathbf{r}) \int_v [g^{(2)}(\mathbf{r}, \mathbf{r} + \mathbf{r}') - 1] d^2r'} - 1$  is the relative strength of correlation to local fluctuation  $\delta\tilde{n}^2$  [108]. Here  $g^{(2)}$  is the normalized second-order correlation function [110] and  $v$  denotes the effective area of the resolution limited spot. When the sample is uncorrelated, we have  $z = 0$ ; non-zero  $z$  suggests finite correlations in the sample. In the fluctuation region shown in Fig. 3.17, observing a lower fluctuation than would be indicated by the compressibility, with  $z$  approaching 2, suggests that the correlation length approaches or even exceeds our imaging cell dimension  $\sqrt{v} \sim 2 \mu\text{m}$ . This observation is in agreement with the expected growth of correlation when the system enters the fluctuation region. Similar length scales were also observed in the first-order coherence near the BKT phase transition using an interferometric method [94] and near the superfluid phase transition in three dimensions [111].

### 3.4.6 Detailed procedures and analyses

Preparation and detection of cesium 2D Bose gases are similar to those described in Ref. [31]. We adjust the temperature of the sample by applying magnetic field pulses near a Feshbach resonance to excite the atoms. We then tune the scattering length to a designated value, followed by 800 ms wait time to ensure full thermalization of the sample.

Absorption imaging is performed *in situ* using a strong resonant laser beam, saturating the sample to reduce the optical thickness. Atom-photon resonant cross-section and atomic

density are independently calibrated. Averaged atom number  $N_i$  and number fluctuation  $\delta N_i^2$  at  $i$ -th CCD pixel are evaluated pixel-wise based on images taken under identical experiment conditions. The photon shot-noise, weakly depending on the sample's optical thickness, is calibrated and removed from the measured number variance. We correct the effect of finite imaging resolution on the remaining number variance using calibration from dilute thermal gas measurements. The density fluctuation  $\delta n_i^2$  is obtained from the recovered atom number variance using  $\delta n_i^2 \lambda_{dB}^2 = \delta N_i^2 / A$ , which replaces the dependence on the CCD pixel area  $A$  by a proper area scale  $\lambda_{dB}^2$ .

**Calibration of the atomic surface density and the atom number fluctuation.** The atomic surface density  $n$  of the 2D gas is evaluated with similar schemes discussed in Ref. [112], where the resonant cross-section  $\sigma_0$  is independently calibrated using a thin 3D Bose condensate with similar optical thickness and the known atom number-to-Thomas-Fermi radius conversion. The resulting value can be compared to that determined from the atom shot-noise amplitude in dilute 2D thermal gases, where the noise is evaluated using binned CCD pixels to remove finite resolution effects. For dilute thermal gases, we expect  $\delta N^2 = N$ , where  $N$  is the mean atom number; we compare the fluctuation amplitude to the mean and extract the value of  $\sigma_0$ . Two results agree to within 10% and the residual non-linearity in the density calibration is negligible.

We evaluate the atom number variance  $\delta N^2$  pixel-wise based on images taken under identical experiment conditions. The photon shot-noise contribution  $\delta N_p^2$ , which weakly depends on the sample's optical thickness  $n\sigma_0$ , is calibrated and removed from the atom number fluctuation using  $\delta N_p^2 = (\delta N_0^2 / 2) [1 + \frac{(1 + \gamma e^{-n\sigma_0})^2}{(1 + \gamma)^2} e^{n\sigma_0}]$ , where  $\delta N_0^2$  is the photon shot-noise without atoms and  $\gamma$  is the ratio of the imaging beam intensity to the saturation intensity. Both  $\delta N_0^2$  and  $\gamma$  are experimentally calibrated. We then correct for the effect of finite resolution on the number fluctuation[30] by comparing the atom number variance in a dilute thermal cloud to its mean atom number, using  $\delta N^2 = N$ , and applying this

calibration to all fluctuations measured at lower temperatures and higher densities.

**Density-density correlation in the fluctuation measurement.** In the fluctuation measurement, we determine  $\delta n^2$  from the pixel-wise atom number variance using the formula  $\delta n^2 \lambda_{dB}^2 = \delta N^2 / A$ , which replaces the dependence on the pixel area  $A$  by a natural area scale  $\lambda_{dB}^2$ . This definition, however, does not fully eliminate the dependence on the imaging resolution spot size  $v \sim (2 \mu\text{m})^2$ . In particular, when the density-density correlation length  $\xi$  approaches or exceeds the resolution, the measured fluctuation can depend on the fixed length scale  $\sqrt{v}$ , which can complicate the scaling behavior. However, we do not see clear deviation of scale invariance and universality within our measurement uncertainties (Fig. 3.15b and 3b). We attribute this to the small variation of the non-scale invariant contribution within our limited range of sample temperature. Further analysis on the correlations and fluctuations is in progress and the result will be published elsewhere.

**Determination of the BKT critical values from the fluctuation data.** We use a hyperbolic function  $y(\tilde{\mu}) = s(\tilde{\mu} - \tilde{\mu}_c) - \sqrt{s^2(\tilde{\mu} - \tilde{\mu}_c)^2 + w^2}$  to empirically fit the crossover feature of the density fluctuation near the transition region, assuming  $\delta \tilde{n}^2(\tilde{\mu}) = D e^{y(\tilde{\mu})}$ , where the critical chemical potential  $\tilde{\mu}_c$ , the fluctuation in the superfluid regime  $D$ , the slope of the exponential rise  $s$ , and the width of the transition region  $w$  are fitting parameters. The critical phase space density is then determined from the density profile as  $\tilde{n}_c = \tilde{n}(\tilde{\mu}_c)$ . Other choices of fit functions give similar results, contributing only small systematics from the choice of different models.

**Obtaining the universal function  $H(x)$ .** We use the density profiles in the inset of Fig. 3.16a to look for critical values  $\tilde{n}_c$  and  $\tilde{\mu}_c$  such that the equations of state at all values of  $g$  collapse to a single universal curve  $H(x) = \tilde{n}(\tilde{\mu}) - \tilde{n}_c$ , where  $x = (\tilde{\mu} - \tilde{\mu}_c)/g$  is the rescaled chemical potential. To do this, we take the profile measured at  $g = 0.05 \equiv g_r$  as the reference, evaluate  $H_r(x) = \tilde{n}(g_r x + \tilde{\mu}_{c,r}) - \tilde{n}_{c,r}$  using the critical values  $\tilde{n}_{c,r}$  and  $\tilde{\mu}_{c,r}$  determined from the fluctuation crossover feature, and smoothly interpolate the data

to make a continuous reference curve  $H_r(x)$  in the range of  $|x| \leq 1$ . Using this model, we perform minimum chi-square fit to the profiles measured at all other values of  $g$  according to  $\tilde{n}(\tilde{\mu}) = \tilde{n}_c + H_r(\frac{\tilde{\mu} - \tilde{\mu}_c}{g})$ , with only  $\tilde{n}_c$  and  $\tilde{\mu}_c$  as free parameters. This procedure successfully collapses all density profiles (see Fig. 3.16a), and is independent of any theoretical model. The resulting critical values  $\tilde{n}_c$  and  $\tilde{\mu}_c$  are plotted in Fig. 3.16c-d.

### 3.4.7 Conclusion

In summary, based on *in situ* density measurements at different chemical potential, temperature, and scattering length, we have explored and confirmed the global scale invariance of a weakly-interacting 2D gas, as well as the universal behavior near the critical point. Our results provide detailed description of critical thermodynamics near the BKT transition and offer new prospects to investigate other critical phenomena near classical or quantum phase transitions. In particular, we present experimental evidence of the growing correlations in the fluctuation region through the application of the fluctuation-dissipation theorem. Further investigations into the correlations will provide new insights into the rich critical phenomena near the transition point, for instance, critical opalescence and critical slowing.

## 3.5 Extracting density-density correlations from *in situ* images of atomic quantum gases

In this section, we present a complete recipe to extract the density-density correlations and the static structure factor of a two-dimensional (2D) atomic quantum gas from *in situ* imaging. Using images of non-interacting thermal gases, we characterize and remove the systematic contributions of imaging aberrations to the measured density-density correlations of atomic samples. We determine the static structure factor and report results on

weakly interacting 2D Bose gases, as well as strongly interacting gases in a 2D optical lattice. In the strongly interacting regime, we observe a strong suppression of the static structure factor at long wavelengths.

This section is based on a published work (by C.-L. Hung, X. Zhang, L.-C. Ha, S.-K. Tung, N. Gemelke, and C. Chin) in *New J. Phys.* **13**, 075019 (2011).

### 3.5.1 Introduction

Fluctuations and correlations result from the transient dynamics of a many-body system deviating away from its equilibrium state. Generally, fluctuations are stronger at higher temperatures and when the system is more susceptible to the external forces (as governed by the fluctuation-dissipation theorem, see [106, 113]). Local fluctuations and their correlations can thus be a powerful tool to probe thermodynamics, and to identify phase transition of a many-body system due to the sudden change of the susceptibility to the thermodynamic forces.

Measurement of fluctuations and correlations on degenerate atomic gases can reveal much information about their quantum nature [114]. Experiment examples include the quantum statistics of the atoms [115, 58, 116, 117, 118], pairing correlations [119] and quantum phases in reduced dimensions [120, 121]. In these experiments, images of the sample are taken after the time-of-flight expansion in free space, from which the momentum-space correlations are extracted.

*In situ* imaging provides a new and powerful tool to examine the density fluctuations in real space [70, 30, 122, 123, 124, 125, 126, 127, 128], offering a complimentary description of the quantum state. This new tool has been used to resolve spatially separated thermodynamic phases in inhomogeneous samples. From *in situ* measurements, both Mott insulator density plateaus and a reduction of local density fluctuations were observed

[30, 125, 126, 31]. Furthermore, a universal scaling behavior was observed in the density fluctuations of 2D Bose gases [32].

Precise measurements of spatial correlations, however, present significant technical challenges. In *in situ* imaging, one typically divides the density images into small unit cells or pixels and then evaluates the statistical correlation of the signals in the cells. If both the dimension of the cell and the imaging resolution are much smaller than the correlation length of the sample, the interpretation of the result is straightforward. In practice, because the correlation length of quantum gases is typically on the order of  $1 \mu\text{m}$ , comparable to the optical wavelength that limits the image resolution, interpreting experimental data is often more difficult. Finite image resolution, due to either diffraction, aberrations or both, contributes to systematic errors and uncertainties in the fluctuation and correlation measurements.

In this section, we present a general method to determine density-density correlations and static structure factors of quantum gases by carefully investigating and removing systematics due to imaging imperfections. In Section 2, we review the static structure factor and its relation to the real space density fluctuations. In Section 3, we describe how the density fluctuation power spectrum of a non-interacting thermal gas can be used to calibrate systematics in an imperfect imaging system, and show that the measurement can be explained by aberration theory. In Section 4, we present measurements of density fluctuations in weakly interacting 2D Bose gases and strongly interacting gases in a 2D optical lattice, and extract their static structure factors from the density-density correlations.

### 3.5.2 *The density-density correlation function and the static structure factor*

We start by considering a 2D, homogeneous sample at a mean density  $\bar{n}$ . The density-density correlation depends on the separation  $\mathbf{r}_1 - \mathbf{r}_2$  between two points, and the static correlation function  $\nu(\mathbf{r})$  is defined as [129]

$$\begin{aligned}\nu(\mathbf{r}_1 - \mathbf{r}_2) &= \bar{n}^{-1} \langle \delta n(\mathbf{r}_1) \delta n(\mathbf{r}_2) \rangle \\ &= \delta(\mathbf{r}_1 - \mathbf{r}_2) + \bar{n}^{-1} \langle \hat{\Psi}^\dagger(\mathbf{r}_1) \hat{\Psi}^\dagger(\mathbf{r}_2) \hat{\Psi}(\mathbf{r}_1) \hat{\Psi}(\mathbf{r}_2) \rangle - \bar{n}\end{aligned}\quad (3.20)$$

where  $\langle \dots \rangle$  denotes the ensemble average, and  $\delta n(\mathbf{r}) = n(\mathbf{r}) - \bar{n}$  is the local density fluctuation around its mean value  $\bar{n}$ . The Dirac delta function  $\delta(\mathbf{r}_1 - \mathbf{r}_2)$  represents the auto-correlation of individual atoms, and  $\langle \hat{\Psi}^\dagger(\mathbf{r}_1) \hat{\Psi}^\dagger(\mathbf{r}_2) \hat{\Psi}(\mathbf{r}_1) \hat{\Psi}(\mathbf{r}_2) \rangle = G^{(2)}(\mathbf{r}_1 - \mathbf{r}_2)$  is the second-order correlation function [110]. When the sample is completely uncorrelated, only atomic shot noise is present and  $\nu(\mathbf{r}_1 - \mathbf{r}_2) = \delta(\mathbf{r}_1 - \mathbf{r}_2)$ . At sufficiently high phase space density, when the inter-particle separation becomes comparable to the thermal de Broglie wavelength  $\lambda_{dB}$  or the healing length, density-density correlation becomes non-zero near this characteristic correlation length scale and  $\nu(\mathbf{r})$  deviates from the simple shot noise behavior.

The static structure factor is the Fourier transform of the static correlation function [129, 130]

$$S(\mathbf{k}) = \int \nu(\mathbf{r}) e^{-i\mathbf{k}\cdot\mathbf{r}} d\mathbf{r}, \quad (3.21)$$

where  $\mathbf{k}$  is the spatial frequency wave vector. We can rewrite the static structure factor in

terms of the density fluctuation in the reciprocal space as [130]

$$S(\mathbf{k}) = \frac{\langle \delta n(\mathbf{k}) \delta n(-\mathbf{k}) \rangle}{N} = \frac{\langle |\delta n(\mathbf{k})|^2 \rangle}{N}, \quad (3.22)$$

where  $\delta n(\mathbf{k}) = \int \delta n(\mathbf{r}) e^{-i\mathbf{k}\cdot\mathbf{r}} d\mathbf{r}$ , and  $N$  is the total particle number. Here,  $\delta n(-\mathbf{k}) = \delta n^*(\mathbf{k})$  since the density fluctuation  $\delta n(\mathbf{r})$  is real. The static structure factor is therefore equal to the density fluctuation power spectrum, normalized to the total particle number  $N$ . A non-correlated gas possesses a structureless, flat spectrum  $S(\mathbf{k}) = 1$  while a correlated gas shows a non-trivial  $S(\mathbf{k})$  for  $k$  near or smaller than inverse of the correlation length  $\xi^{-1}$ .

The static structure factor reveals essential information on the collective and the statistical behavior of thermodynamic phases [113, 130, 131, 132]. It has been shown that, through the *generalized fluctuation-dissipation theorem* [107], the static structure factor of a Bose condensate is directly related to the elementary excitation energy  $\epsilon(\mathbf{k})$  as [130, 133]

$$S(\mathbf{k}) = \frac{\hbar^2 k^2}{2m\epsilon(\mathbf{k})} \coth \frac{\epsilon(\mathbf{k})}{2k_B T}, \quad (3.23)$$

where  $m$  is the atomic mass,  $T$  is the temperature,  $\hbar$  is the Planck constant  $h$  divided by  $2\pi$ , and  $k_B$  is the Boltzmann constant. See references [130, 131, 132] on the static structure factor of a general system with complex dynamic density response in the frequency domain.

Previous experimental determinations of the static structure factor in the zero-temperature limit, based on two-photon Bragg spectroscopy, have been reported for weakly interacting Bose gases [134, 135] and strongly interacting Fermi gases [136]. Here, we show that  $S(\mathbf{k})$  at finite temperatures can be directly determined from *in situ* density fluctuation and correlation measurements.

Experimental determination of  $S(\mathbf{k})$  from density fluctuations is complicated by arti-

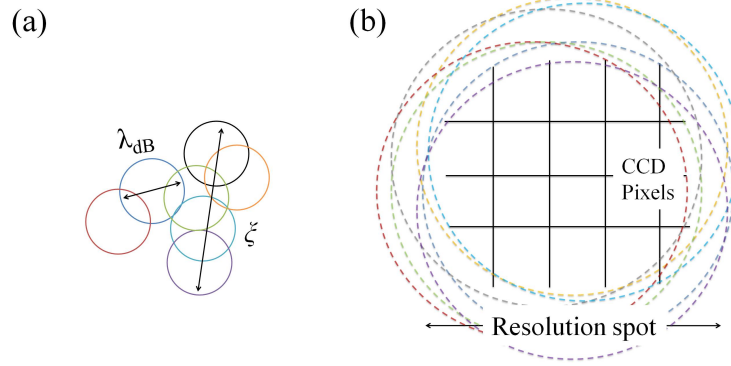


Figure 3.18: A comparison between physical length scales and measurement length scales. In (a), each atom is represented by a color circle with its diameter equal to the thermal de Broglie wavelength,  $\lambda_{dB}$ .  $\xi$  is the correlation length. An ideal measurement detects atom with perfect resolution. (b) shows the experimental condition where the image resolution is larger than the other length scales. Here, the image of an atom forms a resolution limited spot (dashed circles), and is large compared to the correlated area  $\xi^2$  and the CCD pixel area. The grid lines represent the CCD pixel array.

ficial length scales introduced by the measurement, including, for example, finite image resolution and size of the pixels in the charge-coupled device (CCD). Figure 3.18 shows a comparison between the measurement length scales (the resolution limited spot size and CCD pixel size), the correlation length  $\xi$ , and the thermal de Broglie wavelength  $\lambda_{dB}$ . Ideally, a density measurement should count the atom number inside a detection cell (pixel) with sufficiently high image resolution, and the dimension of the cell should be small compared to the atomic correlation length. In our experiment, the image resolution is determined by the imaging beam wavelength  $\lambda = 852$  nm, the numerical aperture  $N.A. = 0.28$ , and the aberrations of the imaging system. The image of a single atom on the CCD chip would form an Airy-disk like pattern with a radius comparable to or larger than  $\lambda_{dB}$  or  $\xi$ . The imaging magnification was chosen such that the CCD pixel size  $\sqrt{A} = 0.66$   $\mu\text{m}$  in the object plane is small compared to the diffraction limited spot radius  $\sim 1.8$   $\mu\text{m}$ . The atom number  $N_j$  recorded on the  $j$ -th CCD pixel is related to the atom number density  $\int dr n(\mathbf{r}) \mathcal{P}(\mathbf{r}_j - \mathbf{r})$ , assuming the point spread function  $\mathcal{P}(\mathbf{r})$  is approximately flat over the

length scale of a single pixel,

$$n_{exp}(\mathbf{r}_j) \equiv \frac{N_j}{A} \approx \int d\mathbf{r} n(\mathbf{r}) \mathcal{P}(\mathbf{r}_j - \mathbf{r}), \quad (3.24)$$

where  $\mathbf{r}_j$  is the center position of the  $j$ -th pixel in the object plane,  $n(\mathbf{r})$  is the atom number density distribution, and the integration runs over the entire  $x - y$  coordinate space. The atom number fluctuation measured at the  $j$ -th pixel is related to the density-density correlation as

$$\langle \delta N_j^2 \rangle \approx A^2 \int d\mathbf{r} \int d\mathbf{r}' \langle \delta n(\mathbf{r}) \delta n(\mathbf{r}') \rangle \mathcal{P}(\mathbf{r}_j - \mathbf{r}) \mathcal{P}(\mathbf{r}_j - \mathbf{r}'), \quad (3.25)$$

where  $\delta N_j = N_j - \langle N_j \rangle$  is the atom number fluctuation around its mean value  $\langle N_j \rangle$ .

In the Fourier space, Eq. (3.24) can be written as

$$\delta n_{exp}(\mathbf{k}_l) \approx \delta n(\mathbf{k}_l) \mathcal{P}(\mathbf{k}_l), \quad (3.26)$$

where  $\delta n_{exp}(\mathbf{k}_l) \equiv \sum_j \delta N_j e^{-i\mathbf{k}_l \cdot \mathbf{r}_j}$  is the discrete Fourier transform of  $\delta N_j$ , approximating the continuous Fourier transform. Here,  $\mathbf{k}_l = \frac{2\pi}{L}(l_x, l_y)$ ,  $L$  is the linear size of the image,  $l_x$  and  $l_y$  are integer indices in  $\mathbf{k}$ -space. From Eq. (3.22) and (3.26), the power spectrum of the density fluctuation is related to the static structure factor as

$$\langle |\delta n_{exp}(\mathbf{k}_l)|^2 \rangle \approx NS(\mathbf{k}_l) \mathcal{M}^2(\mathbf{k}_l), \quad (3.27)$$

where the modulation transfer function  $\mathcal{M}(\mathbf{k}) = |\mathcal{P}(\mathbf{k})|$  accounts for the imaging system's sensitivity at a given spatial frequency  $\mathbf{k}$ , and is determined by the point spread function. Also, from Eq. (3.25), the pixel-wise atom number fluctuation is related to the weighted

static structure factor integrated over the  $\mathbf{k}$ -space,

$$\langle \delta N_j^2 \rangle \approx \frac{\langle N_j \rangle A}{4\pi^2} \int d\mathbf{k} S(\mathbf{k}) \mathcal{M}^2(\mathbf{k}). \quad (3.28)$$

Generalization of the above calculations to arbitrary image resolution and detection cell size is straightforward. In addition to convolving with the point spread function, the measured atom number density must also be convolved with the detection cell geometry. Equation (3.24) can therefore be written as  $N_j/A = \int d\mathbf{k} n(\mathbf{k}) \mathcal{P}(\mathbf{k}) \mathcal{H}(\mathbf{k}) e^{i\mathbf{k}\cdot\mathbf{r}_j}$ , where  $\mathcal{H}(\mathbf{k}) = \int_A e^{i\mathbf{k}\cdot\mathbf{r}} d\mathbf{r}/A$  and the integration goes over the area  $A$  of the detection cell. This suggests simply replacing  $\mathcal{M}^2(\mathbf{k})$  by  $\mathcal{M}^2(\mathbf{k}) \mathcal{H}^2(\mathbf{k})$  to generalize Eq. (3.27) and (3.28). Finally, in all cases, the discrete Fourier transform defined in Eq. (3.26) should well approximate the continuous Fourier transform for spatial frequencies smaller than the sampling frequency  $1/\sqrt{A}$ .

We view the factor  $\mathcal{M}^2(\mathbf{k}) \mathcal{H}^2(\mathbf{k})$  as the general imaging response function, describing how the imaging apparatus responds to density fluctuations occurring at various spatial frequencies. To extract the static structure factor from *in situ* density correlation measurements, one therefore needs to characterize the imaging response function at all spatial frequencies to high precision. Since our pixel-size is much smaller than the diffraction and aberration limited spot size, we will from here forward assume  $\mathcal{H}^2(\mathbf{k}) = 1$ ;  $\mathcal{H}^2(\mathbf{k})$  decays around  $k \sim 4/\sqrt{A} = 6 \mu\text{m}^{-1}$  ( $1/e$  radius), which is much larger than  $k = 2\pi \text{N.A.}/\lambda = 2.1 \mu\text{m}^{-1}$ , where  $\mathcal{M}^2(\mathbf{k})$  terminates.

### 3.5.3 Measuring the imaging response function $\mathcal{M}^2(\mathbf{k})$

In this section, we show how to use density fluctuations of thermal atomic gases to determine the imaging response function  $\mathcal{M}^2(\mathbf{k})$ . Other approaches based on imaging individual atoms can be found, for example, in Refs. [137, 138].

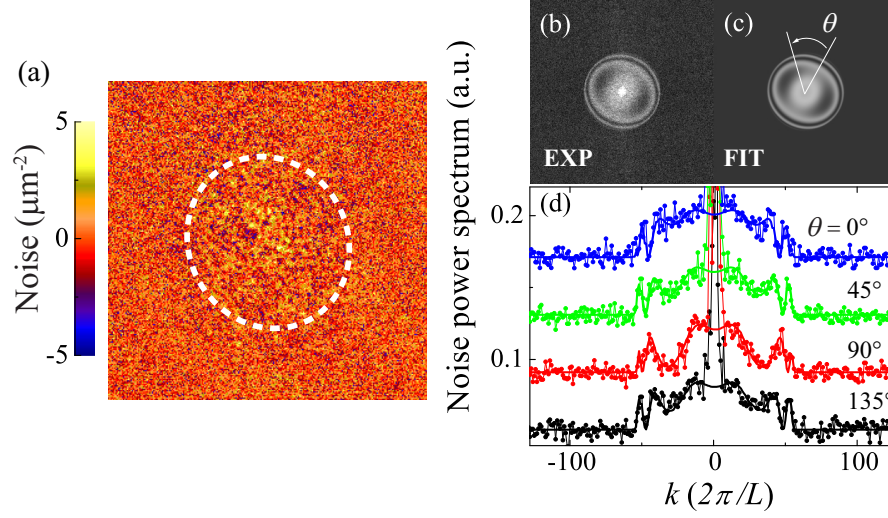


Figure 3.19: Determination of the imaging response function  $\mathcal{M}^2(\mathbf{k})$  from *in situ* images of 2D thermal gases. (a) Image noise of a 2D thermal gas, obtained by subtracting the averaged density image from a single-shot image. The dashed ellipse encircles the location of thermal atoms. (b) Noise power spectrum evaluated from 60 images, using discrete Fourier transform defined following Eq. (3.26). Zero spatial frequency is shifted to the image center. (c) Fit to the image noise power spectrum using imaging response function defined in Eq. (3.31) and aberration parameters defined in Eqs. (3.29) and (3.30). (d) Sample line-cuts of experiment (circles) and fit (solid lines), with cutting angle  $\theta$  indicated in the graph. The profiles are plotted with offset for clarity. Image size:  $L^2 = 256 \times 256$  pixels.

## Experimental setup and procedures

Measuring density fluctuations in low density thermal gases provides an easy way to precisely determine the imaging response function. An ideal thermal gas at low phase-space density has an almost constant static structure factor up to  $k = \lambda_{dB}^{-1}$  [110] which, in our case, is larger than the sampling frequency  $1/\sqrt{A}$ . Therefore, the density fluctuation power spectrum derived from an ideal thermal gas reveals the square of the modulation transfer function, as indicated by Eq. (3.27).

We prepare a 2D thermal gas by first loading a three-dimensional  $^{133}\text{Cs}$  Bose-Einstein condensate with  $2 \times 10^4$  atoms into a 2D pancake-like optical potential with trap frequencies

$\omega_z = 2\pi \times 2000$  Hz (vertical) and  $\omega_r = 2\pi \times 10$  Hz (horizontal) [31, 32]. We then heat the sample by applying magnetic field pulses near a Feshbach resonance. After sufficient thermalization time, we ramp the magnetic field to 17 G where the scattering length is nearly zero. The resulting thermal gas is non-interacting at a temperature  $T = 90$  nK and its density distribution is then recorded through *in situ* absorption imaging [32].

We evaluate the density fluctuation power spectrum  $\mathcal{M}_{exp}^2(\mathbf{k}_l) = \langle |\delta n_{exp}(\mathbf{k}_l)|^2 \rangle$  using 60 thermal gas images (size:  $256 \times 256$  pixels). Figure 3.19(a) shows a sample of the noise recorded in the images. Outside the cloud (whose boundary roughly follows the dashed line), the noise is dominated by the optical shot noise, and is therefore uncorrelated and independent of spatial frequency. In the presence of thermal atoms, we observe excess noise due to fluctuations in the thermal atom density. The noise power spectrum is shown as an image in Fig. 3.19(b), with line-cuts shown in Fig. 3.19(d). We note that the power spectrum acquires a flat offset extending to the highest spatial frequency, due to the photon shot noise in the imaging beam. Above the offset, the contribution from atomic density fluctuations is non-uniform and has a hard edge corresponding to the finite range of the imaging response function. Close to the edge, ripples in the noise power spectrum appears because of aberrations of the imaging optics, discussed in later paragraphs. Finally, the bright peak at the center corresponds to the large scale density variation due to the finite extent of the trapped atoms, and is masked out in our following analysis.

To fully understand the imaging response function with imaging imperfections, we compare our result with calculations based on Fraunhofer diffraction and aberration theory [139] as described in the following paragraphs.

## Point spread function in absorption imaging

We consider a single atom illuminated by an imaging beam, the latter is assumed to be a plane wave with a constant phase across both the object and the image planes. The atom, driven by the imaging electric field, scatters a spherical wave (dark field) which interferes destructively with the incident plane wave [140]. The dark field is clipped by the limiting aperture of the imaging optics and is distorted by the imaging aberrations. An exit pupil function  $p$  is used to describe the aberrated dark field at the exit of the imaging optics [139], and its Fourier transform  $p(\mathbf{k})$  with  $\mathbf{k} \propto \mathbf{R}$  describes the dark field distribution on the CCD chip, where  $\mathbf{R}$  is the position in the image plane. The image of a single atom is then an absorptive feature formed by the interference between the dark field and the incident plane wave in the image plane.

We extend this to absorption imaging of many atoms with density  $n(\mathbf{r}) = \sum_i \delta(\mathbf{r} - \mathbf{r}_i)$ , where  $\mathbf{r}_i$  is the location of the  $i$ -th atom in the object plane. The total scattered field in the image plane is<sup>4</sup>  $\Delta E = \sum_i \epsilon p(\mathbf{k} - \mathbf{k}_i)$ , with each atom contributing a dark field amplitude  $\epsilon$ , and  $\mathbf{k}$  relates to the position  $\mathbf{r}$  in the object plane through  $\mathbf{k} = \mathbf{r}/ad$ , where  $a$  is the radius of the limiting aperture and  $d = \lambda/(2\pi \text{N.A.})$ . The dark field  $\epsilon \propto e^{i\delta_s} E_0$  is proportional to the incident field  $E_0$ , and carries with a phase shift  $\delta_s$  associated with the laser beam detuning from atomic resonance. For a thin sample illuminated by an incident beam with intensity  $I_0$ , the beam transmission is  $t^2 = |E_0 + \Delta E|^2 / |E_0|^2 \approx 1 + 2\Re[\Delta E/E_0]$  and the atomic density  $n_{exp} \propto -\ln(t^2) + (1 - t^2)I_0/I_{sat}$  [112, 32] leads to  $n_{exp} \propto -2(1 + I_0/I_{sat})\Re[\Delta E/E_0] \propto \sum_i \Re[e^{i\delta_s} p(\mathbf{k} - \mathbf{k}_i)]$ . Here,  $\Re[\cdot]$  refers to the real part and  $I_{sat}$  is the saturation intensity for the imaging transition. Comparing the above expression to Eq. (3.24), we derive the point spread function as  $\mathcal{P}(\mathbf{r}) \propto \Re[e^{i\delta_s} p(\mathbf{k})]|_{\mathbf{k}=\mathbf{r}/ad}$ , in contrast to the form  $|p(\mathbf{k})|^2$  in the case of fluorescence or incoherent imaging.

---

4. We consider the density  $n$  of the 2D gas in a range that the photon scattering cross section remains density-independent [33].

When the dark field passes through aberrated optics, neither the amplitude nor the phase at the exit pupil is uniform, but is distorted by imperfections of the imaging system. To account for attenuation and phase distortion, We can modify the exit pupil function as

$$p(r_p, \theta_p) = U(r_p/a, \theta_p)e^{i\Theta(r_p/a, \theta_p)}, \quad (3.29)$$

where  $r_p$  and  $\theta_p$  are polar coordinates on the exit pupil,  $U(\rho, \theta)$  is the transmittance function, and  $\Theta(\rho, \theta)$  is the wavefront aberration function. We assume  $U$  to be azimuthally symmetric and model it as  $U(\rho) = H(1 - \rho)e^{-\rho^2/\tau^2}$ , where  $H(x)$  is the Heaviside step function setting a sharp cutoff when  $r_p$  reaches the radius  $a$  of the limiting aperture. The factor  $e^{-\rho^2/\tau^2}$ , with  $1/e$  radius  $r_p = a\tau$ , is used to model the weaker transmittance at large incident angle due to, e.g., finite acceptance angle of optical coatings. For the commercial objective used in the experiment, we need only to include a few terms in the wavefront aberration function

$$\Theta(\rho, \theta) \approx S_0\rho^4 + \alpha\rho^2 \cos(2\theta - 2\phi) + \beta\rho^2, \quad (3.30)$$

where the parameters used to quantify the aberrations are:  $S_0$  for spherical aberration,  $\alpha$  for astigmatism (with  $\phi$  the azimuthal angle of the misaligned optical axis), and  $\beta$  for defocusing due to atoms not in or leaving the focal plane during the imaging.

Using the exit pupil function in Eq. (3.29), we can evaluate the point spread function via  $\mathcal{P}(\mathbf{r}) \propto \Re[e^{i\delta_s} p(\mathbf{k})]|_{\mathbf{k}=\mathbf{r}/ad}$  with proper normalization. We can also calculate the modulation transfer function  $\mathcal{M}(\mathbf{k}) = |\mathcal{P}(\mathbf{k})|$ . In fact, determination of any one of  $p(\mathbf{r}_p)$ ,  $\mathcal{P}(\mathbf{r})$ , or  $\mathcal{M}(\mathbf{k})$  leads to a complete characterization of the imaging system including its imperfections.

## Modeling the imaging response function

We fit the exit pupil function  $p$  in the form of Eq. (3.29), using a discrete Fourier transform, by comparing

$$\mathcal{M}_{fit}^2 = |\mathcal{FT}(\Re[e^{i\delta_s} \mathcal{FT}(p)])|^2 \quad (3.31)$$

to the thermal gas noise power spectrum  $\mathcal{M}_{exp}^2$  shown in Fig. 3.19(b). Here,  $\mathcal{FT}(\cdot)$  denotes the discrete Fourier transform. Figure 3.19(c) shows the best fit to the measurement, which captures most of the relevant features in the experiment data. Sample line-cuts with uniform angular spacing are shown in Fig. 3.19(d). This experimental method can in principle be applied to general coherent imaging systems, provided the signal-to-noise ratio of the power spectrum image is sufficiently good to resolve all features contributed by the aberrations. Moreover, one can obtain analytic expressions for the point spread function and the modulation transfer function once the exit pupil function is known (see Section 3.5.5).

Having determined the imaging response function, one can remove systematic contributions from imaging imperfections to the static structure factor as extracted from the power spectrum of atomic density fluctuations, see Eq.(3.27).

### *3.5.4 Measuring density-density correlations and static structure factors of interacting 2D Bose gases*

We measure the density-density correlations of interacting 2D Bose gases based on the method presented in the previous sections. This study is partially motivated by a finding in our earlier work that the local density fluctuation of a 2D Bose gas is suppressed when it enters the Berezinskii-Kosterlitz-Thouless (BKT) fluctuation and the superfluid regions [32]. We attributed this phenomenon to the emergence of long density-density correlation length exceeding the size of the imaging cell and the resolution. This results in a smaller

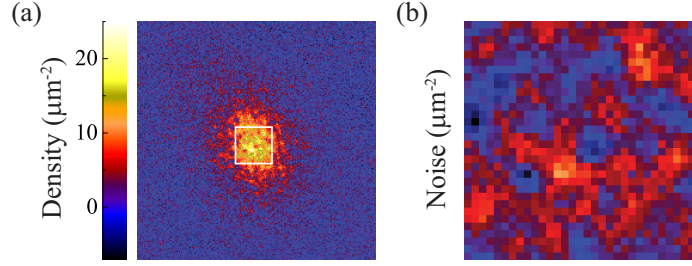


Figure 3.20: Illustration of the patch selected for the static structure factor analysis. (a) shows a typical cloud image of  $200 \times 200$  pixels. The selected patch is located at the center of the cloud, bounded by a box with an area of  $32 \times 32$  pixels. (b) shows the density fluctuations inside the patch.

pixel-wise fluctuation  $\delta N^2/A$  than the simple product of the thermal energy  $k_B T$  and the compressibility  $\kappa$ , as is expected from the classical fluctuation-dissipation theorem (FDT) [106]. Below, we present a careful analysis of the density-density correlations of interacting 2D Bose gases and discuss the role of correlations in the FDT.

To extract local properties from a trapped sample, we limit our analysis to a small central area of the sample where the density is nearly flat. In addition, the area is chosen to be large enough to offer sufficient resolution in the Fourier space. We choose the patch size to be  $32 \times 32$  pixels. Figure 3.20 shows a typical image and the density fluctuations inside the patch.

To ensure that we obtain an accurate static structure factor using the small patch, we perform a measurement on a non-interacting 2D thermal gas at a phase space density  $n\lambda_{dB}^2 = 0.5$  and compare the measured static structure factor to the theory prediction [110]. We first calculate the imaging response function  $\mathcal{M}^2(\mathbf{k})$  for a patch size of  $32 \times 32$  pixels and divide the thermal gas noise power spectrum by  $\mathcal{M}^2(\mathbf{k})$ . The resulting spectrum should represent the static structure factor of an ideal 2D thermal gas. In Fig. 3.21, we plot the azimuthally averaged static structure factor with data points uniformly spaced in  $k$ , up

to the resolution limited spatial frequency  $k = 2\pi \text{N.A.}/\lambda$ . The measured static structure factor is flat and agrees with the expected value of  $S(k) \approx 1.3$  for  $k < \lambda_{dB}^{-1} = 2 \mu\text{m}^{-15}$ .

Applying the same analysis to *interacting* 2D Bose gases, we observe very different strengths and length scales for the density fluctuations. In Fig. 3.21(a-c), we present the single-shot image noise of samples prepared under three different conditions: weakly interacting gases at the temperature  $T = 40 \text{ nK}$  (below the BKT critical point), with dimensionless interaction strength<sup>1</sup>  $g = 0.05$  and  $0.26$  (phase space density  $n\lambda_{dB}^2 = 9$  and  $7$ ); and a strongly interacting 2D gas at the temperature  $T = 8 \text{ nK}$ , prepared in a 2D optical lattice at a mean site occupancy number of  $2.6$ , and a depth of  $7 E_R$ , where  $E_R = h \times 1.3 \text{ kHz}$  is the recoil energy. Due to the tight confinement, the sample in the optical lattice has a high effective interaction strength<sup>1</sup>  $g_{\text{eff}} = 1.0$  [10]. Details on the preparation of the 2D gases in the bulk and in an optical lattice can be found in Refs. [32] and [10], respectively.

The difference in the density fluctuations shown in Fig. 3.21(a-c) can be characterized in their static structure factors shown in Fig. 3.21(d). We observe positive correlations above the shot noise level  $S(k) = 1$  in the two weakly interacting samples. The one at  $g = 0.05$  shows stronger density correlations at small  $k$  than does the sample at  $g = 0.26$ . The enhanced density correlations  $S(k) > 1$  at low momenta are expected since the thermally induced phonon excitations can populate states with length scale  $1/k$  longer than the healing length  $\xi = 1/\sqrt{n\bar{g}}$ . For gases with stronger interactions, excitations cost more energy and the excited states are less populated. At smaller  $g$ , the correlation length is longer and, therefore, the static structure factor decays at a smaller  $k$ .

---

5. Following the calculation in Ref. [110], we find the static correlation function of an ideal 2D thermal gas is  $\nu(r) = \delta(r) + |g_1(z, e^{-\pi r^2/\lambda_{dB}^2})|^2/g_1(z, 1)\lambda_{dB}^2$ , where  $z = e^{\mu/k_B T}$  is the local fugacity and  $g_\gamma(x, y) = \sum_{k=1}^{\infty} x^k y^{1/k}/k^\gamma$  is the generalized Bose function. Fourier transforming  $\nu(r)$  to obtain the static structure factor  $S(k)$ , we find  $S(k) \approx 1.3$  remains flat for  $k\lambda_{dB} < 1$ .

1. The dimensionless interaction strength of a weakly interacting 2D Bose gas is  $g = \sqrt{8\pi}a_s/l_z$ , where  $a_s$  is the atomic scattering length and  $l_z = \sqrt{\hbar/m\omega_z}$  is the vertical harmonic oscillator length. For a 2D gas in a 2D optical lattice, the effective interaction strength is  $g_{\text{eff}} = mUl^2/\hbar^2$  [10], where  $U$  is the on-site interaction and  $l$  is the lattice constant.

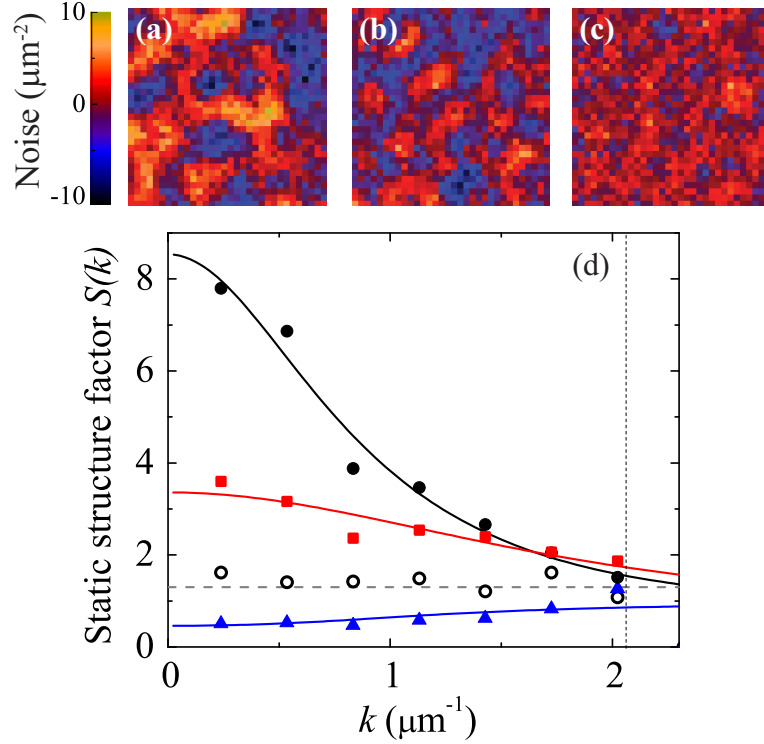


Figure 3.21: Density fluctuations and the static structure factors of 2D Bose gases. (a) and (b) Image noise of weakly interacting 2D Bose gases in the superfluid phase at dimensionless interaction strength  $g = 0.05$  and  $0.26$ . (c) Image noise of a strongly interacting 2D Bose gas at  $g_{\text{eff}} = 1.0$  prepared in a 2D optical lattice at a depth of  $7 E_R$ . (d) shows the static structure factors extracted from the noise power spectra of interacting 2D gases as shown in (a) (black circles), (b) (red squares), and (c) (blue triangles). The static structure factor of an ideal thermal gas at phase space density  $n\lambda_{dB}^2 = 0.5$  (open circles) and the expected value of  $S(k) \approx 1.3$  (gray dashed line) are plotted for comparison. Solid lines are the guides to the eye. Vertical dashed line indicates the resolution limited spatial frequency  $k = 2\pi\text{N.A.}/\lambda = 2.1 \mu\text{m}^{-1}$ .

The most intriguing observation is the negative correlations  $S(k) < 1$  in the strongly interacting gas with  $g_{\text{eff}} = 1.0$ . We observe a below-shot-noise spectrum at low momentum  $k$ , showing that long wave-length excitations are strongly suppressed due to a stronger interaction energy  $n\hbar^2 g_{\text{eff}}/m = k_B \times 34 \text{ nK}$  compared to the thermal energy  $k_B \times 8 \text{ nK}$ . As the momentum  $k$  increases, the excitation populations gradually return to the shot noise level. Our observation is consistent with the prediction in Ref. [133] that when the thermal energy drops below the interaction energy, global density fluctuations in a superfluid are suppressed.

Finally, we discuss the contribution of finite density-density correlations in the FDT. Including correlations, we can write the FDT as  $k_B T \kappa(\mathbf{r}) = \int \langle \delta n(\mathbf{r}) \delta n(\mathbf{r}') \rangle d\mathbf{r}' = n(\mathbf{r}) S(0)$  [133]. We compare the measured static structure factor, extrapolated to zero- $k$ , to the value of  $k_B T \kappa/n$ , where  $\kappa = \partial n / \partial \mu$  is the experimentally determined compressibility [32], and indeed find that  $nS(0)$  equals to  $k_B T \kappa$  to within our experimental uncertainties of  $10 \sim 20\%$  for all three interacting samples. This agreement shows that the measured correlations and thus the static structure factor can be linked to the thermodynamic quantities via the FDT. Our ability to determine  $S(0)$  and  $\kappa$  from *in situ* images also suggests a new scheme to determine temperature of the sample from local observables as  $k_B T = nS(0)/\kappa$ .

### 3.5.5 *Full analysis of the point spread function and the modulation transfer function*

#### Point spread function

Here, we describe our approach to characterize imaging imperfections using extended Nijboer-Zernike diffraction theory [141]. To obtain the point spread function from the exit pupil function  $p(r_p, \theta_p)$ , it is convenient to first decompose the exit pupil function using a

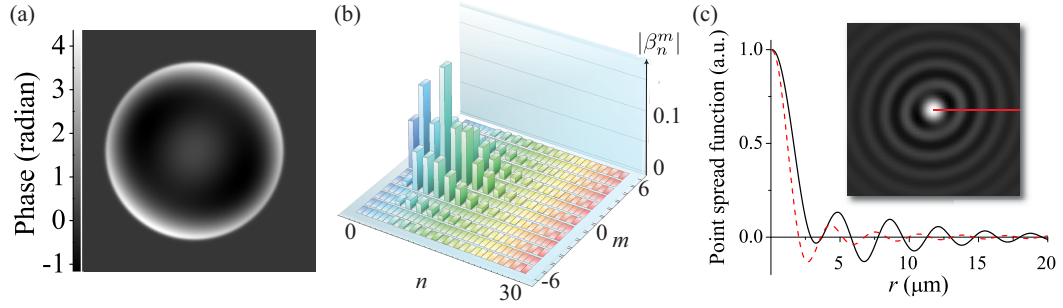


Figure 3.22: Analysis of the imaging aberrations and the point spread function. (a) shows the wavefront aberration (the phase of the exit pupil function) determined from the fit to the experiment. (b) shows the expansion coefficients  $|\beta_n^m|$  determined from Eq. (3.34), using the exit pupil function in (a). (c) shows a line-cut of the derived point spread function (solid line). The unaberrated point spread function is plotted for comparison (dashed line). Inset shows the 2D distribution of the aberrated point spread function and red line indicates the direction of the line-cut. Image size is  $(33 \mu\text{m})^2$ .

complete set of orthogonal functions on the unit disk in the polar coordinates

$$p(r_p, \theta_p) = \sum_{n=0}^{\infty} \sum_{m=-n}^n \beta_n^m Z_n^m\left(\frac{r_p}{a}, \theta_p\right), \quad (3.32)$$

where  $Z_n^m(\rho, \theta) = R_n^{|m|}(\rho)e^{im\theta}$  is a Zernike polynomial, the radial function

$$R_n^m(\rho) = \sum_{k=0}^{(n-m)/2} \frac{(-1)^k (n-k)!}{k! [(n+m)/2 - k]! [(n-m)/2 - k]!} \rho^{n-2k} \quad (3.33)$$

terminates at  $\rho = 1$ , and  $R_n^m = 0$  when  $n - m$  is odd. The expansion coefficient  $\beta_n^m$  is given by

$$\beta_n^m = \frac{n+1}{\pi a^2} \int_0^a \int_0^{2\pi} p(r_p, \theta_p) Z_n^{-m}(r_p/a, \theta_p) r_p dr_p d\theta_p. \quad (3.34)$$

If we then apply the expansion Eq. (3.32) to the Fourier transform of the exit pupil function  $p(k, \theta) = \int_0^a \int_0^{2\pi} p(r_p, \theta_p) e^{-ikr_p \cos(\theta - \theta_p)} r_p dr_p d\theta_p$  and carry out the integration using the Zernike-Bessel relation  $\int_0^1 R_n^m(\rho) J_m(\xi\rho) \rho d\rho = (-1)^{(n-m)/2} J_{n+1}(\xi)/\xi$ , we arrive at the

following formula

$$p(k, \theta) = 2\pi a^2 \sum_{n=0}^{\infty} \sum_{m=-n}^n i^n \beta_n^m e^{im(\theta+\pi)} \frac{J_{n+1}(ka)}{ka}, \quad (3.35)$$

where  $J_n(z)$  is the  $n$ -th order Bessel function of the first kind. The point spread function  $\mathcal{P}(r, \theta)$  is the real part of  $e^{i\delta_s} p(k, \theta)|_{k=r/ad}$  with proper normalization

$$\mathcal{P}(r, \theta) = \frac{1}{\mathcal{N}} \sum_{n=0}^{\infty} \sum_{m=-n}^n \Re[i^n \beta_n^m e^{im(\theta+\pi)+i\delta_s}] \frac{J_{n+1}(r/d)}{r/d}, \quad (3.36)$$

where  $\mathcal{N} = 2\pi d^2 \Re[e^{i\delta_s} p(\mathbf{r}_p)]|_{\mathbf{r}_p=0} = 2\pi d^2 \cos \delta_s$  is the normalizing factor such that  $\int \mathcal{P}(\mathbf{r}) d^2 r = 1$ . For a non-aberrated system, only  $\beta_0^0$  is non-zero and the above equation reduces to the form  $J_1(z)/z$ , as expected.

Using the above equations, we can derive the point spread function from the fitted exit pupil function shown in Fig. 3.22(a). We calculate the expansion coefficients  $\beta_n^m$  and evaluate the corresponding point spread function, see Fig. 3.22(b-c).

## Modulation transfer function

It is straightforward to evaluate the modulation transfer function  $\mathcal{M}(\mathbf{k}) = |\mathcal{P}(\mathbf{k})|$  and the imaging response function  $\mathcal{M}^2(\mathbf{k}) = |\mathcal{P}(\mathbf{k})|^2$  directly from the exit pupil function  $p(r_p, \theta_p)$ . Since the point spread function can be written as

$$\mathcal{P}(\mathbf{r}) = [e^{i\delta_s} p(\mathbf{k}) + e^{-i\delta_s} p^*(\mathbf{k})]/4\pi a^2 \mathcal{N}|_{\mathbf{k}=\mathbf{r}/ad}, \quad (3.37)$$

its Fourier transform is

$$\mathcal{P}(\mathbf{k}) = \frac{\pi d^2}{\mathcal{N}} [e^{i\delta_s} p(r_p, \theta + \pi) + e^{-i\delta_s} p^*(r_p, \theta)]|_{r_p=kad}, \quad (3.38)$$

where  $k = |\mathbf{k}|$  is the spatial frequency and  $\theta$  is the polar angle of  $\mathbf{k}$  in the image plane. From Eq. (3.38), the imaging response function is  $\mathcal{M}^2(\mathbf{k}) \propto |p(kad, \theta + \pi) + e^{-2i\delta_s} p^*(kad, \theta)|^2$ . This result shows that the phase shift  $\delta_s$  is important since  $\mathcal{M}^2(\mathbf{k})$  depends on the interference between  $p(kad, \theta + \pi)$  and  $p^*(kad, \theta)$ . The transmittance  $U$ , defined in the exit pupil function Eq. (3.29), accounts for the radial envelope in  $\mathcal{M}^2(\mathbf{k})$ , leading to the sharp edge at  $k = d^{-1} = 2\pi \text{N.A.}/\lambda$ . Either the continuous function Eq. (3.38) or the discrete Fourier model Eq. (3.31) can be used to calculate the imaging response function.

### 3.5.6 Conclusion

In this section, we demonstrated the extraction of density-density correlations and static structure factors from *in situ* images of 2D Bose gases. Careful analysis and modeling of the imaging response function allow us to fully eliminate the systematic effect of imaging imperfections on our measurements of density-density correlations. For thermal gases, our measurement of the static structure factor agrees well with theory. For interacting 2D gases below the BKT critical temperature, intriguingly, we observe positive density-density correlations in weakly interacting samples ( $g \ll 1$ ) and negative correlations in the strong interaction regime ( $g_{\text{eff}} = 1.0$ ). For all interacting gases, our static structure factor measurements agree with the prediction of the FDT as  $S(0) = k_B T \kappa / n$ . Extension of our 2D measurement can further test the prediction of anomalous density fluctuations in a condensate [129, 142, 143, 144] and strong correlations in the quantum critical region [145, 146]. Finally, our analysis can be applied to perform precise local thermometry [109] and can potentially be used to extract the local excitation energy spectrum through the application of the generalized fluctuation-dissipation theorem [130, 107].

# CHAPTER 4

## OBSERVATION OF QUANTUM CRITICALITY WITH ULTRACOLD ATOMS IN OPTICAL LATTICES

Quantum criticality emerges when a many-body system is in the proximity of a continuous phase transition that is driven by quantum fluctuations. In the quantum critical regime, exotic, yet universal properties are anticipated and discussed across a broad spectrum of physics disciplines. Ultracold atoms provide a clean system to test these predictions. Here we report the observation of quantum criticality with two-dimensional Bose gases in optical lattices. Based on *in situ* density measurements, we observe scaling behavior of the equation of state at low temperatures, locate the quantum critical point, and constrain the critical exponents. Furthermore, we observe a finite critical entropy per particle which carries a weak dependence on the atomic interaction strength. Our experiment provides a prototypical method to study quantum criticality with ultracold atoms.

This chapter is based on our work by X. Zhang, C.-L. Hung, S.-K. Tung, and C. Chin (arXiv:1109.0344, accepted by *Science*).

### **4.1 Proposal: probe quantum criticality with 2D Bose gases in optical lattices**

#### *4.1.1 Probing quantum criticality with ultracold atoms*

In the vicinity of a continuous quantum phase transition, quantum fluctuations lead to non-classical universal behavior of a many-body system [1, 11]. Quantum criticality not only provides novel routes to new material design and discovery [1, 6, 5, 4, 147], but also raises possible links between condensed matter systems and those studied in nuclear physics [148, 149] or in cosmology [1, 9]. Understanding quantum criticality and its general role in

strongly correlated systems has hence attracted significant studies such as those on heavy-fermion materials [4], Ising ferromagnets [150], and chromium at high pressure [151].

Ultracold atoms offer a clean system for a quantitative and precise study of quantum phase transitions [55, 152, 153, 154] and critical phenomena [111]. As an example, the superfluid-to-Mott insulator quantum phase transition is realized by loading atomic Bose-Einstein condensates into optical lattices [55]. In recent experiments, scaling behavior was observed in interacting Bose gases in three [111] and two dimensions [32], and in Rydberg gases [155]. Suppression of the superfluid critical temperature near the Mott transition was observed in 3D optical lattices [73]. Studying quantum criticality in cold atoms based on finite-temperature thermodynamic measurements, however, remains challenging and has attracted increasing theoretical interest in recent years [156, 157, 158, 159].

#### *4.1.2 The Superfluid-to-Mott insulator transition*

In a system of bosonic atoms confined in optical lattices, the superfluid-to-Mott insulator quantum phase transition can be described by the Bose-Hubbard model [62]. This transition is driven by the competition between two quantum energy scales: the tunneling energy  $t$  and the on-site interaction  $U$ . At zero temperature, two phases are predicted: the superfluid (SF) and Mott insulator (MI) phases. In the tunneling-dominated regime ( $g \equiv t/U \gg 1$ ), the system forms a superfluid at low temperatures; in the interaction-dominated regime ( $g \ll 1$ ), the system assumes a Mott insulator phase in the ground state. When  $g$  equals the critical value  $g_c$ , the ground state of the system is neither a superfluid nor a Mott insulator. At finite temperatures, the critical point expands into a V-shaped regime where universal scaling behaviors are expected [11, 147, 160].

In addition to the optical lattice, atoms are typically confined by an external harmonic potential, which adds new perspectives for experimental observations. Because of this

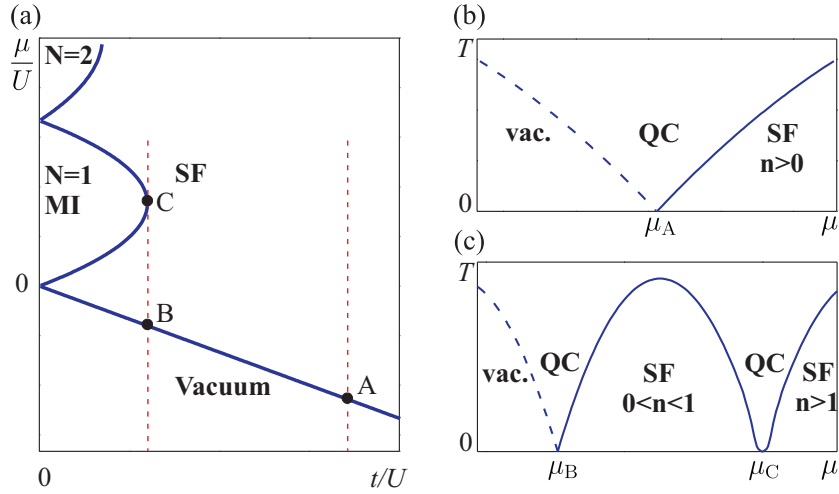


Figure 4.1: Illustrations of phase diagrams of the Bose-Hubbard model. (a) Zero-temperature phase diagram in the  $\mu/U$ - $t/U$  plane. Here MI denotes the Mott insulator state, SF denotes the superfluid state, and vacuum denotes the state with no atoms occupying the lattice sites. Density profiles of trapped gases probe lines in the phase diagram along the chemical potential  $\mu$  direction (with fixed  $t/U$ ), shown by the dashed lines. Points A, B, and C are the specific critical points on the phase boundaries referred to in the text. At finite temperatures, these critical points expand to quantum critical regions. (b) Finite-temperature phase diagram along the fixed- $t/U$  line going through the vacuum-to-superfluid transition point A at zero temperature. Here vac. denotes the vacuum state and QC denotes the quantum critical region. (c) Finite-temperature phase diagram along the fixed- $t/U$  line going through the vacuum-to-superfluid transition point B and the tip of the occupation number  $N = 1$  Mott insulator lobe (point C) at zero temperature.

potential, the system has a higher density as one moves toward the trap center [62, 30]. This density profile can reveal the phase diagram of a homogeneous system with different chemical potentials at a fixed coupling constant  $g$ , as shown in Fig. 4.1(a). A system with a large and negative chemical potential is in a vacuum state. As one increases the chemical potential, the system evolves into the superfluid state. For small enough  $g$  and larger chemical potential, the system can enter the Mott insulator state with unit occupation number. Typically, the harmonic potential is slowly varying compared to the optical lattice potential, and the density distribution is expected to be slowly varying over the length scale of the lattice constant. With a weak harmonic confinement, the local density approximation applies, and every point in the system can be viewed as a homogeneous sub-system with a local chemical potential. Therefore, a measured density profile probes a line in the phase diagram along the chemical potential direction. Near the phase boundary, the line crosses the quantum critical regime of our research interest, as shown in Fig. 4.1.

### 4.1.3 *Critical exponents and universality classes*

Near a continuous quantum phase transition, characteristic physical quantities can show singular behaviors. For example, when the system approaches the superfluid-to-Mott insulator transition from the MI side, the gap energy to particle-hole excitations will vanish; similarly, when the system approaches the transition from the superfluid side, the characteristic energy scale related to the phonon excitations will vanish. If we denote this vanishing energy scale as  $\Delta$ , we can write

$$\Delta \propto (g - g_c)^{z\nu}, \quad (4.1)$$

where  $z$  and  $\nu$  are generic exponents [11]. Similarly, a characteristic length scale  $\xi$  diverges at the transition point:

$$\xi \sim (g - g_c)^{-\nu}. \quad (4.2)$$

Here  $z$  and  $\nu$  are called the dynamical critical exponent and the correlation length exponent, respectively. Here we see that for a continuous quantum phase transition, the characteristic time scale ( $T$ ) and the characteristic length scale  $\xi$  are intrinsically linked together:

$$T \propto \frac{1}{\Delta} \propto \xi^z, \quad (4.3)$$

which is in clear contrast to a classical phase transition where time and length scales are separated.

Exponents  $z$  and  $\nu$  are two of the characteristic critical exponents that classifies a continuous phase transition. If two different phase transitions belong to the same universality class, they will share the same critical exponents and show universal behavior independent of the microscopic details. In the phase diagram shown in Fig. 4.1a, critical points at different location on the phase boundary line have different universality classes. Here we limit our discussion to two-dimensional systems. Point A and B are predicted to obey the generic dilute Bose gas universality class with  $z = 2$  and  $\nu = 1/2$  [11, 157, 61]. By comparison, point C on the tip of the MI lobe is a multi-critical point where the particle- and hole-excitations become equally possible, and has more complex critical behaviors: it belongs to the O(2) universality class with  $z = 1$  and  $\nu = 1$  [11, 157, 61] when the transition is driven by the chemical potential  $\mu$  along the vertical axis, and belongs to another set of exponents ( $z = 1$  and  $\nu = 0.67$ ) when driven by  $t/U$  along the horizontal axis [85]. In our experiment, we study the critical behavior near point A on the vacuum-to-superfluid phase boundary.

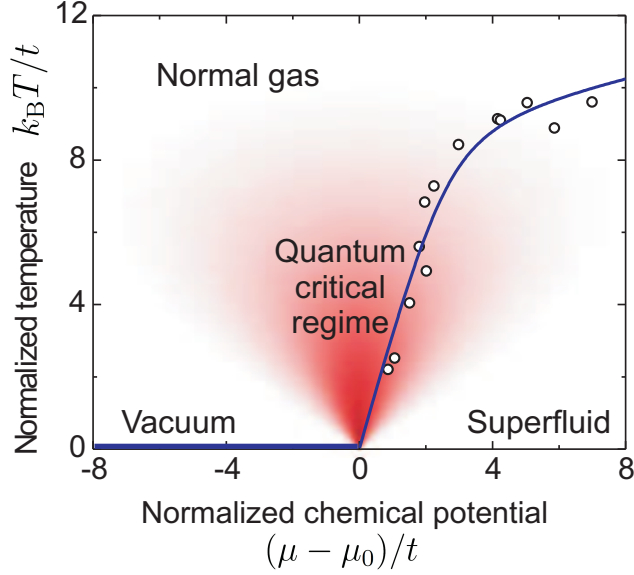


Figure 4.2: **The vacuum-to-superfluid quantum phase transition in 2D optical lattices.** At zero temperature, a quantum phase transition from vacuum (horizontal thick blue line) to superfluid occurs when the chemical potential  $\mu$  reaches the critical value  $\mu_0$ . Sufficiently close to the transition point  $\mu_0$ , quantum criticality prevails (red shaded area), and the normal-to-superfluid transition temperature  $T_c$  (measurements shown as empty circles; see section 4.2.3 for determination of the normal-to-superfluid transition point) is expected to vanish as  $T_c \sim (\mu - \mu_0)^{z\nu}$ ; the blue line is a guide to the eye. From the prediction  $z\nu = 1$  [61, 157, 158], the linearly extrapolated critical chemical potential is  $\mu_0 = -3.6(6)t$ , consistent with the theoretical value  $-4t$  [10]. Here both the thermal energy scale  $k_B T$  and chemical potential  $\mu$  are normalized by the tunneling  $t$ .

#### 4.1.4 *The vacuum-to-superfluid quantum phase transition and the predicted critical scaling laws*

The vacuum-to-superfluid transition (point A in Figure 4.1) can be viewed as a transition between Mott insulator with zero occupation number and superfluid, and can be described by the Bose-Hubbard model [61]. Our measurement is based on atomic samples near a normal-to-superfluid transition, which connects to the vacuum-to-superfluid quantum phase transition in the zero-temperature limit. The phase transition and quantum critical regime in this study are illustrated in Fig. 4.2. The zero-temperature vacuum-to-superfluid

transition occurs when the chemical potential  $\mu$  approaches the quantum critical point  $\mu_0$ . Sufficiently close to the quantum critical point, the critical temperature  $T_c$  for the normal-to-superfluid transition is expected to decrease according to the following scaling [61]:

$$\frac{k_{\text{B}}T_c}{t} = c \left( \frac{\mu - \mu_0}{t} \right)^{z\nu}, \quad (4.4)$$

where  $k_{\text{B}}$  is the Boltzmann constant,  $t$  is the tunneling energy,  $z$  is the dynamical critical exponent,  $\nu$  is the correlation length exponent, and  $c$  is a constant. In the quantum critical regime (shaded area in Fig. 4.2), the temperature  $T$  provides the sole energy scale, and all thermodynamic observables are expected to scale with  $T$  [61]. Thus the equation of state is predicted to obey the following scaling [156]

$$\tilde{N} = F(\tilde{\mu}), \quad (4.5)$$

in which  $F(x)$  is a generic function, and

$$\tilde{N} = \frac{N - N_{\text{r}}}{\left(\frac{k_{\text{B}}T}{t}\right)^{\frac{D}{z} + 1 - \frac{1}{z\nu}}} \quad \text{and} \quad \tilde{\mu} = \frac{\frac{\mu - \mu_0}{t}}{\left(\frac{k_{\text{B}}T}{t}\right)^{\frac{1}{z\nu}}} \quad (4.6)$$

are the scaled occupation number and scaled chemical potential, respectively. Here  $N$  is the occupation number,  $D$  is the dimensionality, and  $N_{\text{r}}$  is the non-universal part of the occupation number. For the vacuum-to-superfluid transition in the two-dimensional Bose-Hubbard model, we have  $N_{\text{r}} = 0$  and  $D = 2$ , and the predicted critical exponents are  $z = 2$  and  $\nu = 1/2$ , characteristics of the dilute Bose gas universality class [11, 157, 61]. We note that in an infinite 2D system, there can be logarithmic corrections to the scaling functions near the quantum critical point [11]. In real experiments with finite sample size and temperature range, however, deviations from the scaling laws due to logarithmic corrections are expected to be small [161] and are, in this work, below our measurement uncertainties.

## 4.2 Experimental setup, procedures, and analyses

### 4.2.1 Preparation of cesium 2D Bose gases in optical lattices

Our experiment is based on 2D atomic gases of cesium-133 in 2D square optical lattices [30, 31]. The 2D trap geometry is provided by the weak horizontal ( $r$ -) confinement and strong vertical ( $z$ -) confinement, with envelope trap frequencies  $f_r = 9.6$  Hz and  $f_z = 1940$  Hz, respectively. Details of the system and the sample preparation are described in a previous work [31]. Typically 4,000 to 20,000 atoms are loaded into the lattice. The lattice constant is  $d = \lambda/2 = 0.532 \mu\text{m}$  and the depth is  $V_L = 6.8 E_R$ , where  $E_R = k_B \times 63.6$  nK is the recoil energy,  $\lambda = 1064$  nm is the lattice laser wavelength, and  $h$  is the Planck constant. In the lattice, the tunneling energy is  $t = k_B \times 2.7$  nK, the on-site interaction is  $U = k_B \times 17$  nK, and the scattering length is  $a = 15.9$  nm. The sample temperature is controlled in the range of  $T = 5.8 \sim 31$  nK.

We adjust the atomic temperature by applying magnetic field pulses near a magnetic Feshbach resonance [19] to excite the atoms [32]. After the pulse, we tune the scattering length to  $a = 15.9$  nm, wait for 200 ms, and ramp on the optical lattice to  $6.8 E_R$  in 270 ms. These parameters are chosen to allow the sample to reach thermal equilibrium after the ramp [31]. The final lattice depth is sufficiently deep to validate single band Bose-Hubbard description. After preparing the sample, we perform *in situ* absorption imaging using a strong resonant laser beam [32, 34]. The atomic density is independently calibrated in similar methods as in a previous work [32].

We determine the equation of state  $n(\mu, T)$  of the sample from the measured *in situ* density distribution  $n(x, y)$  [32, 30]. The chemical potential  $\mu(x, y)$  and the temperature  $T$  are obtained by fitting the low-density tail of the sample where the atoms are normal. The fit is based on the mean-field model, Eq. 4.8, which accounts for interaction [10, 162]. Equation of state measured near the quantum critical point can reveal essential information

on quantum criticality, as proposed in a previous paper [10].

### 4.2.2 *Achieving low atomic temperatures*

In our experiment, we prepare a cold 2D Bose gas and then heat it up to various temperatures. The real challenge is to reach low enough temperatures. We started by producing an almost pure 3D BEC which should have very low temperature due to effective evaporative cooling. However, when the BEC is compressed into a single site of the vertical lattice with full strength, the evaporation will be turned off and the atoms cannot be cooled any more. To reach as low a temperature as possible, we introduce a two-step ramping up of the vertical lattice as follow. First of all, the vertical lattice is ramped to an intermediate depth which is high enough to provide substantially larger vertical confinement than the light sheet, and yet low enough such that the most energetic atoms can still escape from the trap and the rest of atoms are cooled. We finish all other changes in the dipole trapping beam intensities and in the magnetic field, and then perform the second step to ramp the vertical lattice to its full strength. This procedure maximizes the time of evaporative cooling and helps to reach lower atomic temperatures.

A second strategy is to start with a BEC with smaller atom number. In fact, if the system is in the critical regime, we only need relatively small atomic densities at low temperatures in order to reach a certain scaled occupation number. Thus we can substantially reduce the total atomic number by cutting down the final trap depth in the evaporation, which corresponds to a lower atomic temperature. In addition, we can neglect the previous step [30] of ramping to zero interaction in the vertical lattice loading, because the vertical sample size is already small enough. A smaller sample can also require less horizontal transport when atoms are compressed vertically. Based on these considerations, we significantly reduce the atom number and achieve lower temperatures (5.8 nK compared to the previous 11 nK).

### 4.2.3 Determination of the normal-to-superfluid transition point $\mu_c$

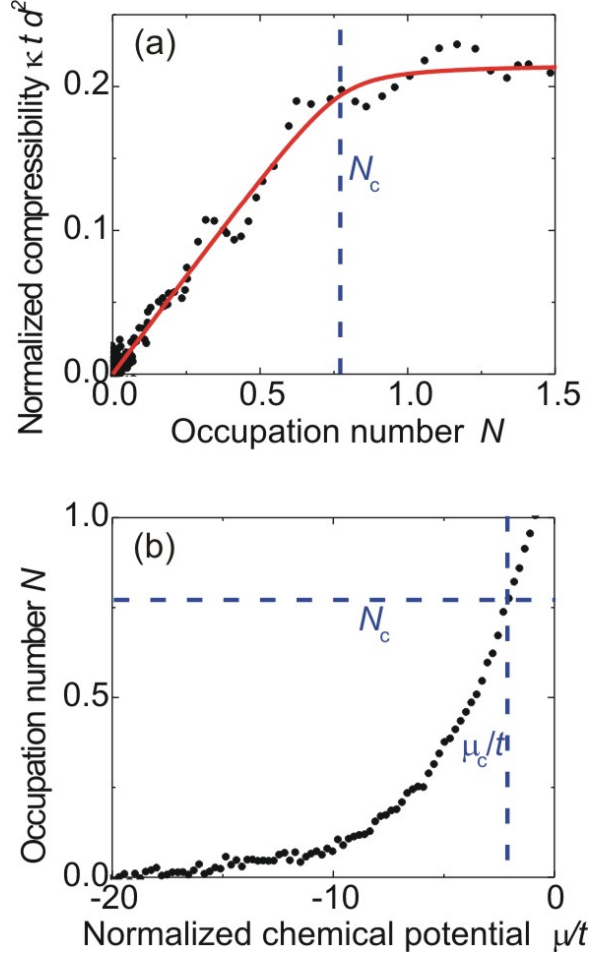


Figure 4.3: The critical chemical potential for normal-to-superfluid transition at  $T_{\text{ref}} = 4.0t/k_B$ . (a) Fit the crossover behavior to obtain  $N_c$ : data (black circles), fit (red line),  $N_c$  position (blue dashed line). (b) Use  $N_c$  to determine  $\mu_c$  based on the measured  $N(\mu/t)$  function. Here we determine  $N_c = 0.77$  and  $\mu_c = -2.1t$

To determine the normal-to-superfluid transition points (open circles in Fig. 4.2), we use a procedure similar to that in a previous work [32]. At a reference temperature  $T_{\text{ref}}$ , we obtain the critical chemical potential  $\mu_{c,\text{ref}}$  for the normal-to-superfluid transition by fitting the crossover of the compressibility  $\kappa = \frac{dn}{d\mu}$  (as a function of density  $n$ ) near the transition region, as illustrated in Fig. 4.3. The fit is based on an empirical formula  $\kappa = kn -$

$\sqrt{k^2(n - n_c)^2 + w^2} + \sqrt{k^2 n_c^2 + w^2}$ , where the slope  $k$ , critical density  $n_c = n(\mu_c, T_{\text{ref}})$ , and the width  $w$  of the transition region are fitting parameters. At a different temperature  $T$ , we obtain the transition point by comparing the equation of state at the two temperatures  $T$  and  $T_{\text{ref}}$  and collapsing the scaled equation of state near the transition points into a single curve [32], as illustrated in Fig. 4.4:

$$\frac{n - n_c}{k_B T} = H\left(\frac{\mu - \mu_c}{k_B T}\right). \quad (4.7)$$

The resulting critical points are shown in Fig. 4.2.

#### 4.2.4 Determination of the peak chemical potential and the temperature

We determine the peak chemical potential  $\mu_m$  (chemical potential at the trap center  $r = 0$ ) and the temperature  $T$  of a 2D Bose gas in 2D optical lattices by fitting the low-density tail of the azimuthally averaged density profile using the following formula [10]:

$$n(r) = d^{-2} \sum_{l=1}^{\infty} [I_0(2l\beta t)]^2 e^{l\beta[\mu_m - 2U_{\text{eff}} n d^2 - V(r)]}, \quad (4.8)$$

This formula is based on local density approximation and a mean-field model that takes interaction into account. Here  $n(r)$  is the 2D atomic density at radius  $r$  from the cloud center,  $d = 0.532 \mu\text{m}$  is the lattice spacing,  $I_0(x) = \int_{-\pi}^{\pi} \frac{d\theta}{2\pi} e^{x \cos \theta}$  is the zeroth-order Bessel function with purely imaginary argument,  $\beta = 1/k_B T$ ,  $k_B$  is the Boltzmann constant,  $t$  is the tunneling,  $V(r)$  is the envelope trapping potential, and  $U_{\text{eff}}$  is the effective interaction. Here the calculation of  $U_{\text{eff}}$  involves the Bose-Hubbard on-site interaction parameter  $U$  and terms for a modified two-particle propagator [162]:

$$U_{\text{eff}} = \frac{U}{1 + \frac{U}{2t}\Pi}, \quad (4.9)$$

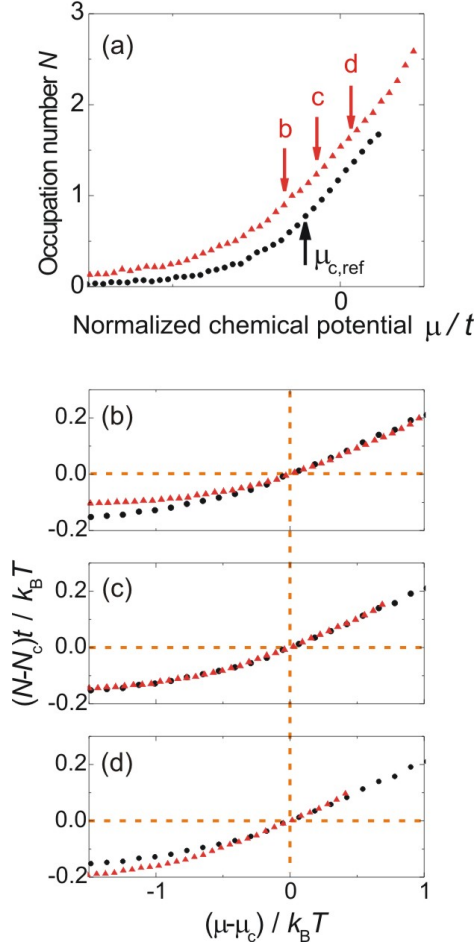


Figure 4.4: Compare the scaled equation of state near the normal-to-superfluid transition points. (a) The unscaled equation of state, occupation number  $N$  as a function of the normalized chemical potential  $\mu/t$  at two temperatures,  $T_{\text{ref}} = 4.0t/k_B$  (black circles) and  $T = 7.3t/k_B$  (red triangles). The black arrow indicates the normal-to-superfluid transition point  $\mu_{c,\text{ref}} = -2.1t$  for  $T_{\text{ref}} = 4.0t/k_B$ , as shown in Fig. 4.3; the three red arrows indicate the trial values for  $\mu_c$  at  $T = 7.3t/k_B$  used in the following three panels (b ~ d). (b) to (d) comparing the scaled equation of state  $(N - N_c)t/k_B T$  as a function of  $(\mu - \mu_c)/k_B T$  using  $\mu_{c,\text{ref}} = -2.1t$  at temperature  $T_{\text{ref}} = 4.0t/k_B$  and trial  $\mu_c = -3.4t$  in (b),  $-1.4t$  in (c), and  $0.6t$  in (d), at temperature  $T = 7.3t/k_B$ . Orange dashed lines show that the transition point always corresponds to  $(0,0)$  after the shifting and scaling. Here we see that in (c) the scaled equation of state has a better collapsing. A refined optimization gives  $\mu_c = -1.4t$  as the normal-to-superfluid transition point at  $T = 7.3t/k_B$ .

where

$$\Pi = \left(\frac{d}{2\pi}\right)^2 \iint \frac{dk_x dk_y}{\frac{k_B T}{t} + 2 [2 - \cos(k_x d) - \cos(k_y d)]},$$

and the integration ranges of  $k_x$  and  $k_y$  are both from  $-\pi/d$  to  $\pi/d$ , which covers the first Brillouin zone of the 2D square lattice. We test this formula on quantum Monte Carlo (QMC) data [158]. Within our experimental temperature range, the fitted  $T$  agrees with QMC value within 3%, and the fitted  $\mu_m$  agrees with QMC value within 0.6t.

#### 4.2.5 Effective interaction strength of a 2D gas

We define the dimensionless effective interaction strength  $g$  for our Bose gas in optical lattices:

$$g = U_{\text{eff}} \frac{m^* d^2}{\hbar^2} \quad (4.10)$$

and for that without lattices [32]:

$$g = \frac{\sqrt{8\pi} a}{l_z} \quad (4.11)$$

where the effective interaction  $U_{\text{eff}}$  is calculated using Eq. 4.9,  $\hbar$  is the reduced Planck constant,  $m^* = \hbar^2/E''(\mathbf{k})|_{\mathbf{k}=0}$  is the single-particle effective mass in a 2D optical lattice and can be calculated from the ground-band dispersion relation  $E(\mathbf{k})$ ,  $a$  is the scattering length which is tunable via a magnetic Feshbach resonance [19], and  $l_z$  is the vertical harmonic oscillator length.

### 4.3 Experimental observation of quantum criticality

In this section, we report the observation of quantum critical behavior of ultracold cesium atoms in a two-dimensional (2D) optical lattice across the vacuum-to-superfluid transition. At progressively lower temperatures, quantum criticality is revealed in the emergence of

critical scaling of the equation of state. From the equation of state, we extract the quantum critical point and the critical exponents, and compare them with theoretical predictions. Furthermore, we observe the breakdown of quantum criticality at high temperatures and estimate an upper thermal energy scale for the quantum critical behavior. The derived scaling laws permit a complete determination of the thermodynamics of the critical gas. In particular, we observe a non-zero critical entropy per particle which carries a weak dependence on the atomic interaction.

### 4.3.1 Locating the quantum critical point $\mu_0$

We locate the quantum critical point by noting that at the critical chemical potential  $\mu = \mu_0$ , the scaled occupation number  $\tilde{N} = Nt/k_{\text{B}}T = nd^2t/k_{\text{B}}T$  is temperature-independent, as indicated by Eq. 4.5. Here we have applied a predicted exponent  $\nu = 1/2$ . We plot  $\tilde{N}$  as a function of  $\mu$  in the low temperature range of 5.8~15 nK, and indeed observe a crossing point, shown in the inset of Fig. 4.5A. We quantitatively determine  $\mu_0$  as follows.

For a given chemical potential  $\mu$ , we calculate the reduced chi-squared of the scaled occupation numbers  $\tilde{N} = Nt/k_{\text{B}}T$  using measurements at  $M$  different temperatures, as shown in the following formula:

$$\chi^2(\mu) = \frac{1}{M-1} \sum_{i=1}^M \left[ \frac{\tilde{N}_i(\mu) - \tilde{N}_{\text{av}}(\mu)}{\sigma_i(\mu)} \right]^2 \quad (4.12)$$

where  $\tilde{N}_{\text{av}}(\mu) = \sum_{i=1}^M \tilde{N}_i(\mu)/M$ , and  $\sigma_i(\mu)$  is the statistical uncertainty of  $\tilde{N}_i(\mu)$ . The quantum critical point  $\mu = \mu_0$ , which corresponds to the crossing point, is determined by finding the minimum of  $\chi^2(\mu)$ . We identify this point as the critical point for the vacuum-to-superfluid transition, and our result,  $\mu_0 = -4.5(6)t$ , agrees with the prediction  $-4t$  [10].

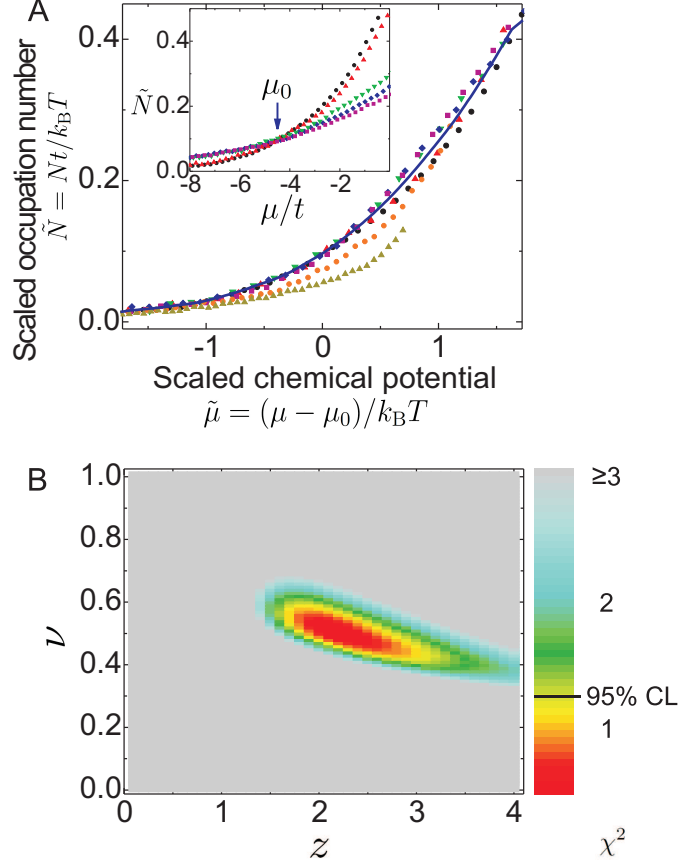


Figure 4.5: **Evidence of a quantum critical regime.** (A) Scaled occupation number  $\tilde{N} = Nt/k_B T$  as a function of the scaled chemical potential  $\tilde{\mu} = (\mu - \mu_0)/k_B T$ , measured at seven temperatures:  $T = 5.8$  nK (black circles), 6.7 nK (red triangles), 11 nK (green triangles), 13 nK (blue diamonds), 15 nK (magenta squares), 24 nK (orange circles), and 31 nK (dark yellow triangles), with the blue solid line showing the average curve for the lowest four temperatures. Inset shows the low-temperature data in the range of  $T = 5.8 \sim 15$  nK, and the critical chemical potential  $\mu_0$  is identified as the crossing point; see text. The result,  $\mu_0 = -4.5(6)t$ , agrees with the prediction  $\mu_0 = -4t$  [10]. (B) Determination of the dynamical critical exponent  $z$  and the correlation length exponent  $\nu$  based on  $\mu_0 = -4.5t$ . The color represents the reduced chi-squared,  $\chi^2$ , and indicates how well the scaled equation of state can collapse into one single curve. The exponents are determined as  $z = 2.2_{-0.5}^{+1.0}$  and  $\nu = 0.52_{-0.10}^{+0.09}$ , where the uncertainties correspond to 95% confidence level. The predicted values are  $z = 2$  and  $\nu = 1/2$ .

### 4.3.2 Testing the critical scaling law

To test the critical scaling law, we compare the equation of state at different temperatures. Based on the expected exponents  $z = 2$  and  $\nu = 1/2$ , we plot the scaled occupation number  $\tilde{N}$  as a function of the scaled chemical potential  $\tilde{\mu} = (\mu - \mu_0)/k_B T$ ; see Fig. 4.5A. Below 15 nK, all the measurements collapse into a single curve, which confirms the emergence of the quantum critical scaling law (Eq. 4.5) at low temperatures. Deviations become obvious at higher temperatures.

### 4.3.3 Constraining the critical exponents $z$ and $\nu$

We examine the range of critical exponents  $z$  and  $\nu$  that allow the scaled equation of state at low temperatures to overlap within experimental uncertainties. Taking  $\mu_0 = -4.5t$  and various values of  $z$  and  $\nu$  in the range of  $0 < z < 4$  and  $0 < \nu < 1$ , we compute the corresponding scaled occupation numbers  $\tilde{N}$  and scaled chemical potentials  $\tilde{\mu}$  based on Eq. 4.6. We then evaluate how well the scaled equation of state in the range of  $T = 5.8 \sim 15$  nK can collapse to a single curve by computing the reduced chi-squared (described later). As shown in Fig. 4.5B, the exponents are determined as  $z = 2.2_{-0.5}^{+1.0}$  and  $\nu = 0.52_{-0.10}^{+0.09}$ , where the uncertainties correspond to 95% confidence level. Based on the theoretical value of  $\mu_0 = -4t$ , we find the exponents to be  $z = 2.6_{-0.6}^{+1.2}$  and  $\nu = 0.44(8)$ . In the following analyses, we adopt  $z = 2$ ,  $\nu = 1/2$ , and  $\mu_0 = -4.5t$ .

Using a given critical chemical potential  $\mu_0$  and trial values of  $z$  and  $\nu$ , we compute the scaled occupation number  $\tilde{N}$  and the scaled chemical potential  $\tilde{\mu}$  according to Eq. 4.6. We then compute the reduced chi-squared,  $\chi^2$ , based on the deviations of  $\tilde{N}$  from the average value at the same  $\tilde{\mu}$ . By minimizing  $\chi^2$  in the range of  $-1.5 k_B T < \mu - \mu_0 < 1.5 k_B T$ , the possible values of  $z$  and  $\nu$  are constrained according to the chosen confidence level.

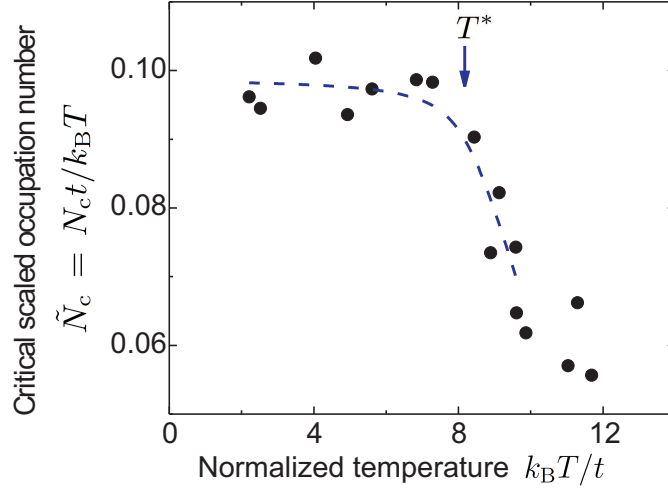


Figure 4.6: **Finite-temperature effect on quantum critical scaling.** Scaled occupation number  $\tilde{N}_c = N_{ct}/k_B T$  at the critical chemical potential  $\mu = \mu_0$  as a function of the normalized temperature  $k_B T/t$ . The blue dashed line is an empirical fit, giving a temperature scale  $T^* \approx 8t/k_B$ . For  $T < T^*$ ,  $\tilde{N}_c \approx 0.097$  is independent of the temperature; for  $T > T^*$ ,  $\tilde{N}_c$  deviates from the low-temperature value.

#### 4.3.4 Finite-temperature effect on quantum critical scaling

Our measurements at different temperatures allow us to investigate the breakdown of quantum criticality at high temperatures. To quantify the deviations, we focus on the temperature dependence of the scaled occupation number  $\tilde{N}$  at the critical chemical potential  $\mu = \mu_0$ , as shown in Fig. 4.6. Deviations from the low-temperature value are clear when the temperature exceeds  $T^* = 22 \text{ nK} \approx 8t/k_B$ . From this, we conclude that at  $\mu = \mu_0$ , the upper bound of thermal energy for the quantum critical behavior in our system is  $k_B T^* \approx 8t$ . Our result is in fair agreement with the prediction of  $6t$  based on quantum Monte Carlo calculations [158].

#### 4.3.5 Thermodynamics in the quantum critical regime

From the equation of state, one can derive other thermodynamic quantities in the critical regime. Based on the Gibbs-Duham equation [20], we derive the pressure  $P(\mu, T)$  from

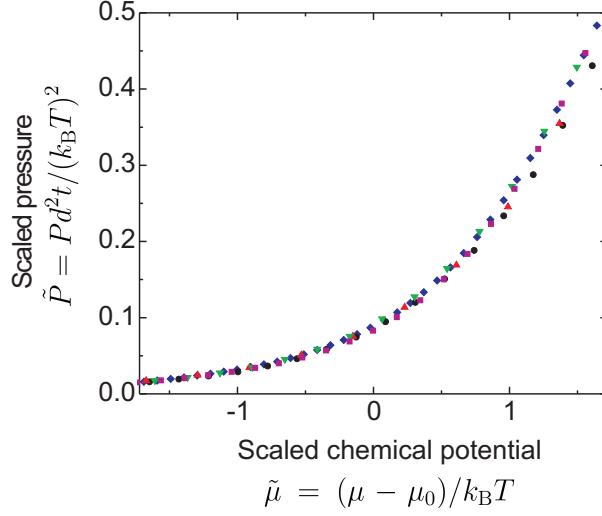


Figure 4.7: **Scaling of pressure  $P$  at low temperatures.** The symbol and color scheme is the same as that in Fig. 4.5A of the main text: black circles (5.8 nK), red triangles (6.7 nK), green triangles (11 nK), blue diamonds (13 nK), and magenta squares (15 nK). The collapse of the scaled measurements shows that the pressure scales according to Eq. 12 at low temperatures.

the *in situ* density measurements:

$$P(\mu, T) = \int_{-\infty}^{\mu} n(\mu', T) d\mu' \quad (4.13)$$

The entropy density  $s(\mu, T)$  is related to the pressure via differentiation with respect to temperature:

$$s(\mu, T) = \left( \frac{\partial P}{\partial T} \right)_{\mu} \quad (4.14)$$

We determine the pressure  $P$  using Eq. 4.13, and find that in the quantum critical regime near the vacuum-to-superfluid transition, it follows the scaling law of Eq. 4.15, see Fig. 4.7.

$$P(\mu, T) = \left( \frac{k_B T}{t} \right)^{\frac{D}{z}+1} K_P(\tilde{\mu}), \quad (4.15)$$

Thus the entropy density  $s$  follows the scaling law given by Eq. 4.16.

$$s(\mu, T) = \left( \frac{k_{\text{B}}T}{t} \right)^{\frac{D}{z}} K_s(\tilde{\mu}), \quad (4.16)$$

where  $K_P$  and  $K_s$  are generic functions of  $\tilde{\mu}$ . Combining Eq. 4.5 and Eq. 4.16, we obtain the entropy per particle  $S/N$  in unit of  $k_{\text{B}}$

$$\frac{S}{Nk_{\text{B}}} = \left( \frac{k_{\text{B}}T}{t} \right)^{-1+\frac{1}{z\nu}} W(\tilde{\mu}) \quad (4.17)$$

where  $W$  is a generic function.

For  $z = 2$ ,  $\nu = 1/2$ ,  $S/Nk_{\text{B}} = W(\tilde{\mu}) = 2K_P/K_{P'} - \tilde{\mu}$  is a temperature-independent function of the scaled chemical potential  $\tilde{\mu} = (\mu - \mu_0)/k_{\text{B}}T$ . In particular, near the critical point  $\tilde{\mu} = 0$ ,  $S/Nk_{\text{B}}$  varies approximately as a linear function of  $\tilde{\mu}$ :  $W(\tilde{\mu}) = a - b\tilde{\mu}$ . Using  $W(\tilde{\mu}) = 2K_P/K_{P'} - \tilde{\mu}$ , we can solve the pressure  $P$  and express it in terms of density  $n$  and temperature  $T$ :

$$P = Cn^x(k_{\text{B}}T)^y, \quad (4.18)$$

where  $x = \frac{2}{1+b}$ ,  $y = \frac{2b}{1+b}$ , and the proportionality constant  $C = \left(\frac{a}{2}\right)^{\frac{2}{1+b}} \left(\frac{K_P(0)}{t^2}\right)^{\frac{-1+b}{1+b}}$ .

A similar technique was applied to obtain the entropy per particle for a bulk 2D gas of rubidium-87 atoms [34].

Here we derive the entropy per particle  $S/N$  based on measurements in the temperature range of  $T = 5.8 \sim 15$  nK. The measured entropy per particle only depends on the scaled chemical potential  $\tilde{\mu}$  and monotonically decreases (Fig. 4.8A), indicating a positive specific heat. Near the critical point  $\tilde{\mu} = 0$ , the entropy per particle has an approximate linear dependence on the scaled chemical potential:  $S/Nk_{\text{B}} = a - b\tilde{\mu}$ , with  $a = 1.8(1)$ ,  $b = 1.1(1)$ . From this linear dependence, we derive an empirical thermodynamic relation

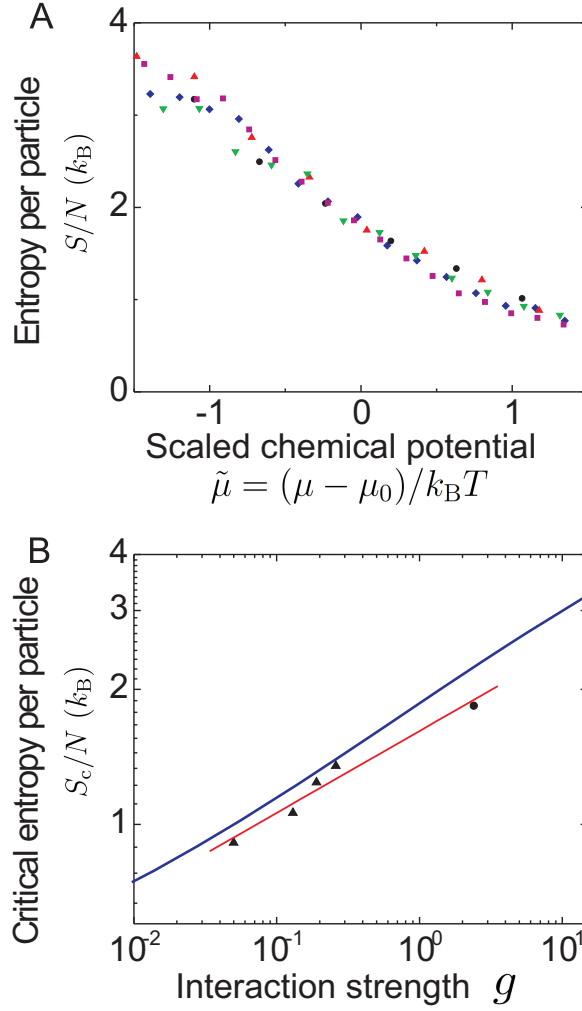


Figure 4.8: **Entropy per particle in the critical regime.** (A) Entropy per particle  $S/N$  as a function of the scaled chemical potential  $\tilde{\mu}$ , measured in the temperature range of  $5.8 \sim 15$  nK (same symbol and color scheme as in Fig. 4.5A). (B) Critical entropy per particle  $S_c/N$  as a function of the effective interaction strengths  $g$ : measurements for Bose gases with 2D optical lattices (black circle) and without lattice (black triangles, extracted from data in a previous work [32]), mean-field calculations (blue line), and a power-law fit to the measurements,  $S_c/Nk_B = 1.6(1)g^{0.18(2)}$  (red line).

analogous to the ideal gas law:

$$P = Cn^x (k_B T)^y, \quad (4.19)$$

where  $P$  is the pressure of the 2D gas,  $x = \frac{2}{1+b} = 0.95(5)$ ,  $y = \frac{2b}{1+b} = 1.05(5)$ ,  $C = 0.8(2)(td^2)^w$  is a constant, and  $w = \frac{1-b}{1+b} = -0.05(5)$ .

#### 4.3.6 *The dependence of thermodynamic observables on inter-atomic interaction strength*

We observe a weak dependence of the critical entropy per particle on the atomic interaction. Noting that a weakly-interacting 2D Bose gas follows similar scaling laws near  $\mu = 0$  [32] due to the same underlying dilute Bose gas universality class [11, 146], we apply similar analysis and extract the critical entropy per particle  $S_c/N$  at four interaction strengths  $g \approx 0.05, 0.13, 0.19, 0.26$ , as shown together with the lattice data ( $g \approx 2.4$ ) in Fig. 4.8B. We observe a slow growing of  $S_c/N$  with  $g$ , and compare the measurements with mean-field calculations. The measured  $S_c/N$  is systematically lower than the mean-field predictions, potentially due to quantum critical physics. The weak dependence on the interaction strength can be captured by a power-law fit to the data as  $S_c/Nk_B = 1.6(1)g^{0.18(2)}$ .

#### **Mean-field calculation on the entropy per particle**

Here in Fig. 4.8B, we calculate the entropy per particle  $S/N$  based on Eq. 4.8. At low temperatures  $T$ , the Bessel function takes its asymptotic form  $I_0(x) \approx e^x/\sqrt{2\pi x}$  when  $x = 2lt/(k_B T)$  is large, and Eq. 4.8 reduces to

$$F(\tilde{\mu}) = -\frac{1}{4\pi} \ln \left[ 1 - \exp \left( \tilde{\mu} - \frac{2U_{\text{eff}}}{t} F(\tilde{\mu}) \right) \right].$$

One can calculate  $F(\tilde{\mu})$  by solving this equation self-consistently, and then derive  $K_P(\tilde{\mu})$  and  $S/Nk_B = 2K_P/K_P' - \tilde{\mu}$  from  $F(\tilde{\mu})$ . In this calculation, the effective mass takes the value  $m^* = \frac{\hbar^2}{2td^2}$  (under the tight-binding approximation); the effective interaction strength is thus given by  $g = \frac{U_{\text{eff}}}{2t}$  based on Eq. 4.10.

## 4.4 Conclusion

In summary, based on *in situ* density measurements of Bose gases in 2D optical lattices, we confirm the quantum criticality near the vacuum-to-superfluid quantum phase transition. We show the suppression of the superfluid critical temperature, observe the scaling of equation of state, and extract the quantum critical point and critical exponents. In addition, we find that the entropy per particle is temperature-independent in the critical regime and has a weak dependence on the atomic interaction. Our experimental methods hold promise for identifying general quantum phase transitions, and prepare the tools for investigating quantum critical dynamics.

## CHAPTER 5

### OUTLOOK

We describe possible future directions of the cesium experiment. On the top of our list is quantum critical dynamics, an important topic in condensed matter physics which is challenging to study and remains largely unexplored. Our experiment based on cold atoms in optical lattices provides an excellent tool to investigate this topic, as described in the first section. A second direction lies in the improved measurements and analyses of local correlations in quantum gases, as described in the second section.

#### 5.1 Quantum critical dynamics

We discuss some prospects of studying quantum critical dynamics using cold atoms in optical lattices. Prominent dynamic phenomena include quantum critical transport of mass and entropy, and dynamics of defect generation across the quantum critical point as described by the Kibble-Zurek mechanism [163, 82].

This section is based on part of our proposal (by X. Zhang, C.-L. Hung, S.-K. Tung, N. Gemelke, and C. Chin) published in *New J. Phys.* 13, 045011 (2011).

##### 5.1.1 *Quantum critical transport*

Mass and heat transport across the quantum critical regime provide important tests for quantum critical theory [11]. Sufficiently close to the critical point, one expects that transport coefficients obey universal scaling relations independent of microscopic physics [11, 164]. In two dimensions, in particular, we expect that the static mass transport exhibits a universal behavior, in analogous to the prediction on the electrical conductivity [165, 9],

and the static mass conductivity at the critical point is given by

$$\sigma = \frac{m}{\hbar} \Phi_\sigma, \quad (5.1)$$

which only depends on the fundamental constants  $m/\hbar$  and a dimensionless, universal number  $\Phi_\sigma$  determined from the universality class of the underlying phase transition. Here  $\hbar$  is the reduced Planck constant, and  $m$  is the atomic mass. Analytic predictions on the transport coefficients in the quantum critical regime were recently reported on the basis of the anti-de Sitter/conformal field theory duality [9, 14]. Measurements of transport coefficients in general can be of fundamental interest in quantum field theory [9]; the relation between mass and thermal conductivities is in close analogy to the Wiedemann-Franz relation between charge and thermal transport coefficients in electronic systems, which is shown to break down near the quantum critical point in a recent experiment [166].

Mass and heat transport are induced by generalized forces such as chemical potential gradient and temperature gradient. A natural approach to study dynamics of atoms in optical lattices is to first create non-equilibrium density distributions in the sample and then measure the subsequent evolution of density profiles.

Non-equilibrium density distributions can be induced in various ways. For example, one can create a controlled perturbation in the local chemical potential and induce transport by dynamically changing the envelope trapping potential in an equilibrated system or changing the on-site interaction  $U$  near a Feshbach resonance [19]. On the other hand, applying lattice ramps slow compared to local microscopic time scales can still violate global adiabaticity and induce macroscopic mass and heat flow [31]. This is aggravated by the pronounced difference in the equilibrium density and entropy profiles between superfluid and Mott insulator phases, as shown in Fig. 5.1. In a non-equilibrated system, we expect quantum critical dynamics to take place near integer site occupation numbers.

While measuring the evolution of the density profile is straightforward using our *in situ* imaging technique [30, 31], heat or entropy measurement in the quantum critical regime remains a challenging task. Nevertheless, the entropy profile is readily measurable deeply in the Mott-insulating regime by counting occupancy statistics using single-site resolved fluorescence imaging in combination with on-site number filtering [126, 125], or can be extracted from counting average site occupancies before and after on-site number filtering processes [31]. Since the local equilibration time scale (on the order of  $\hbar/U$  [125]) is sufficiently decoupled from the global dynamics [167], a locally isentropic projection from the quantum critical regime deeply into the MI regime can be achieved and the local entropy profile measured.

From the density and entropy profile measurements, we can determine their current densities through the application of a generic continuity equation  $\frac{\partial \rho}{\partial \tau} + \nabla \cdot \vec{J}_\rho = \Gamma_\rho$ . Here  $\rho(\vec{x}, \tau)$  represents experimentally measured mass or entropy density,  $\vec{J}_\rho$  is the corresponding current density, and  $\Gamma_\rho$  is a source term which characterizes, for example, particle loss ( $\Gamma_\rho < 0$ ) or entropy generation ( $\Gamma_\rho > 0$ ).

Mass conductivity  $\sigma$  and thermal conductivity  $\kappa$  can be determined by relating the mass and entropy current densities,  $\vec{J}_n$  and  $\vec{J}_s$ , as functions of position  $\vec{x}$  and time  $\tau$ , to the generalized forces: the local chemical potential gradient  $\vec{\nabla}\mu$ , the potential energy gradient  $\vec{\nabla}V$ , and the temperature gradient  $\vec{\nabla}T$ . They obey the following transport equations [168]

$$\vec{J}_n(\vec{x}, \tau) = -\sigma \vec{\nabla}[\mu(\vec{x}, \tau) + V(\vec{x}, \tau)] - \frac{mL_{nq}}{k_B} \vec{\nabla}T(\vec{x}, \tau) \quad (5.2)$$

$$\vec{J}_s(\vec{x}, \tau) = -\frac{L_{qn}}{k_B} \vec{\nabla}[\mu(\vec{x}, \tau) + V(\vec{x}, \tau)] - \frac{\kappa}{T} \vec{\nabla}T(\vec{x}, \tau). \quad (5.3)$$

Here  $L_{nq}$  and  $L_{qn}$  are phenomenological coefficients similar to the Seebeck and Peltier coefficients in the thermoelectric effect and can be related via the Onsager reciprocity relation [169].

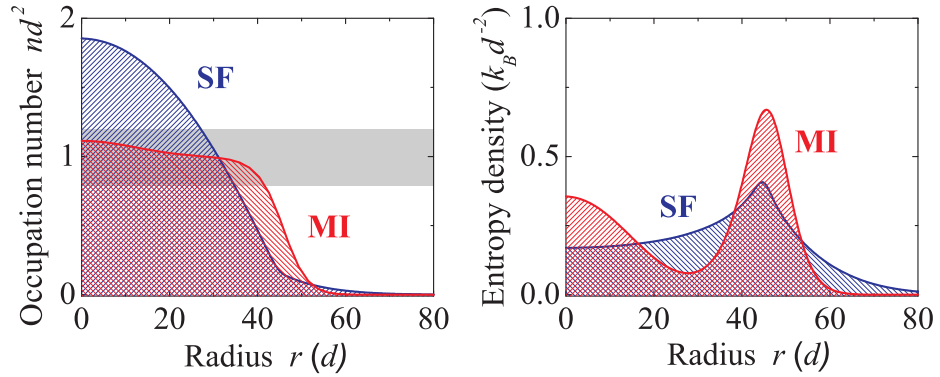


Figure 5.1: Sketch of density and entropy profiles of a trapped, finite-temperature gas in the tunneling-dominated regime where the center of the cloud is a superfluid (SF), and in the interaction-dominated regime where the cloud shows a Mott-insulating domain (MI) with unit occupation number. The calculation is done with the same particle number and total entropy for the two regimes. The gray shaded area marks an extended region near unit site occupation number ( $nd^2 = 1$ ) where quantum critical transport can take place when global adiabaticity breaks down during the lattice loading process.  $d = 532$  nm is the lattice constant.

Finally, to obtain precise information of spatially resolved chemical potential gradient and temperature gradient, we resort to the equilibrium properties of the sample which can be determined from measurements of the equilibrium density and density fluctuation. The complementary knowledge of the equation of state  $n(\mu, T)$  and its fluctuation  $\delta n^2(\mu, T)$  in equilibrium can be inverted to obtain  $\mu(n, \delta n^2)$  and  $T(n, \delta n^2)$ . We propose that, in a sample driven out of equilibrium globally but remaining locally equilibrated, local density and fluctuation measurements can still be used to extract its local chemical potential and temperature. This assumption can be further examined by comparing local compressibility to density fluctuation and extracting local temperature through the application of the fluctuation-dissipation theorem [109].

### 5.1.2 Progress on transport measurements

Our recent experiment studied global mass transport and statistical evolution in a 2D sample across the SF-MI phase boundary [31]. We discovered slow equilibration dynamics with time scales more than 100 times longer than the microscopic time scales for the on-site interaction and tunneling energy. This suggests that transport can limit the global equilibration process inside a sample traversing a quantum critical point.

In Fig. 5.2 (a-c), we plot the evolution of density profiles of a 2D gas containing  $N = 2 \times 10^4$  atoms after a short 50 ms ramp from zero to a final lattice depth of  $10 E_R$ . At this lattice depth,  $U/t = 11$  is below the critical point  $U/t = 17$  for the Mott insulator state with unit occupation number [85]. We record density profiles after holding the sample at the final lattice depth for various hold times  $\tau$ . With an equilibration time scale around 180 ms, the cloud gently expands and the peak density slowly decreases due to the increase of repulsive atomic interaction during the lattice ramp. This equilibration time scale can depend on the sample size and the local properties of the coexisting phases in an inhomogeneous sample.

We further extract the evolution of local mass current density, leading to detailed local transport properties beyond a single equilibration time scale. We compute the mass current density  $\vec{J}_n$  by comparing density profiles taken at adjacent hold times ( $\Delta\tau = 10 \sim 50$  ms) and applying the continuity equation,  $m \frac{\Delta n}{\Delta\tau} + \nabla \cdot \vec{J}_n(r, \tau) = 0$ , to evaluate  $\vec{J}_n(r, \tau)$ . Here, we assume no atom loss in the analyses for short hold times  $\tau < 500$  ms. Assuming that mass flow only occurs in the radial direction ( $\hat{r}$ ) due to azimuthal symmetry of the sample, we write the mass current density as  $\vec{J}_n(r, \tau) = mj(r, \tau)\hat{r}$ . The number current density  $j(r, \tau)$  is computed according to

$$j(r, \tau) = \frac{1}{2\pi r} \frac{N(r, \tau + \Delta\tau) - N(r, \tau)}{\Delta\tau}, \quad (5.4)$$

where  $N(r, \tau) = \int_0^r n(r', \tau) 2\pi r' dr'$  is the number of atoms located inside a circle of radius

$r$  at hold time  $\tau$ . Positive  $j$  means a current flowing toward larger radius  $r$ , and vice versa.

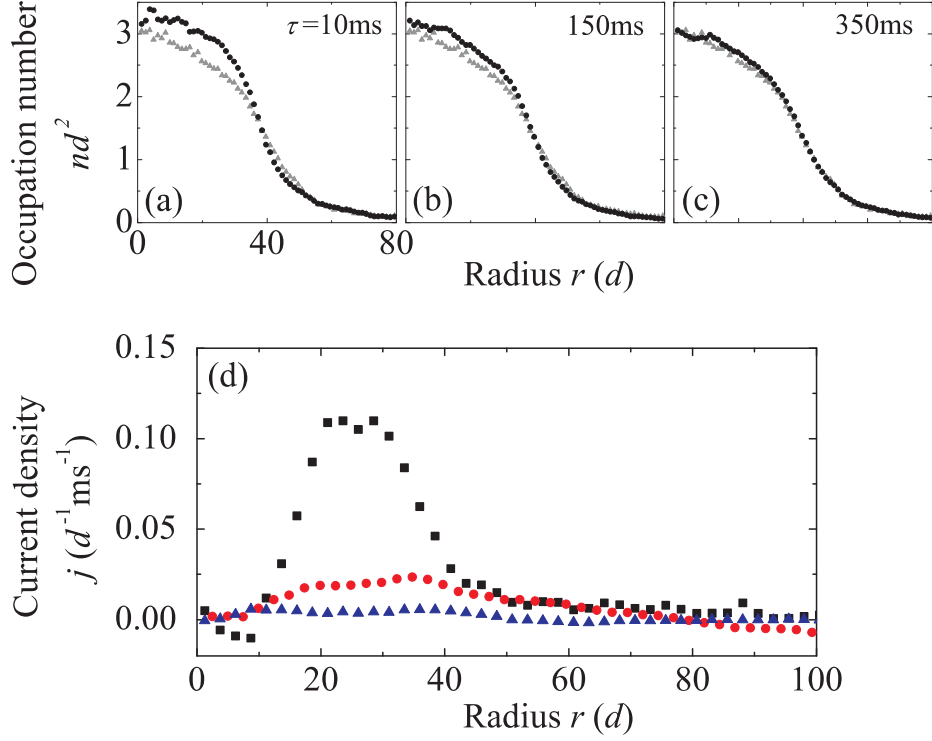


Figure 5.2: Evolution of the density profile and the atom number current density after a short 50 ms lattice ramp from zero depth to a final depth of  $10 E_R$  ( $U/t = 11$ ). Upper figure shows the density profile after holding the sample at a constant final depth for hold times  $\tau =$ (a) 10, (b) 150, and (c) 350 ms (black circles). In each figure (a-c), the near-equilibrated density profile measured at long hold time  $\tau = 500$  ms (gray triangles) is plotted for comparison. Each profile is based on an average of 20 to 30 *in situ* images. (d) shows the atom number current density at hold time  $\tau = 10$  (black squares), 150 (red circles), and 350 (blue triangles) ms, derived from the density profiles measured near hold times shown in (a-c) using Eq. (5.2).

In Fig. 5.2(d), we show  $j(r, \tau)$  computed from density profiles measured near hold times shown in Fig. 5.2 (a-c). We observe overall positive mass flow, which is consistent with the picture of an expanding sample inside the optical lattice. The mass current density varies across the sample. Shortly after the lattice ramp at  $\tau = 10$  ms, mass transport is most apparent inside a radius  $r = 40d$ , where the occupation number  $nd^2 > 1$  and the atoms respond to the increase of on-site repulsion. The current density peaks around an annular

area  $20d < r < 30d$  when the occupation number is in the range  $2 < nd^2 < 3$ ; outside this annular area, the current density is suppressed when the occupation number is in the range  $nd^2 > 3$  or  $nd^2 < 2$ . At a larger hold time  $\tau = 150$  ms, similar transport continues to take place but with smaller amplitude. At a long hold time  $\tau = 350$  ms when the sample is closer to equilibration, the current density  $j$  becomes smaller than our measurement noise.

In sum, we have shown that spatially resolved mass current density is readily measurable using our *in situ* imaging technique. We expect that local transport coefficients can be extracted using Eq. (5.2), from further measurements of local temperature gradients and chemical potential gradients. Our interest lies in mass transport in the quantum critical regimes near integer occupation numbers, where the static mass conductivity is predicted to be universal (Eq. (5.1)). Measurements of local entropy density are under future investigations, with details outlined in previous paragraphs.

### 5.1.3 Qualitative estimate of the mass conductivity

According to Eq. 5.2, the mass flow depends on both the chemical potential gradient and the temperature gradient in the sample. In the following analysis, we qualitatively estimate the mass conductivity by making two approximations: (1) we totally ignore the temperature gradient; (2) we assume the sample temperature during the profile evolution is the same as the final temperature after 500 ms holding time. Under these two assumptions, the mass flow is solely caused by the chemical potential gradient which can be estimate as follows.

In the sample after 500 ms hold time, the mass flow is negligible, and the “global chemical potential”  $F \equiv \mu + V$  in Eq. 5.2 is a constant. Note that the “local chemical potential”  $\mu$  depends primarily on the atomic interaction energy, and is a function of the local density  $n$  and temperature  $T$ . Since in our assumptions, the temperature stays the same for different times,  $\mu$  should be solely determined by  $n$ . Thus we can compare the

chemical potential at the same local density  $n$  for samples at different hold times. For the sample after a short time  $\tau$ , we write

$$\mu(n(r, \tau)) + V(r) = F(r, \tau). \quad (5.5)$$

For the sample after  $\tau_m = 500$  ms hold time, we write

$$\mu(n(r', \tau_m)) + V(r') = \text{constant}. \quad (5.6)$$

Here we define the potential energy offset such that  $V = 0$  at the trap center (with  $r = 0$ ), and write the constant as  $\mu_m$  which represents the chemical potential at the trap center (or “the global chemical potential”) for the sample after  $\tau_m = 500$  ms hold time. We also define  $r'$  as the radii where the density  $n(r', \tau_m)$  in the sample after hold time  $\tau_m$  equals to the density  $n(r, \tau)$  in the sample after hold time  $\tau$ , as illustrated in Fig. 5.3, and we see that  $r'$  is a function of  $r$ .

Since  $\mu(n(r, \tau)) = \mu(n(r', \tau_m))$  (by definition of  $r'$ ), we obtain

$$\begin{aligned} F(r, \tau) &= \text{constant} + V(r) - V(r') \\ &= \mu_m + \frac{1}{2}m\omega^2(r^2 - r'^2) \end{aligned} \quad (5.7)$$

where we applied  $V(r) = m\omega^2 r^2 / 2$ .

Using Eq. 5.2 (taking only the chemical potential gradient part on the right hand side),

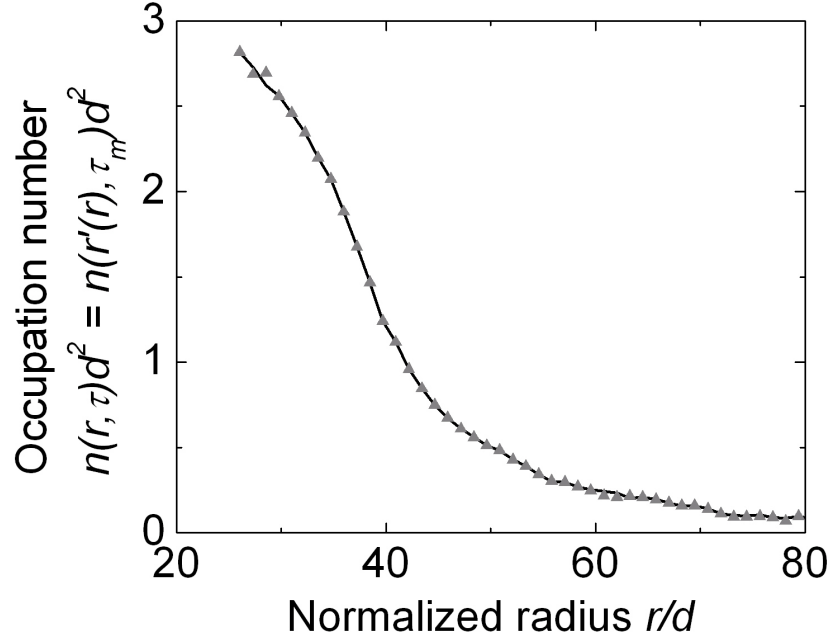


Figure 5.3: Illustration of  $n(r, \tau) = n(r', \tau_m)$ . The Black line shows the density  $n(r, \tau)$  as a function of radius  $r$  for the sample after hold time  $\tau$ . Gray triangles show  $n(r', \tau_m)$  as a function of  $r$  (since  $r'$  is a function of  $r$ ) based on the sample after hold time  $\tau_m$  and the determined  $r'$ . The overlapping of the two profiles checks our determination of  $r'$  at each  $r$  value.

we have

$$\begin{aligned}
 mj &= \vec{J}_n \cdot \hat{r} \\
 &= -\sigma[\vec{\nabla}(\mu + V)] \cdot \hat{r} \\
 &\equiv -\sigma[\vec{\nabla}F] \cdot \hat{r} \\
 &= \sigma \frac{\partial(-F)}{\partial r} \\
 &= \sigma \frac{1}{2} m \omega^2 d \frac{\partial[(r'/d)^2 - (r/d)^2]}{\partial(r/d)} \\
 &= \sigma \frac{E_d(\omega)}{d} D(r; d), \tag{5.8}
 \end{aligned}$$

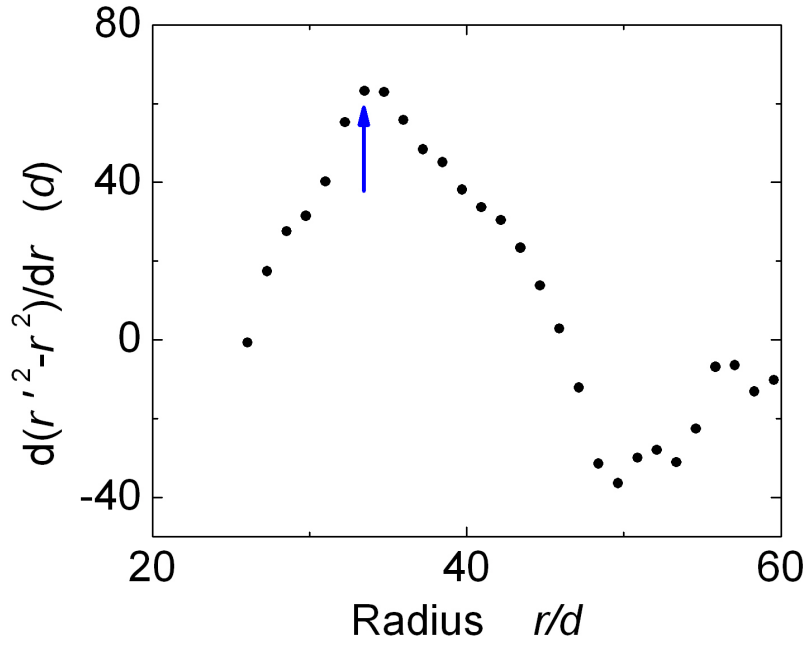


Figure 5.4: Estimate the chemical potential gradient.

where  $E_d(\omega) \equiv \frac{1}{2}m\omega^2 d^2$  is a characteristic energy scale for a system with lattice spacing  $d$  and envelope frequency  $\frac{\omega}{2\pi}$ , and  $D(r; d) \equiv \frac{\partial[(r'/d)^2 - (r/d)^2]}{\partial(r/d)}$  is a partial derivative. Thus

$$\sigma = \frac{mjd}{E_d(\omega)D(r; d)} \quad (5.9)$$

Fig. 5.4 shows the derived  $D(r; d) = \frac{\partial[(r'/d)^2 - (r/d)^2]}{\partial(r/d)}$  from Fig. 5.2a for  $\tau = 10$  ms. We indeed see a maximum derivative of 60 at  $r = 33d$ . At the same time, from Fig. 5.2d, the current density for  $\tau = 10$  ms does have a near-maximum value  $j \approx 0.09d^{-1}\text{ms}^{-1}$  at  $r = 33d$ . Here the envelope trapping frequency is  $\omega \approx 2\pi \times (1 + 10/82) \times 12 \text{ Hz} =$

$2\pi \times 13.5$  Hz [31]. Putting these numbers into Eq. 5.9, we get

$$\begin{aligned}\sigma &\approx m \frac{0.09 \text{ ms}^{-1}}{k_{\text{B}} \times 16.3 \text{ picoKelvin}} \frac{1}{60} \\ &\approx \frac{m}{\hbar} \times 0.7\end{aligned}\tag{5.10}$$

Here we have several remarks about this analysis:

- This analysis should be viewed as a practice calculation because we use a model that totally neglects the temperature gradient effect, which might be an over-simplification. At the same time, *the analysis here does serve as an order of magnitude estimation of the mass transport conductivity.*
- The discrepancy between the radii for the maximum current density and for the maximum derivative  $D(r; d) = \frac{\partial[(r'/d)^2 - (r/d)^2]}{\partial(r/d)}$  can be caused by possible temperature gradients in the sample (not considered in this analysis) or the limited signal to noise ratio in our measurements (which can affect the derivative calculation).
- The experimental procedure needs to be improved such that the mass transport is solely induced by chemical potential gradient, and that the two assumptions at the beginning of this analysis are either validated or not needed anymore. One possible approach is to keep the lattice depth the same and change only the envelope trap frequency, such that there is no temperature gradient in the cloud, and the chemical potential gradient is cleanly calibrated (that is, there is no need to compare samples after different hold times anymore).
- It is conjectured [11, 170] that the relaxation time ( $\tau_r$ ) of a system in the quantum

critical regime only depends on temperature  $T$ , the reduced Planck constant  $\hbar$ , and a universal proportionality constant  $C$  (dependent only upon the universality class)

$$\tau_r = C \frac{\hbar}{k_B T}, \quad (5.11)$$

and that  $\tau_r$  takes larger values in the non-quantum-critical regime than in the quantum critical regime. Thus under this conjecture, Eq. 5.11 provides a generic lower bound for relaxation time in interacting quantum systems; correspondingly, Eq. 5.1 provides a generic lower bound for the DC mass conductivity.

- If we assume the conjecture cited above is correct, it would be worth comparing our order of magnitude estimation, Eq. 5.10, with the theoretical formula, Eq. 5.1 (where the universal constant  $\Phi_\sigma$  is expected to be of order unity). *We see the measured proportionality constant 0.7 is of order unity and is comparable to the theoretically expected lower bound  $\Phi_\sigma$ , which means our experiment is likely free of those restricting microscopic details (such as too slow a tunneling rate) that can prevent the study of universal transport – our measurement is not “orders of magnitude off-scale” at all. This is very encouraging for our future study on quantum critical transport.*

#### 5.1.4 The Kibble-Zurek mechanism (KZM)

Based on general critical scaling arguments, the KZM predicts the formation of topological defects after a system dynamically crosses through a second-order thermodynamic [171, 172] or quantum phase transition [163, 82]. For optical lattice experiments, the KZM applies when the system is quenched from a gapped Mott insulator state to a gapless superfluid phase, and predicts that the density of defects scales with the ramp rate of the coupling

strength  $g$  [82].

The scaling behavior can reveal critical exponents of the underlying quantum phase transition [82, 173, 174]. When the coupling strength  $g$  is adiabatically ramped close to  $g_c$ , the many-body gap  $\Delta$  scales as  $\Delta \propto |g - g_c|^{z\nu} = |\lambda(\tau)|^{z\nu}$ , where  $\lambda(\tau) = g(\tau) - g_c$  characterizes the time dependence of the ramp. The adiabaticity criterion breaks down at a time  $\tau = \tau_a$  when the gap  $\Delta$  becomes small enough and the ramp rate violates  $\frac{d\Delta}{d\tau} \frac{\hbar}{\Delta} \leq \Delta$ , yielding excitations with a characteristic energy scale  $\Delta_a \propto |\lambda'(\tau_a)|^{z\nu/(z\nu+1)}$  or length scale  $\xi_a \propto \Delta_a^{-1/z}$ . The density of defects  $n_{ex}$  should therefore scale universally as [82, 173]

$$n_{ex} \propto \xi_a^{-D} \propto \gamma_a^{D\nu/(z\nu+1)}, \quad (5.12)$$

where  $\gamma_a = |\lambda'(\tau_a)|$  is the magnitude of the ramp rate at which adiabaticity fails.

In a two-dimensional superfluid, topological defects are vortices. Observing vortices in an optical lattice using *in situ* imaging is challenging, largely due to the smallness of a typical vortex core size ( $< 1 \mu\text{m}$ ) compared to the imaging resolution ( $\geq 5 \mu\text{m}$ ) available in most experiments. While the latter can be technically improved, increasing the vortex core size by reducing the atomic interaction can also be achieved experimentally either through tuning a magnetic Feshbach resonance [19] or releasing atoms for a short time-of-flight time [175, 176].

Further extensions of the KZM consider finite-temperature and finite-size effects [174]. In general, the scaling of excitations also depends on the pathway of quenching [82, 174, 177], and the system can enter the Landau-Zener regime in nearly defect-free processes [163]. Detailed experiments could reveal the wealth in the dynamics of quantum critical phenomena as well as the intriguing connection between quantum mechanics and thermodynamics in genuine quantum systems [178, 179].

## 5.2 Spatially resolved density-density correlation measurements

Correlations have fundamental importance in the study of many-body physics. In our previous work (section 3.5), we presented a scheme to extract density-density correlations from *in situ* images of atomic gases. There our analysis is based on either a large square image of thermal gases which is uncorrelated or the center  $32 \times 32$  pixels which is of a certain phase. In a general trapped gas, different quantum phases coexist and it is worth extending the previous method to analyzing an arbitrary shape of region in the cloud. We outline the generalized method and show a sample result with comparable performance compared with previous result.

Our previous analysis (section 3.5) uses 2D discrete Fourier transform (DFT) to calculate the noise power spectrum of each image, and then average over multiple experimental shots. In an actual trapped atomic sample, the local quantum phase depends on the chemical potential whose equal-value lines are often elliptical contours. Therefore, except for the phase at the trap center, other phases lie in elliptical ring regions with different radii. If we want to analyze the correlation inside a ring region (as illustrated in Fig. 5.6b), a direct discrete Fourier transform doesn't work and a different method is required.

### 5.2.1 *From atomic density of a general-shape cloud to density correlation function defined on a regular square grid*

The key idea is to separate the calculation into two steps. To calculate the static structure factor  $S(k)$  as a function of spatial frequency  $k$ , we can first calculate the correlation function  $\nu(r)$  as a function of the spatial coordinate difference  $r$  and second, perform DFT only then to derive  $S(k)$ .

We have a portion of atomic cloud, with arbitrary shape and  $Q$  pixels in it. From the average number per pixel  $N_i$  at position  $r_i$  ( $1 \leq i \leq Q$ ), we can calculate the number

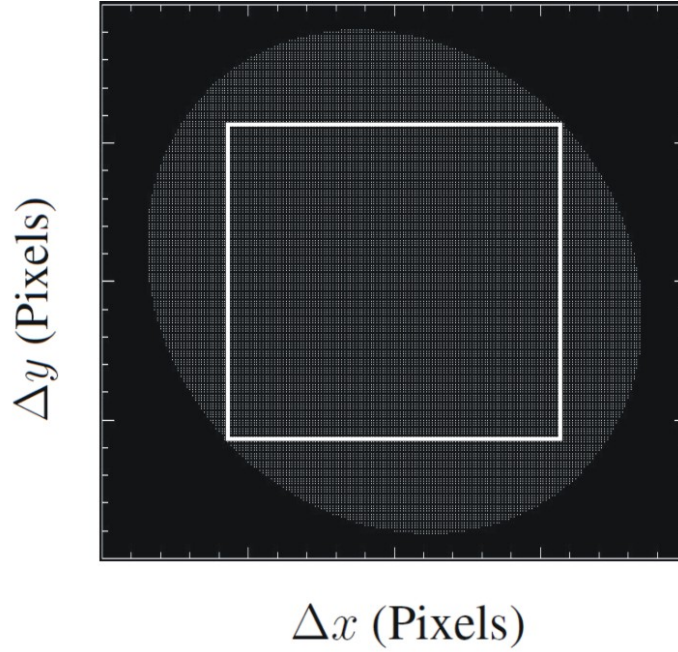


Figure 5.5: The two-point coordinate difference vector of an elliptical ring region. The sample image is represented as a 2D array of pixels. The white dots are possible coordinate difference vectors between two points in the ring region. White lines are the selected range in the  $\Delta x$ - $\Delta y$  space for later analysis.

correlation between pixel  $i$  and  $j$ :

$$\nu_{i,j} = \nu(\mathbf{r}_i - \mathbf{r}_j) = \frac{1}{A} \frac{\frac{1}{S} \sum_{q=1}^S \Delta N_{i,q} \Delta N_{j,q}}{\sqrt{N_i N_j}} \quad (5.13)$$

where  $\Delta_r$  is the linear pixel size,  $A$  is the pixel area,  $q = 1, 2, \dots, S$  corresponds to  $S$  repetitions of experiment,  $N_i = \frac{1}{S} \sum_{q=1}^S N_{i,q}$  is the average number at the  $i$ th pixel,  $\Delta N_{i,q} = N_{i,q} - N_i$  is the single-shot fluctuation. For any possible coordinate difference  $\mathbf{r} = (\Delta x, \Delta y)$ , we evaluate the correlation function  $\nu(\mathbf{r})$  on each point by averaging over all the two-point correlators  $\nu_{i,j}$  with the same coordinate difference  $\mathbf{r}$ .

As illustrated in Fig. 5.5, although a ring area can contain rather limited number of pixels, the possible coordinate differences  $\mathbf{r} = (\Delta x, \Delta y)$  can be many, and we can choose

a fairly large square range in  $(\Delta x, \Delta y)$  space for subsequent calculations. For example, one can count from (0,0) along the 45 degree and 135 degree lines and find the maximum traveling distance, and define  $L$  as the maximum even integer that do not exceed  $\min\{\max\{\text{abs}(\Delta x + \Delta y)\}, \max\{\text{abs}(\Delta x - \Delta y)\}\}$  and  $M = L/2 + 1$ , where  $\Delta x = x_i - x_j$  and  $\Delta y = y_i - y_j$  runs through all the possible pairs for points  $i, j$ . In this definition,  $L$  is the linear size of the selected square region, and  $-(M - 1) \leq \Delta x, \Delta y \leq M - 1$ .

### 5.2.2 Properly weighted discrete Fourier transform for calculating the static structure factor

The second step is to perform properly weighted discrete Fourier transform of  $\nu(\mathbf{r})$  to obtain the static structure factor  $S(\mathbf{k})$ . Defining

$$\begin{aligned} \nu_M(\mathbf{r}, \mathbf{r}') &= \frac{(M - |i - i'|)(M - |j - j'|)}{M^2} \left\langle \frac{\delta n(\mathbf{r})\delta n(\mathbf{r}')}{\bar{n}} \right\rangle \\ &= \frac{(M - |i - i'|)(M - |j - j'|)}{M^2} \nu(\mathbf{r} - \mathbf{r}') \end{aligned} \quad (5.14)$$

We calculate the static structure factor by discrete Fourier transform:

$$S(\mathbf{k}) = \sum_{\mathbf{r}-\mathbf{r}'} \Delta_r^2 \nu_M(\mathbf{r}, \mathbf{r}') e^{-i\mathbf{k}\cdot(\mathbf{r}-\mathbf{r}')} \quad (5.15)$$

where  $(\mathbf{r} - \mathbf{r}')/\Delta_r = (i - i', j - j')$  is a vector of integers in the range of  $-(M - 1) \leq i - i', j - j' \leq M - 1$ .

We note that the correlation function is modified due to the finite grid size;  $m_{\Delta i, \Delta j} = \frac{(M - |\Delta i|)(M - |\Delta j|)}{M^2}$  is the total number of point pairs for which  $i - i' = \Delta i$  and  $j - j' = \Delta j$ ; this number summed over all possible  $\Delta x$  and  $\Delta y$  gives  $M^4$ , the total number of points for

calculating the square of a 2D Fourier transform on a M by M grid:

$$\sum_{-(M-1) \leq \Delta i, \Delta j \leq M-1} m_{\Delta i, \Delta j} = M^4,$$

consistent with our previous method using a 2D grid from the beginning, and applicable to a much broader range of general cloud shapes.

This weight factor, however, requires the physical correlation length to be much smaller than the linear size  $M \times \Delta_r$  of the analysis region. Indeed, because we are assuming periodic boundary condition in performing DFT, if the physical correlation length is comparable to  $M \times \Delta_r$ , the assumption does not produce an accurate picture of the actual system any more. Thus we always need to choose a large enough region inside the cloud compared to the expected correlation length in that region. For most ring regions, the linear size  $M \times \Delta_r$  is more than  $10 \mu\text{m}$ , which far exceeds the typical correlation length, and our analysis scheme is safety applicable.

Besides, we note that the actual measurements are always convoluted with finite imaging resolution. So the analysis provides not the static structure factor  $S(k)$ , but  $S(k)M^2(k)$ , where  $M(k)$  is the modulation transfer function of the imaging system [71].

To end this section, we show that *as a calibration, the new method can produce a known answer with as good a signal-to-noise ratio as that of the previous method.* In Fig. 5.6, we show results on static structure factor ( $S(k)$ ) of thermal gases: in Fig. 5.6b, we select part of the low-density wing (marked by the gray region and the arrow) of a thermal gas; in Fig. 5.6c, we select the central  $32 \times 32$  pixels (marked by the white square box and the arrow, with phase space density of 0.5) of a thermal gas. Here the two images in Fig. 5.6b and c are only for illustrating the selected regions. We see that both results in Fig. 5.6a (black circles for (b) and red triangles for (c)) show the expected almost constant (and near unity) behavior of  $S(k)$  with comparable signal-to-noise. *This result serves as a test*

*and calibration of our new scheme based on general-shaped regions in atomic samples, and shows that the new scheme is readily applicable to further experiments on various quantum phases of interacting atomic gases.*

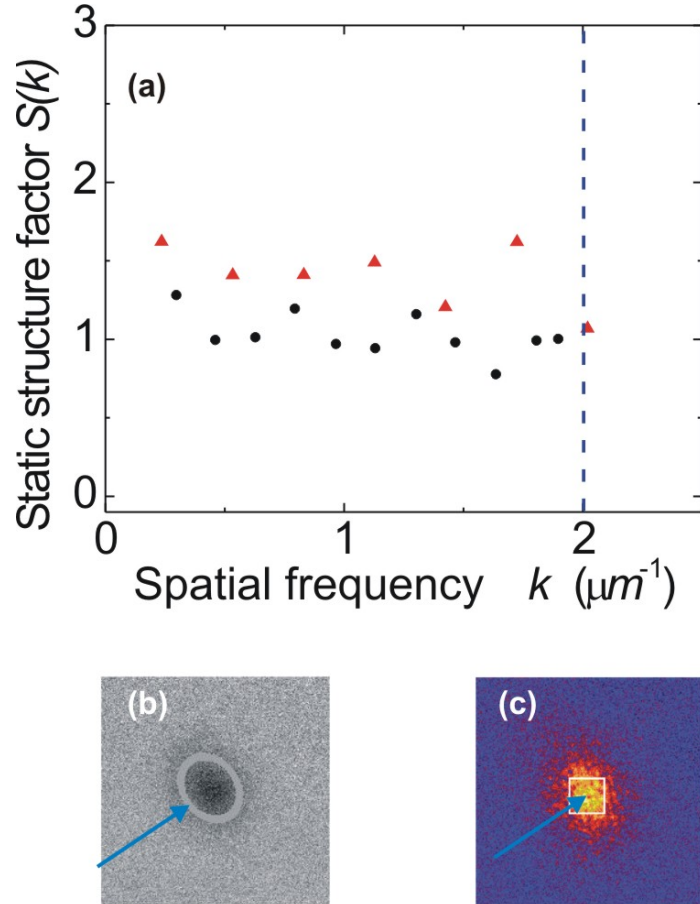


Figure 5.6: Illustration of static structure factor  $S(k)$  extracted from different-shaped atomic clouds. (a) Static structure factor as a function of spatial frequency  $k$ , extracted from thermal gases based on an elliptical ring region shown in **b** (black circles) and based on the central  $32 \times 32$  pixels shown in **c** (red triangles, extracted from the open circles in Fig. 3.21). The blue dashed line shows the resolution-limited spatial frequency of about  $2 \mu\text{m}^{-1}$ . Here we have performed azimuthal averaging of  $S(k)$  to reduce it to a 1D curve  $S(k)$ . (b) Illustration of the elliptical ring region (in gray, marked by the blue arrow) from which we extract  $S(k)$  (see also black circles in **a**). (c) Illustration of the central  $32 \times 32$  pixels (inside the white box and marked by the blue arrow) from which we extract  $S(k)$  (red triangles in **a**); this picture originally appears in Fig. 3.20a. Here the only purpose of (b) and (c) is to illustrate the shape of selected regions

## APPENDIX A

### LIST OF PUBLICATIONS

1. Fast, runaway evaporative cooling to Bose-Einstein condensation in optical traps.  
C.-L. Hung, X. Zhang, N. Gemelke, and C. Chin, *Phys. Rev. A* **78**, 011604 (2008)(Rapid communication).
2. Exploring universality of few-body physics based on ultracold atoms near Feshbach resonances.  
N. Gemelke, C.-L. Hung, X. Zhang, and C. Chin, Proceeding of 2008 ICAP.
3. *In situ* observation of incompressible Mott-insulating domains in ultracold atomic gases.  
N. Gemelke, X. Zhang, C.-L. Hung, and C. Chin, *Nature* **460**, 995 (2009).
4. Slow mass transport and statistical evolution of an atomic gas across the superfluid-Mott insulator transition.  
C.-L. Hung, X. Zhang, N. Gemelke, and C. Chin, *Phys. Rev. Lett.* **104**, 160403 (2010).
5. Observation of scale invariance and universality in two-dimensional Bose gases.  
C.-L. Hung, X. Zhang, N. Gemelke, and C. Chin, *Nature* **470**, 236-239 (2011).
6. Exploring quantum criticality based on ultracold atoms in optical lattices.  
X. Zhang, C.-L. Hung, S.-K. Tung, N. Gemelke, and C. Chin, *New Journal of Physics* **13**, 045011 (2011).
7. Extracting density-density correlations from *in situ* images of atomic quantum gases.  
C.-L. Hung, X. Zhang, L.-C. Ha, S.-K. Tung, N. Gemelke, and C. Chin, *New Journal of Physics* **13**, 075019 (2011).
8. Quantum critical behavior of ultracold atoms in two-dimensional optical lattices.  
X. Zhang, C.-L. Hung, S.-K. Tung, and C. Chin, arXiv:1109.0344 (accepted by *Science*).

## BIBLIOGRAPHY

- [1] P. Coleman, A. J. Schofield, Quantum criticality. *Nature* **433**, 226-229 (2005).
- [2] Wilson, Kenneth G., The renormalization group and critical phenomena, *Review of Modern Physics*, 55, 583 (1983).
- [3] H. E. Stanley. Scaling, universality, and renormalization: Three pillars of modern critical phenomena. *Rev. Mod. Phys.*, 71:S358–S366, 1999.
- [4] Philipp Gegenwart, Qimiao Si, and Frank Steglich. Quantum criticality in heavy-Fermion metals. *Nature Physics*, 4(3):186–197, 2008.
- [5] Hilbert v. Löhneysen, Achim Rosch, Matthias Vojta, and Peter Wölfle. Fermi-liquid instabilities at magnetic quantum phase transitions. *Rev. Mod. Phys.*, 79(3):1015–1075, Aug 2007.
- [6] D. van der Marel, H. J. A. Molegraaf, J. Zaanen, Z. Nussinov, F. Carbone, A. Damascelli, H. Eisaki, M. Greven, P. H. Kes, and M. Li. Quantum critical behaviour in a high-Tc superconductor. *Nature*, 425(6955):271–274, 2003.
- [7] Nicolas Roch, Serge Florens, Vincent Bouchiat, Wolfgang Wernsdorfer, and Franck Balestro. Quantum phase transition in a single-molecule quantum dot. *Nature*, 453:633–637, May 2008.
- [8] Hatsuda, Tetsuo and Maeda, Kenji, Quantum Phase Transitions in Dense QCD, arXiv:0912.1437v1 (2009).
- [9] Subir Sachdev and Markus Müller. Quantum criticality and black holes. *Journal of Physics: Condensed Matter*, 21(16):164216, 2009.
- [10] X. Zhang, C.-L. Hung, S.-K. Tung, N. Gemelke, and C. Chin. Exploring quantum criticality based on ultracold atoms in optical lattices. *New Journal of Physics*, 13(4):045011, 2011.
- [11] Sachdev S. *Quantum Phase Transitions*. Cambridge: Cambridge University Press, 1999.
- [12] Kedar Damle and Subir Sachdev. Nonzero-temperature transport near quantum critical points. *Physical Review B*, 56:8714–8733, October 1997.
- [13] Subir Sachdev. What can gauge-gravity duality teach us about condensed matter physics? arXiv:1108.1197v3, 2011.
- [14] Ofer Aharony, Steven S. Gubser, Juan Maldacena, Hirosi Ooguri, and Yaron Oz. Large N field theories, string theory and gravity. *Physics Reports*, 323(3-4):183 – 386, 2000.

- [15] M. H. Anderson, J. R. Ensher, M. R. Matthews, C. E. Wieman, and E. A. Cornell. Observation of Bose-Einstein condensation in a dilute atomic vapor. *Science*, 269(5221):198–201, 1995.
- [16] K. B. Davis, M. O. Mewes, M. R. Andrews, N. J. van Druten, D. S. Durfee, D. M. Kurn, and W. Ketterle. Bose-Einstein condensation in a gas of sodium atoms. *Phys. Rev. Lett.*, 75(22):3969–3973, 1995.
- [17] C. C. Bradley, C. A. Sackett, and R. G. Hulet. Bose-Einstein condensation of lithium: Observation of limited condensate number. *Phys. Rev. Lett.*, 78(6):985–989, 1997.
- [18] I. Bloch, J. Dalibard, and W. Zwerger. Many-body physics with ultracold gases. *Rev. Mod. Phys.*, 80(3):885–964, 2008.
- [19] C. Chin, R. Grimm, P. Julienne, and E. Tiesinga. Feshbach resonances in ultracold gases. *Rev. Mod. Phys.*, 82(2):1225–1286, 2010.
- [20] Tin-Lun Ho and Qi Zhou. Obtaining the phase diagram and thermodynamic quantities of bulk systems from the densities of trapped gases. *Nature Physics*, 6(2):131–134, 10.
- [21] S. Nascimbène, N. Navon, K. J. Jiang, F. Chevy, and C. Salomon. Exploring the thermodynamics of a universal Fermi gas. *Nature*, 463(7284):1057–1060, 2010.
- [22] N. Navon, S. Nascimbène, F. Chevy, and C. Salomon. The equation of state of a low-temperature Fermi gas with tunable interactions. *Science*, 328(5979):729–732, 2010.
- [23] Simon Fölling, Artur Widera, Torben Müller, Fabrice Gerbier, and Immanuel Bloch. Formation of spatial shell structure in the superfluid to Mott insulator transition. *Phys. Rev. Lett.*, 97(6):060403, 2006.
- [24] Wolfgang Petrich, Michael H. Anderson, Jason R. Ensher, and Eric A. Cornell, J. Opt. Soc. Am. B. **11**, 1332 (1994).
- [25] Xibo Zhang, Important numbers. *Group notes on experimenting* (2012).
- [26] Xibo Zhang, Mispirations: the databook of mistakes and inspirations. *Group notes on experimenting* (2012).
- [27] Chen-Lung Hung. *In situ probing of two-dimensional quantum gases*. PhD thesis, University of Chicago, 2011.
- [28] C. L. Hung, X. Zhang, N. Gemelke, and C. Chin. Accelerating evaporative cooling of atoms into Bose-Einstein condensation in optical traps. *Phys. Rev. A*, 78:011604, 2008.

- [29] Nathan Gemelke. Precise and agile magnetic coil control for deflection, levitation, and resonance imaging. *Technical note*, 2007.
- [30] N. Gemelke, X. Zhang, C. L. Hung, and C. Chin. In situ observation of incompressible Mott-insulating domains in ultracold atomic gases. *Nature*, 460(7258):995–998, 2009.
- [31] C. L. Hung, X. Zhang, N. Gemelke, and C. Chin. Slow mass transport and statistical evolution of an atomic gas across the superfluid-Mott-insulator transition. *Phys. Rev. Lett.*, 104(16):160403, 2010.
- [32] C.-L. Hung, X. Zhang, N. Gemelke, and C. Chin. Observation of scale invariance and universality in two-dimensional Bose gases. *Nature*, 470(7333):236–239, 2011.
- [33] S. P. Rath, T. Yefsah, K. J. Günter, M. Cheneau, R. Desbuquois, M. Holzmann, W. Krauth, and J. Dalibard. Equilibrium state of a trapped two-dimensional Bose gas. *Phys. Rev. A*, 82(1):013609, 2010.
- [34] T. Yefsah, R. Desbuquois, L. Chomaz, K. J. Günter, and J. Dalibard. Exploring the thermodynamics of a two-dimensional Bose gas. *Phys. Rev. Lett.*, 107, 2011.
- [35] J. Stenger, S. Inouye, D. M. Stamper-Kurn, H. J. Miesner, A. P. Chikkatur, and W. Ketterle. Spin domains in ground-state Bose-Einstein condensates. *Nature*, 396(6709):345–348, 1998. 10.1038/24567.
- [36] S. Inouye, M. R. Andrews, J. Stenger, H. J. Miesner, D. M. Stamper-Kurn, and W. Ketterle. Observation of Feshbach resonances in a Bose-Einstein condensate. *Nature*, 392(6672):151–154, 1998. 10.1038/32354.
- [37] S. Jochim, M. Bartenstein, A. Altmeyer, G. Hendl, S. Riedl, C. Chin, J. Hecker Denschlag, and R. Grimm. Bose-Einstein condensation of molecules. *Science*, 302(5653):2101–2103, 2003.
- [38] Markus Greiner, Cindy A. Regal, and Deborah S. Jin. Emergence of a molecular Bose-Einstein condensate from a Fermi gas. *Nature*, 426(6966):537–540, 2003.
- [39] M. D. Barrett, J. A. Sauer, and M. S. Chapman. All-optical formation of an atomic Bose-Einstein condensate. *Phys. Rev. Lett.*, 87(1):010404, 2001.
- [40] Tino Weber, Jens Herbig, Michael Mark, Hanns-Christoph Nagerl, and Rudolf Grimm. Bose-Einstein condensation of cesium. *Science*, 299(5604):232–235, 2003.
- [41] S. R. Granade, M. E. Gehm, K. M. O’Hara, and J. E. Thomas. All-optical production of a degenerate Fermi gas. *Phys. Rev. Lett.*, 88(12):120405, Mar 2002.

- [42] Cindy A. Regal, Christopher Ticknor, John L. Bohn, and Deborah S. Jin. Creation of ultracold molecules from a Fermi gas of atoms. *Nature*, 424(6944):47–50, 2003. 10.1038/nature01738.
- [43] Yosuke Takasu, Kenichi Maki, Kaduki Komori, Tetsushi Takano, Kazuhito Honda, Mitsutaka Kumakura, Tsutomu Yabuzaki, and Yoshiro Takahashi. Spin-singlet Bose-Einstein condensation of two-electron atoms. *Phys. Rev. Lett.*, 91(4):040404, 2003.
- [44] L Luo, B Clancy, J Joseph, J Kinast, A Turlapov, and J E Thomas. Evaporative cooling of unitary Fermi gas mixtures in optical traps. *New Journal of Physics*, 8(9):213, 2006.
- [45] Toshiya Kinoshita, Trevor Wenger, and David S. Weiss. All-optical Bose-Einstein condensation using a compressible crossed dipole trap. *Phys. Rev. A*, 71(1):011602, 2005.
- [46] T. Kraemer, J. Herbig, M. Mark, T. Weber, C. Chin, H. C. Nägerl, and R. Grimm. Optimized production of a cesium Bose-Einstein condensate. *Applied Physics B: Lasers and Optics*, 79(8):1013–1019, 2004.
- [47] Andrew J. Kerman, Vladan Vuletić, Cheng Chin, and Steven Chu. Beyond optical molasses: 3D Raman sideband cooling of atomic cesium to high phase-space density. *Phys. Rev. Lett.*, 84(3):439–442, 2000.
- [48] T. Kraemer, M. Mark, P. Waldburger, J. G. Danzl, C. Chin, B. Engeser, A. D. Lange, K. Pilch, A. Jaakkola, H.-C. Näerl, and R. Grimm. Evidence for Efimov quantum states in an ultracold gas of caesium atoms. *Nature*, 440(7082):315–318, 2006.
- [49] Cheng Chin, Vladan Vuletić, Andrew J. Kerman, Steven Chu, Eite Tiesinga, Paul J. Leo, and Carl J. Williams. Precision Feshbach spectroscopy of ultracold Cs<sub>2</sub>. *Phys. Rev. A*, 70(3):032701, Sep 2004.
- [50] W. Ketterle and N. J. Van Druten. Evaporative cooling of trapped atoms. *Advances in Atomic, Molecular, and Optical Physics*, 37:181–236, 1996.
- [51] K. M. O’Hara, M. E. Gehm, S. R. Granade, and J. E. Thomas. Scaling laws for evaporative cooling in time-dependent optical traps. *Phys. Rev. A*, 64(5):051403, 2001.
- [52] O. J. Luiten, M. W. Reynolds, and J. T. M. Walraven. Kinetic theory of the evaporative cooling of a trapped gas. *Phys. Rev. A*, 53(1):381, 1996.
- [53] E. L. Surkov, J. T. M. Walraven, and G. V. Shlyapnikov. Collisionless motion and evaporative cooling of atoms in magnetic traps. *Phys. Rev. A*, 53(5):3403, 1996.

- [54] P. W. H. Pinkse, A. Mosk, M. Weidemüller, M. W. Reynolds, T. W. Hijmans, and J. T. M. Walraven. One-dimensional evaporative cooling of magnetically trapped atomic hydrogen. *Phys. Rev. A*, 57(6):4747, 1998.
- [55] M. Greiner, O. Mandel, T. Esslinger, T. W. Hänsch, and I. Bloch. Quantum phase transition from a superfluid to a Mott insulator in a gas of ultracold atoms. *Nature*, 415(6867):39–44, 2002.
- [56] I. B. Spielman, W. D. Phillips, and J. V. Porto. Condensate fraction in a 2D Bose gas measured across the Mott-insulator transition. *Phys. Rev. Lett.*, 100(12):120402, 2008.
- [57] M. Köhl, H. Moritz, T. Stöferle, C. Schori, and T. Esslinger. Superfluid to Mott insulator transition in one, two, and three dimensions. *Journal of Low Temperature Physics*, 138(3):635–644, 2005.
- [58] Simon Fölling, Fabrice Gerbier, Artur Widera, Olaf Mandel, atjana Gericke, and Immanuel Bloch. Spatial quantum noise interferometry in expanding ultracold atom clouds. *Nature*, 434(7032):481–484, 2005.
- [59] Fabrice Gerbier, Simon Fölling, Artur Widera, Olaf Mandel, and Immanuel Bloch. Probing number squeezing of ultracold atoms across the superfluid-Mott insulator transition. *Phys. Rev. Lett.*, 96(9):090401, Mar 2006.
- [60] M. I. Kaganov and A. V. Chubukov. Interacting magnons. *Uspekhi Fizicheskikh Nauk.*, 153:537–578, 1987.
- [61] M. P. A. Fisher, P. B. Weichman, G. Grinstein, and D. S. Fisher. Boson localization and the superfluid-insulator transition. *Phys. Rev. B*, 40(1):546–570, 1989.
- [62] D. Jaksch, C. Bruder, J. I. Cirac, C. W. Gardiner, and P. Zoller. Cold bosonic atoms in optical lattices. *Phys. Rev. Lett.*, 81(15):3108–3111, 1998.
- [63] B. Capogrosso-Sansone, N. V. Prokof'ev, and B. V. Svistunov. Phase diagram and thermodynamics of the three-dimensional Bose-Hubbard model. *Phys. Rev. B*, 75(13):134302, Apr 2007.
- [64] Gretchen K. Campbell, Jongchul Mun, Micah Boyd, Patrick Medley, Aaron E. Leanhardt, Luis G. Marcassa, David E. Pritchard, and Wolfgang Ketterle. Imaging the Mott insulator shells by using atomic clock shifts. *Science*, 313(5787):649–652, 2006.
- [65] I. B. Spielman, W. D. Phillips, and J. V. Porto. Mott-insulator transition in a two-dimensional atomic Bose gas. *Phys. Rev. Lett.*, 98(8):080404, Feb 2007.

- [66] G. G. Batrouni, V. Rousseau, R. T. Scalettar, M. Rigol, A. Muramatsu, P. J. H. Denteneer, and M. Troyer. Mott domains of bosons confined on optical lattices. *Phys. Rev. Lett.*, 89(11):117203, Aug 2002.
- [67] D. S. Petrov, M. Holzmann, and G. V. Shlyapnikov. Bose-Einstein condensation in quasi-2D trapped gases. *Phys. Rev. Lett.*, 84(12):2551–2555, 2000.
- [68] F. Gerbier. Boson Mott insulators at finite temperatures. *Phys. Rev. Lett.*, 99(12):120405, 2007.
- [69] K. Hung. *Statistical Mechanics*. Wiley, 1987.
- [70] J. Esteve, J.-B. Trebbia, T. Schumm, A. Aspect, C. I. Westbrook, and I. Bouchoule. Observations of density fluctuations in an elongated Bose gas: Ideal gas and quasi-condensate regimes. *Phys. Rev. Lett.*, 96(13):130403, Apr 2006.
- [71] C.-L. Hung, X. Zhang, L.-C. Ha, S.-K. Tung, N. Gemelke, and C. Chin. Extracting density-density correlations from in situ images of atomic quantum gases. *New Journal of Physics*, 13(7):075019, 2011.
- [72] M. Lewenstein, A. Sanpera, V. Ahufinger, B. Damski, A. Sen, and U. Sen. Ultracold atomic gases in optical lattices: Mimicking condensed matter physics and beyond. *Advances in Physics*, 56(2):243–379, 2007.
- [73] S. Trotzky, L. Pollet, F. Gerbier, U. Schnorrberger, I. Bloch, N. V. Prokof'ev, B. Svistunov, and M. Troyer. Suppression of the critical temperature for superfluidity near the Mott transition. *Nature Physics*, 6(12):998–1004, 2010.
- [74] R. Jördens, N. Strohmaier, K. Günter, H. Moritz, and T. Esslinger. A Mott insulator of Fermionic atoms in an optical lattice. *Nature*, 455(7210):204–207, 2008.
- [75] U. Schneider, L. Hackermüller, S. Will, Th Best, I. Bloch, T. A. Costi, R. W. Helmes, D. Rasch, and A. Rosch. Metallic and insulating phases of repulsively interacting Fermions in a 3D optical lattice. *Science*, 322(5907):1520–1525, 2008.
- [76] J. Hubbard. Electron correlations in narrow energy bands. *Proceedings of the Royal Society of London. Series A. Mathematical and Physical Sciences*, 276(1365):238–257, 1963.
- [77] T. Kinoshita, T. Wenger, and D. S. Weiss. A quantum newton's cradle. *Nature*, 440(7086):900–903, 2006.
- [78] K. Winkler, G. Thalhammer, F. Lang, R. Grimm, J. Hecker Denschlag, A. J. Daley, A. Kantian, H. P. Büchler, and P. Zoller. Repulsively bound atom pairs in an optical lattice. *Nature*, 441(7095):853–856, 2006.

- [79] Niels Strohmaier, Daniel Greif, Robert Jördens, Leticia Tarruell, Henning Moritz, Tilman Esslinger, Rajdeep Sensarma, David Pekker, Ehud Altman, and Eugene Demler. Observation of elastic doublon decay in the Fermi-Hubbard model. *Phys. Rev. Lett.*, 104(8):080401, Feb 2010.
- [80] E. Altman, A. Polkovnikov, E. Demler, B. I. Halperin, and M. D. Lukin. Superfluid-insulator transition in a moving system of interacting bosons. *Phys. Rev. Lett.*, 95(2):020402, 2005.
- [81] J. Mun, P. Medley, G. K. Campbell, L. G. Marcassa, D. E. Pritchard, and W. Ketterle. Phase diagram for a Bose-Einstein condensate moving in an optical lattice. *Phys. Rev. Lett.*, 99(15):150604, 2007.
- [82] F. M. Cucchiatti, B. Damski, J. Dziarmaga, and W. H. Zurek. Dynamics of the Bose-Hubbard model: Transition from a Mott insulator to a superfluid. *Phys. Rev. A*, 75(2):023603, 2007.
- [83] S. R. Clark and D. Jaksch. Dynamics of the superfluids to Mott-insulator transition in one dimension. *Phys. Rev. A*, 70(4):043612, 2004.
- [84] T. Gericke, F. Gerbier, A. Widera, S. Fölling, O. Mandel, and I. Bloch. Adiabatic loading of a Bose-Einstein condensate in a 3D optical lattice. *Journal of Modern Optics*, 54(5):735–743, 2007.
- [85] Barbara Capogrosso-Sansone, Şebnem Güneş Söyler, Nikolay Prokof'ev, and Boris Svistunov. Monte Carlo study of the two-dimensional Bose-Hubbard model. *Phys. Rev. A*, 77(1):015602, Jan 2008.
- [86] T. L. Ho and Q. Zhou. Intrinsic heating and cooling in adiabatic processes for bosons in optical lattices. *Phys. Rev. Lett.*, 99(12):120404, 2007.
- [87] J. Zakrzewski and D. Delande. Breakdown of adiabaticity when loading ultracold atoms in optical lattices. *Phys. Rev. A*, 80:013602, 2009.
- [88] V. L. Berezinskii. Destruction of long-range order in one-dimensional and two-dimensional systems possessing a continuous symmetry group xii. quantum systems. *Sov. Phys. JETP*, 34:610–616, 1972.
- [89] J. M. Kosterlitz and D. J. Thouless. Ordering, metastability and phase transitions in two-dimensional systems. *Journal of Physics C: Solid State Physics*, 6(7):1181–1203, 1973.
- [90] L. P. Pitaevskii and A. Rosch. Breathing modes and hidden symmetry of trapped atoms in two dimensions. *Phys. Rev. A*, 55(2):R853–R856, 1997.

- [91] Z. Hadzibabic, P. Krüger, M. Cheneau, B. Battelier, and J. Dalibard. Berezinskii-Kosterlitz-Thouless crossover in a trapped atomic gas. *Nature*, 441(7097):1118–1121, 2006.
- [92] P. Krüger, Z. Hadzibabic, and J. Dalibard. Critical point of an interacting two-dimensional atomic Bose gas. *Phys. Rev. Lett.*, 99(4):040402, 2007.
- [93] V. Schweikhard, S. Tung, and E. A. Cornell. Vortex proliferation in the Berezinskii-Kosterlitz-Thouless regime on a two-dimensional lattice of Bose-Einstein condensates. *Phys. Rev. Lett.*, 99(3):030401, 2007.
- [94] P. Cladé, C. Ryu, A. Ramanathan, K. Helmerson, and W. D. Phillips. Observation of a 2D Bose gas: From thermal to quasicondensate to superfluid. *Phys. Rev. Lett.*, 102(17):170401, 2009.
- [95] Z. Hadzibabic, P. Krger, M. Cheneau, S. P. Rath, and J. Dalibard. The trapped two-dimensional Bose gas: From Bose-Einstein condensation to berezinskii-Kosterlitz-Thouless physics. *New Journal of Physics*, 10:045006, 2008.
- [96] S. Tung, G. Lamporesi, D. Lobser, L. Xia, and E. A. Cornell. Observation of the pre-superfluid regime in a two-dimensional Bose gas. *Phys. Rev. Lett.*, 105(23):230408, 2010.
- [97] N. Prokof'ev, O. Ruebenacker, and B. Svistunov. Critical point of a weakly interacting two-dimensional Bose gas. *Phys. Rev. Lett.*, 87(27 I):270402, 2001.
- [98] N. Prokof'ev and B. Svistunov. Two-dimensional weakly interacting Bose gas in the fluctuation region. *Phys. Rev. A*, 66(4):43608, 2002.
- [99] M. Holzmann, M. Chevallier, and W. Krauth. Universal correlations and coherence in quasi-two-dimensional trapped Bose gases. *Phys. Rev. A*, 81(4):043622, 2010.
- [100] M. Holzmann, G. Baym, J. P. Blaizot, and F. Laloë. Superfluid transition of homogeneous and trapped two-dimensional Bose gases. *Proceedings of the National Academy of Sciences of the United States of America*, 104(5):1476–1481, 2007.
- [101] C. Mora and Y. Castin. Ground state energy of the two-dimensional weakly interacting Bose gas: First correction beyond Bogoliubov theory. *Phys. Rev. Lett.*, 102(18):180404, 2009.
- [102] T. P. Simula, M. J. Davis, and P. B. Blakie. Superfluidity of an interacting trapped quasi-two-dimensional Bose gas. *Phys. Rev. A*, 77(2):023618, 2008.
- [103] M. Holzmann and W. Krauth. Kosterlitz-Thouless transition of the quasi-two-dimensional trapped Bose gas. *Phys. Rev. Lett.*, 100(19):190402, 2008.

- [104] V.N. Popov and J. Niederle. *Functional Integrals in Quantum Field Theory and Statistical Physics*. D. Reidel Publishing Company, 1983.
- [105] R. N. Bisset, M. J. Davis, T. P. Simula, and P. B. Blakie. Quasicondensation and coherence in the quasi-two-dimensional trapped Bose gas. *Phys. Rev. A*, 79(3):033626, 2009.
- [106] Kerson Huang. *Statistical mechanics*. New York : Wiley, 2nd ed. edition, 1987.
- [107] R. Kubo. The fluctuation-dissipation theorem. *Reports on Progress in Physics*, 29(1):255–284, 1966.
- [108] M. Toda, R. Kubo, and N. Saitō. *Statistical physics I: equilibrium statistical mechanics*. Springer series in solid-state sciences. Springer, 1995.
- [109] Qi Zhou and Tin-Lun Ho. Universal thermometry for quantum simulation. *Phys. Rev. Lett.*, 106(22):225301, May 2011.
- [110] M. Naraschewski and R. J. Glauber. Spatial coherence and density correlations of trapped Bose gases. *Phys. Rev. A*, 59(6):4595–4607, 1999.
- [111] T. Donner, S. Ritter, T. Bourdel, A. Öttl, M. Köhl, and T. Esslinger. Critical behavior of a trapped interacting Bose gas. *Science*, 315(5818):1556–1558, 2007.
- [112] G. Reinaudi, T. Lahaye, Z. Wang, and D. Guéry-Odelin. Strong saturation absorption imaging of dense clouds of ultracold atoms. *Optics Letters*, 32(21):3143–3145, 2007.
- [113] D. Forster. *Hydrodynamic fluctuations, broken symmetry, and correlation functions*. Advanced Books Classics. Perseus Books, 1995.
- [114] Ehud Altman, Eugene Demler, and Mikhail D. Lukin. Probing many-body states of ultracold atoms via noise correlations. *Phys. Rev. A*, 70(1):013603, Jul 2004.
- [115] M. Schellekens, R. Hoppeler, A. Perrin, J. Viana Gomes, D. Boiron, A. Aspect, and C. I. Westbrook. Hanbury brown twiss effect for ultracold quantum gases. *Science*, 310(5748):648–651, 2005.
- [116] T. Rom, Th Best, D. van Oosten, U. Schneider, S. Fölling, B. Paredes, and I. Bloch. Free Fermion antibunching in a degenerate atomic Fermi gas released from an optical lattice. *Nature*, 444(7120):733–736, 2006.
- [117] T. Jelte, J. M. McNamara, W. Hogervorst, W. Vassen, V. Krachmalnicoff, M. Schellekens, A. Perrin, H. Chang, D. Boiron, A. Aspect, and C. I. Westbrook. Comparison of the hanbury brown-twiss effect for bosons and Fermions. *Nature*, 445(7126):402–405, 2007.

- [118] Christian Sanner, Edward J. Su, Aviv Keshet, Ralf Gommers, Yong-il Shin, Wujie Huang, and Wolfgang Ketterle. Suppression of density fluctuations in a quantum degenerate Fermi gas. *Phys. Rev. Lett.*, 105(4):040402, Jul 2010.
- [119] M. Greiner, C. A. Regal, J. T. Stewart, and D. S. Jin. Probing pair-correlated Fermionic atoms through correlations in atom shot noise. *Phys. Rev. Lett.*, 94(11):110401, Mar 2005.
- [120] S. Hofferberth, I. Lesanovsky, T. Schumm, A. Imambekov, V. Gritsev, E. Demler, and J. Schmiedmayer. Probing quantum and thermal noise in an interacting many-body system. *Nature Physics*, 4(6):489–495, 2008.
- [121] S. Manz, R. Bücker, T. Betz, Ch. Koller, S. Hofferberth, I. E. Mazets, A. Imambekov, E. Demler, A. Perrin, J. Schmiedmayer, and T. Schumm. Two-point density correlations of quasicondensates in free expansion. *Phys. Rev. A*, 81(3):031610, Mar 2010.
- [122] Amir Itah, Hagar Veksler, Oren Lahav, Alex Blumkin, Coral Moreno, Carmit Gordon, and Jeff Steinhauer. Direct observation of a sub-poissonian number distribution of atoms in an optical lattice. *Phys. Rev. Lett.*, 104(11):113001, Mar 2010.
- [123] Torben Müller, Bruno Zimmermann, Jakob Meineke, Jean-Philippe Brantut, Tilman Esslinger, and Henning Moritz. Local observation of antibunching in a trapped Fermi gas. *Phys. Rev. Lett.*, 105(4):040401, Jul 2010.
- [124] J. Armijo, T. Jacqmin, K. V. Kheruntsyan, and I. Bouchoule. Probing three-body correlations in a quantum gas using the measurement of the third moment of density fluctuations. *Phys. Rev. Lett.*, 105(23):230402, Nov 2010.
- [125] W. S. Bakr, A. Peng, M. E. Tai, R. Ma, J. Simon, J. I. Gillen, S. Föling, L. Pollet, and M. Greiner. Probing the superfluid-to-Mott insulator transition at the single-atom level. *Science*, 329(5991):547–550, 2010.
- [126] Jacob F. Sherson, Christof Weitenberg, Manuel Endres, Marc Cheneau, Immanuel Bloch, and Stefan Kuhr. Single-atom-resolved fluorescence imaging of an atomic Mott insulator. *Nature*, 467(7311):68–72, 2010.
- [127] Christian Sanner, Edward J. Su, Aviv Keshet, Wujie Huang, Jonathon Gillen, Ralf Gommers, and Wolfgang Ketterle. Speckle imaging of spin fluctuations in a strongly interacting Fermi gas. *Phys. Rev. Lett.*, 106(1):010402, Jan 2011.
- [128] Thibaut Jacqmin, Julien Armijo, Tarik Berrada, Karen V. Kheruntsyan, and Isabelle Bouchoule. Sub-poissonian fluctuations in a 1D Bose gas: From the quantum quasi-condensate to the strongly interacting regime. *Phys. Rev. Lett.*, 106(23):230405, Jun 2011.

- [129] S. Giorgini, L. P. Pitaevskii, and S. Stringari. Anomalous fluctuations of the condensate in interacting Bose gases. *Phys. Rev. Lett.*, 80(23):5040–5043, Jun 1998.
- [130] L. Pitaevskii and S. Stringari. *Bose-Einstein condensation*. Oxford : Oxford University Press, 2003.
- [131] D. Pines and P. Nozières. *The Theory of Quantum Liquids*, volume I. New York : W A Benjamin, 1966.
- [132] P. Nozières and D. Pines. *The Theory of Quantum Liquids*, volume II. Reading, MA : Addison-Wesley, 1990.
- [133] Pitaevskii L P Klawunn M, Recati A and Stringari S. Local atom number fluctuations in quantum gases at finite temperature. *arXiv:1102.3805v1*, 2011.
- [134] D. M. Stamper-Kurn, A. P. Chikkatur, A. Görlitz, S. Inouye, S. Gupta, D. E. Pritchard, and W. Ketterle. Excitation of phonons in a Bose-Einstein condensate by light scattering. *Phys. Rev. Lett.*, 83(15):2876–2879, Oct 1999.
- [135] J. Steinhauer, R. Ozeri, N. Katz, and N. Davidson. Excitation spectrum of a Bose-Einstein condensate. *Phys. Rev. Lett.*, 88(12):120407, Mar 2002.
- [136] E. D. Kuhnle, H. Hu, X.-J. Liu, P. Dyke, M. Mark, P. D. Drummond, P. Hannaford, and C. J. Vale. Universal behavior of pair correlations in a strongly interacting Fermi gas. *Phys. Rev. Lett.*, 105(7):070402, Aug 2010.
- [137] R Bücke, A Perrin, S Manz, T Betz, Ch Koller, T Plisson, J Rottmann, T Schumm, and J Schmiedmayer. Single-particle-sensitive imaging of freely propagating ultracold atoms. *New Journal of Physics*, 11(10):103039, 2009.
- [138] M. Karski, L. Förster, J. M. Choi, W. Alt, A. Widera, and D. Meschede. Nearest-neighbor detection of atoms in a 1D optical lattice by fluorescence imaging. *Phys. Rev. Lett.*, 102(5):053001, Feb 2009.
- [139] Goodman J W. *Introduction to Fourier Optics*. Greenwood Village: Roberts & Co, 2005.
- [140] W. Ketterle, D. S. Durfee, and D. M. Stamper-Kurn. Making, probing and understanding Bose-Einstein condensates. *Proceedings of the International School of Physics "Enrico Fermi"*, Course CXL:p67, 1999.
- [141] Augustus J. E. M. Janssen. Extended Nijboer-Zernike approach for the computation of optical point-spread functions. *J. Opt. Soc. Am. A*, 19(5):849–857, May 2002.
- [142] G. E. Astrakharchik, R. Combescot, and L. P. Pitaevskii. Fluctuations of the number of particles within a given volume in cold quantum gases. *Phys. Rev. A*, 76(6):063616, Dec 2007.

- [143] F. Meier and W. Zwerger. Anomalous condensate fluctuations in strongly interacting superfluids. *Phys. Rev. A*, 60(6):5133–5135, Dec 1999.
- [144] W. Zwerger. Anomalous fluctuations in phases with a broken continuous symmetry. *Phys. Rev. Lett.*, 92(2):027203, Jan 2004.
- [145] Subir Sachdev. Universal relaxational dynamics near two-dimensional quantum critical points. *Phys. Rev. B*, 59(21):14054–14073, Jun 1999.
- [146] Subir Sachdev and Emily R. Dunkel. Quantum critical dynamics of the two-dimensional Bose gas. *Phys. Rev. B*, 73(8):085116, Feb 2006.
- [147] S. Sachdev, Quantum magnetism and criticality, *Nature Physics*, 4, 173-185 (2008).
- [148] U. A. Khawaja, H. Stoof, Skyrmions in a ferromagnetic Bose-Einstein condensate. *Nature*, **411**, 918-920 (2001).
- [149] T. Senthil, A. Vishwanath, L. Balents, S. Sachdev, M. P. A. Fisher, Deconfined Quantum Critical Points. *Science*, **303**, 1490-1494 (2004).
- [150] R. Coldea *et al.*, Quantum Criticality in an Ising Chain: Experimental Evidence for Emergent  $E_8$  Symmetry. *Science*, **327**, 177-180 (2010).
- [151] R. Jaramillo, Y. Feng, J. Wang, T. F. Rosenbaum, Signatures of quantum criticality in pure Cr at high pressure. *Proc. Nat. Acad. Sci.* **107**, 13631-13635 (2010).
- [152] K. Baumann, C. Guerlin, F. Brennecke, T. Esslinger, Dicke quantum phase transition with a superfluid gas in an optical cavity. *Nature*, **464**, 1301-1306 (2010).
- [153] Elmar Haller, Russell Hart, Manfred J. Mark, Johann G. Danzl, Lukas Reichsöllner, Mattias Gustavsson, Marcello Dalmonte, Guido Pupillo, and Hanns-Christoph Nägerl. Pinning quantum phase transition for a Luttinger liquid of strongly interacting bosons. *Nature*, 466(7306):597–600, 2010.
- [154] J. Simon *et al.*, Quantum simulation of antiferromagnetic spin chains in an optical lattice. *Nature* **472**, 307-312 (2011).
- [155] R. Löw *et al.*, Universal scaling in a strongly interacting Rydberg gas. *Phys. Rev. A* **80**, 033422 (2009).
- [156] Q. Zhou, T.-L. Ho, Signature of Quantum Criticality in the Density Profiles of Cold Atom Systems. *Phys. Rev. Lett.* **105**, 245702 (2010).
- [157] K. R. A. Hazzard, E. J. Mueller, Techniques to measure quantum criticality in cold atoms. *Phys. Rev. A* **84**, 013604 (2011).

- [158] Shiang Fang, Chia-Min Chung, Ping Nang Ma, Pochung Chen, and Daw-Wei Wang. Quantum criticality from in situ density imaging. *Phys. Rev. A*, 83(3):031605, Mar 2011.
- [159] Y. Kato, Q. Zhou, N. Kawashima, N. Trivedi, Sharp peaks in the momentum distribution of bosons in optical lattices in the normal state. *Nature Physics*, **4**, 617-621 (2008).
- [160] Zhou Q, Kato Y, Kawashima N and Trivedi N 2009, Direct mapping of the finite temperature phase diagram of strongly correlated quantum models, *Phys. Rev. Lett.* **103** 085701.
- [161] S. T. Bramwell, P. C. W. Holdsworth, Magnetization: A characteristic of the Kosterlitz-Thouless-Berezinskii transition. *Phys. Rev. B*, **49**, 8811-8814 (1994).
- [162] B. Capogrosso-Sansone *et al.*, The Beliaev technique for a weakly interacting Bose gas. *New J. Phys.* **12**, 043010 (2010).
- [163] Wojciech H. Zurek, Uwe Dorner, and Peter Zoller. Dynamics of a quantum phase transition. *Phys. Rev. Lett.*, 95(10):105701, Sep 2005.
- [164] Subir Sachdev and Oleg A. Starykh. Thermally fluctuating superconductors in two dimensions. *Nature*, 405(6784):322–325, 2000.
- [165] Min-Chul Cha, Matthew P. A. Fisher, S. M. Girvin, Mats Wallin, and A. Peter Young. Universal conductivity of two-dimensional films at the superconductor-insulator transition. *Phys. Rev. B*, 44(13):6883–6902, Oct 1991.
- [166] Makariy A. Tanatar, Johnpierre Paglione, Cedimir Petrovic, and Louis Taillefer. Anisotropic violation of the Wiedemann-Franz law at a quantum critical point. *Science*, 316(5829):1320–1322, 2007.
- [167] Stefan S. Natu, Kaden R. A. Hazzard, and Erich J. Mueller. Local versus global equilibration near the bosonic Mott-insulator-superfluid transition. *Phys. Rev. Lett.*, 106(12):125301, Mar 2011.
- [168] J. Rammer. *Quantum Transport Theory*. Frontiers in Physics. Massachusetts: Perseus books, 1998.
- [169] Jr Walter T. Grandy. *Entropy and the Time Evolution of Macroscopic Systems*. Oxford University Press, Oxford, 2008.
- [170] Subir Sachdev. Finite temperature dissipation and transport near quantum critical points. *arXiv:0910.1139v2*, 2010.
- [171] T W B Kibble. Topology of cosmic domains and strings. *Journal of Physics A: Mathematical and General*, 9(8):1387, 1976.

- [172] W. H. Zurek. Cosmological experiments in superfluid helium? *Nature*, 317(6037):505–508, 1985.
- [173] Anatoli Polkovnikov. Universal adiabatic dynamics in the vicinity of a quantum critical point. *Phys. Rev. B*, 72(16):161201, Oct 2005.
- [174] C. De Grandi, V. Gritsev, and A. Polkovnikov. Quench dynamics near a quantum critical point. *Phys. Rev. B*, 81(1):012303, Jan 2010.
- [175] J. R. Abo-Shaeer, C. Raman, J. M. Vogels, and W. Ketterle. Observation of vortex lattices in Bose-Einstein condensates. *Science*, 292(5516):476–479, 2001.
- [176] I. Coddington, P. C. Haljan, P. Engels, V. Schweikhard, S. Tung, and E. A. Cornell. Experimental studies of equilibrium vortex properties in a Bose-condensed gas. *Phys. Rev. A*, 70(6):063607, Dec 2004.
- [177] Ralf Schützhold, Michael Uhlmann, Yan Xu, and Uwe R. Fischer. Sweeping from the superfluid to the Mott phase in the Bose-Hubbard model. *Phys. Rev. Lett.*, 97(20):200601, Nov 2006.
- [178] Anatoli Polkovnikov and Vladimir Gritsev. Breakdown of the adiabatic limit in low-dimensional gapless systems. *Nature Physics*, 4(6):477–481, 2008.
- [179] Marcos Rigol, Vanja Dunjko, and Maxim Olshanii. Thermalization and its mechanism for generic isolated quantum systems. *Nature*, 452(7189):854–858, 2008.